2015-02-03

Vector-based and Ultra-Tight GPS/INS Receiver Performance in the Presence of Continuous Wave Jamming

Krasovski, Sergey

UNIVERSITY OF CALGARY

Vector-based and Ultra-Tight GPS/INS Receiver Performance in the Presence of Continuous Wave Jamming

by

Sergey Krasovski

A THESIS

SUBMITTED TO THE FACULTY OF GRADUATE STUDIES

IN PARTIAL FULFILMENT OF THE REQUIREMENTS FOR THE

DEGREE OF MASTER OF SCIENCE

GRADUATE PROGRAM IN GEOMATICS ENGINEERING

CALGARY, ALBERTA

JANUARY, 2015

Abstract

This thesis investigates the ability of a vector-based Global Positioning System (GPS) receiver and an ultra-tight GPS/inertial receiver to detect and mitigate Continuous Wave (CW) interference in tracking and navigation domains. In this work, an Interference Detector (ID) is incorporated into the tracking domain of a GPS software receiver and a new observation weighting (OW) algorithm is developed to help classify GPS measurements when CW signal is present.

Results show that both vector-based and ultra-tight GPS receivers, accompanied by the ID and OW, offer better navigation solution accuracies in CW jamming than their un-aided counterparts. Specifically, aided receivers improved the horizontal position approximately by a factor of two, while the horizontal velocity errors of the aided vector-based receiver were reduced by a factor of four compared to that of the un-aided counterpart during interference. Also, the novel OW technique set more appropriate observation variances than the carrier-to-noise (C/N_0) weighting in jamming.

Acknowledgements

I would like to thank my supervisor, Professor Mark Petovello, for his continued support and encouragement, attention to detail and unique perspective on my research. Your hard work, enormous motivation and dedication to research have been a super powerful source of inspiration for me over these two and a half years. Thank you for having your doors always opened for me and thank you for your trust in me.

Special gratitude is addressed to my co-supervisor, Professor Gérard Lachapelle. It was a big honour to study under your guidance. Literally every advice you have given to me is very much appreciated. Also, thank you for exposing me to world-class resources and accepting me to your top-level scientific team. Additionally, thank you for taking me to several fantastic hikes and introducing to the breathtaking Canadian Rockies.

All my accomplishments would not be possible without my parents. I cannot express all my love and respect to them only with words. You are the ones who gave me the chance to see the World, and I will always value your limitless care, love and understanding.

I would like to thank all my relatives who have always supported and cheered me during my graduate studies.

Big thanks go to many members of the PLAN Group:

- Zhe He, Ali Broumandan, Srinivas Bhaskar, Vijaykumar Bellad and G. S. Naveen for sharing your technical experience and helping with my data collections.
- My C++ gurus, Bernhard Aumayer and Bashir Kazemipur, for their advices and help, which greatly improved my coding skills.
- Tiantong Ren, Paul Verlaine Gakne and Adam Clare for sharing the office with me and being so friendly and supportive. I could not dream of better office mates.
- The Great Nepalese Anup Dhital. Our football discussions and games, hikes and conversations were a great fun, which will never be forgotten.
- Erin Kahr, Rakesh Kumar and Jingjing Dou, for being so nice and friendly.

- All amazing graduate students from the PLAN Group, who supported me and accompanied for hundreds of coffee breaks, thank you.

To all executives of the G^3, who made my social life within the department interesting and dynamic, thank you very much.

I would also like to thank my Belarusian friends Katia, Dima Kuziuberdin, and Masha. Your friendship and kindness are very important to me.

To the staff of the Department of Geomatics Engineering, thank you a lot. Your smiles were always supportive and warm.

I would like to acknowledge the Calgary Airport Authority for providing me with financial support.

Dedication

To my beloved mama and papa, Elena and Pavel.
Without you, I wouldn't be even a fraction of who I am.

Table of Contents

List of Tables

List of Figures and Illustrations

List of Abbreviations

Symbol	Definition
ADC	Analog-to-Digital Converter
AGC	Automatic Gain Control
BPSK	Binary Phase-Shift Keying
CAF	Cross-Ambiguity Function
C/A	Coarse Acquisition
C/N_0	Carrier-to-Noise Ratio
CW	Continuous Wave
DLL	Delay Lock Loop
DOP	Dilution Of Precision
ECEF	Earth-Centred, Earth-Fixed
EKF	Extended Kalman Filter
FFT	Fast Fourier Transform
FLI	Frequency Lock Indicator
FLL	Frequency Lock Loop
GBAS	Ground-Based Augmentation System
GLONASS	Global Navigation Satellite System
GNSS	Global Navigation Satellite System
GPS	Global Positioning System
GSM	Global System For Mobile Communications
ID	Interference Detector
IF	Intermediate Frequency

IMU	Inertial Measurement Unit
INS	Inertial Navigation System
J/S	Jamming to Signal Ratio
J/N	Jamming to Noise Ratio
KF	Kalman Filter
LTE	Long Term Evolution
LS	Least Squares
LOS	Line-Of-Sight
NCO	Numerically Controlled Oscillator
NLOS	Non-Line-Of-Sight
OCXO	Ovenized Crystal Oscillator
PLI	Phase Lock Indicator
PLL	Phase Lock Loop
PPD	Personal Privacy Devices
PR	Pseudorange
PRR	Pseudorange Rate
PRN	Pseudorandom Number
RF	Radio Frequency
RFI	Radio-Frequency Interference
RMS	Room Mean Square
Rx	Receiver
SV	Satellite Vehicle
TCXO	Temperature-Compensated Crystal Oscillator
UT	Ultra-Tight

VB	Vector-Based

List of Symbols

Symbol	Definition
$(\bullet)^{SV}$	Parameter Corresponding to the Satellite
$(\bullet)^{Rx}$	Parameter Corresponding to the User
$(\bullet)^{-}$	Quantity Before the Measurement Update
$(\bullet)^{+}$	Quantity After the Measurement Update
$\sigma_{(\bullet)}$	Standard Deviation of Subscribed Quantity
$\sigma^2_{(\bullet)}$	Variance of Subscribed Quantity
A_J	Amplitude of the CW Jamming Signal
A_R	Amplitude of Code Correlation Function
C	Spreading Code
C_0	Discrete Fourier Transform of the C/A Gold Code
C_υ	Covariance Matrix of Innovation Sequence
c	Speed of Light in Vacuum
cdt^{SV}	Satellite Clock Drift
cdt^{Rx}	Receiver Clock Drift
D	Navigation Data Bits
d	Code Correlator Offset

dt^{SV}	Satellite Clock Bias Relative to the True GPS Time
dt^{Rx}	Receiver Clock Bias Relative to the True GPS Time
$f_{C/A}$	Frequency of the Strongest Line in C/A Code Spectrum
f_c	Chipping Rate
f_{CW}	Frequency of CW Jamming Signal
f_D	Doppler Frequency
$\hat{f}_D$	Estimated Doppler Frequency
f_J	Frequency of Jamming Signal
f_R	C/A Code Repetition Frequency
f_{L1}	GPS L1 Carrier Frequency
H	Design Matrix
$I(n)$	In-Phase Sample of the Received Signal
K	Kalman Gain Matrix
k_0	Number of the C/A Code Spectrum Line (0 to 1022)
N_0	Noise Spectral Density
n	Sample Number
P	Covariance Matrix of the Estimated States
$Q(n)$	Quadrature Sample of the Received Signal
Q	Process Noise Matrix
$R(\bullet)$	Autocorrelation Function
R	Covariance Matrix of the Observations

$\vec{r}$	Position Vector of the Satellite or Receiver
$S_{L1}(t)$	Signal Transmitted by a GPS Satellite at L1 Frequency
$s(n)$	Signal Sampled by a Front-End
T_{coh}	Coherent Integration Time
T_s	Sampling Rate of a Front-End
T_i	Integration Interval
t	Time Instance
t_{chip}	Duration of One Code Chip
$\vec{v}$	Velocity Vector of the Satellite or Receiver
v	Measurement Noise Vector
w	Process Noise Vector
x	State Vector
z	Observation Vector
δf_D	Doppler Error
$\delta\phi$	Carrier Phase Error
Φ	State Transition Matrix
ϕ	Carrier Phase Offset
γ	Test Statistic
η	Additive Gaussian Noise
λ	Down-Weighting Coefficient
θ	Scaling Factor for the Detection Threshold
ρ	Geometric Range Between the Satellite and the User Receiver
$\dot{\rho}$	Geometric Range Rate Between the Satellite and the User Receiver

τ	Code Phase Delay
$\hat{\tau}$	Estimated Code Phase Delay
υ	Innovation Sequence Vector
ψ	Composite Phase Component of the Interference Signal and GPS Signal

Epigraph

“To strive, to seek, to find, and not to yield”

Alfred Tennyson

Chapter One: Introduction

Satellite navigation plays a paramount role in today's society. Technologies and services provided by Global Navigation Satellite Systems (GNSS), such as The United States' Global Positioning System (GPS) and Russia's GLObal NAvigation Satellite System (GLONASS), are widely used in all aspects of our life. Nowadays, numerous applications rely on GNSS; examples include, but are not limited to, commercial aircraft positioning, automobile and pedestrian navigation, sportsmen performance tracking, stock market time synchronization, earth surface motion monitoring, etc. Furthermore, performance of GPS-only equipment can be significantly improved by augmenting it with the data from other sensors, such as Inertial Measurement Units (IMUs), cameras, barometers, magnetometers, LIDARs, etc. (e.g. Noureldin et al 2013, Aumayer et al 2014, Huang 2010, and Liu et al 2014). Such hybrid navigation systems provide users with much more accurate and reliable positioning information in GNSS challenged environments. However, due to the inherently low power of GPS signals that arrive from the satellites, they are extremely vulnerable to various kinds of radio-frequency interference (Ward 1994). In spite of the fact that there are numerous interference detection and mitigation algorithms, which have their own advantages and disadvantages, new methods are still being developed to protect the GNSS devices against interference.

This thesis investigates the ability of a GPS software receiver to identify interference signals and, based on the detection results, make a decision whether the data from the GPS satellites can be used to compute an accurate navigation solution or not.

1.1 Background

The following subsections discuss the problem of radio-frequency interference (RFI) signals in the field of GNSS, briefly summarize various types of RFI signals, which pose a threat for GNSS receivers, and present a high-level concept of a GNSS Receiver.

1.1.1 Problems of Radio-Frequency Interference in GNSS

Due to GNSS system design, signals arriving from the navigation satellites to receivers on the surface of the Earth have extremely low power. Owing to this fact, they are very vulnerable to RFI signals that may be originated from different sources. Examples of interference signals include, but are not limited to, intentional sources such as Personal Privacy Devices (PPD) and unintentional sources such as Digital Enhanced Cordless Telecommunications (DECT) and Long Term Evolution (LTE) signal (Craven et al 2012).

Interference signals are a major threat to all users of GNSS services because they can cause the GNSS equipment to perform unreliably and provide erroneous position information.

Several instances of GPS interference have been reported by the Federal Aviation Administration in recent years. One of them was reviewed by Gibbons (2013): it was found that a truck driver used a portable GPS jammer at Newark Liberty International Airport, and that this illegal action caused a malfunction in the Ground-Based Augmentation System (GBAS) of the Airport that could have led to catastrophic consequences.

Another example of GPS equipment being potentially corrupted by interference was produced by researchers at the University of Texas at Austin who tricked the navigation system of an $80 million yacht and sent the ship off course. This experiment showed how vulnerable any device with civilian GPS technology is to an effect called spoofing. In this test, the spoofing device was built at a cost of approximately $2000. It was generating fake GPS signals, which could not be distinguished from real GPS signals by the receiver installed on the yacht. As a result, the navigation system on the ship was fooled and reported to the captain that the boat was underwater; moreover, the ship was moving three degrees away from the actual course.

One more interesting instance of GPS jamming was reported by Herald Sun in 2013 (Chronos Technology 2014): more than one hundred taxi drivers in one of the cab companies in the City of Melbourne were fired or admonished for illegal use of portable GPS jamming devices that were used to steal fares.

From the above examples it is obvious that the importance of RFI signal detection and elimination of its effects on GNSS receivers cannot be underestimated.

1.1.2 Overview of RFI Signals

Interference signals can be categorized based on their signal spectrum characteristics; narrow band (NB) and wide band (WB) according to Ward et al (2006) or based on their generation nature, either intentional or unintentional as shown in Dovis (2011). However, in the author's opinion, it is convenient to group the RFI signals into the following three major categories: unintentional interference, spoofing and jamming.

The first type of RFI is the interference signal, which usually has an unintentional nature and comprises multipath, radio signals from cell towers, Digital Video Broadcasting (DVB), Wi-Fi, Bluetooth, Frequency-modulated (FM), Amplitude-modulated (AM), Phase-modulated (PM), etc. This type of RFI is somehow less severe than the other two kinds, which will be addressed later in this section, but can still negatively affect a GNSS receiver at the signal acquisition stage or cause the receiver to produce position errors up to several hundreds of metres as shown by Craven et al (2012), Xie (2013), and Wildemeersch & Fortuny-Guasch (2010).

Multipath is a type of interference signal, which is formed when the line-of-sight (LOS) signal from satellite vehicle (SV) is reflected by some objects and, as a result, an antenna receives both LOS and indirect LOS signals (Ward et al 2006, Tsui 2005). In other words, multipath refers to the phenomenon of a signal reaching an antenna via

indirect path(s). When an antenna receives only the LOS signal reflected by a single object (several objects), such signal is usually called a non-line of sight (NLOS) signal (Ward et al 2006). As a result, the total propagation time for a multipath signal is always longer than the propagation time of the LOS signal. Usually, apart from multipath, other unintentional interference signals are strong out-of-band signals, and their spectral side lobes and powerful harmonics can seriously interfere with the GNSS band (Wildemeersch & Fortuny-Guasch 2010).

The second category of RFI, spoofing, is typical among intentional interference soruces, and it can be split into three subcategories according to Jafarnia-Jahromi et al (2012): GPS signal generator, intermediate receiver-based spoofer and sophisticated receiver-based spoofer. The main goal of spoofing is to produce the counterfeit GNSS-like signals, which will mislead a GNSS receiver at the user's end (Jafarnia-Jahromi 2013, Neilsen et al 2011). In other words, this type of interference signal tries to convince a GNSS receiver that it is located somewhere else by transmitting fake GNSS signals.

The last kind of deliberate RFI is known as jamming, and it poses a major danger to GNSS receivers, the more so because such interference sources are easily available on the market (e.g. Chronos Technology 2014), and these are capable of generating in-band radio signals with the power exceeding the thermal noise floor, and therefore drastically affecting GNSS devices (Craven et al 2012, Rugamer et al 2013). Most common jamming signals include CW and Chirp signals.

To summarize the above, Table 1.1 presents some of the interference signals that can adversely affect GNSS equipment (e.g. Ward et al 2006, Borio 2008).

Table 1.1: Summary of RFI types, their parameters and potential sources

Interference Type	Source	Signal Type	Parameters	
			Frequency Range	Power
Unintentional	DVB, ultra-wideband systems, radars, cell towers, Wi-Fi	Side harmonics, FM-, AM, and PM-modulated	NB, WB	$< P_{GNSS}$
Jamming	PPDs	CW, Chirp, Swept, Pulse	NB, WB	$>> P_{GNSS}$
Spoofing	GNSS signal generators, USRP	Fake GNSS signals	"fake" f_{GNSS}	$\geq P_{GNSS}$

1.1.3 GNSS Receiver Concept

A typical GNSS receiver, consisting of the analog and digital blocks, is shown in Figure 1.1. This sub-section briefly introduces the concept of a GNSS receiver to demonstrate its general structure. This knowledge is necessary to allow a better understanding of the following questions: how various RFI signals can affect a GNSS receiver and how interference signals can be detected and mitigated. In turn, this helps motivate the work done in this thesis. A more detailed discussion of the structure of a GNSS receiver is given in Chapter 2.

In Figure 1.1, the GNSS antenna receives the incoming satellite signal $x(t)$ in analog form, which is further passed to the analog block also known as the signal conditioning block that filters out undesired frequencies, amplifies the desired signal and converts the signals to baseband. The amplification unit is called a Low-noise amplifier (LNA), which injects some noise in the received signal but provides enough gain to cause any losses inserted after the LNA to have a negligible effect, as discussed by Van Dierendonck (1996) and Misra & Enge (2011).

Down-conversion is how the radio-frequency (RF) signal is down-converted to baseband either directly or through an Intermediate Frequency (IF) step (Van Dierendonck 1996, Navipedia 2014). Finally, the baseband signal is quantized into digital samples $x(n)$ in the Analog-To-Digital (ADC) converter, which ensures that quantization errors and dynamic ranges are appropriate to accommodate the signal's characteristics (Pany 2010, Navipedia 2014). Usually, the ADC is accompanied by the Automatic Gain Control (AGC) unit, which is closely related to digital down-conversion and quantization steps and is responsible for adjusting the gain of the front-end section in order to take benefit from the full dynamic range (Curran et al 2009).

After the incoming signal is converted to digital samples, it is passed to the Digital Signal Processing (DSP) block (sometimes referred to as baseband processing block), which includes three main stages: signal acquisition, tracking, and Position, Velocity and Time (PVT) computation (Misra and Enge 2011).

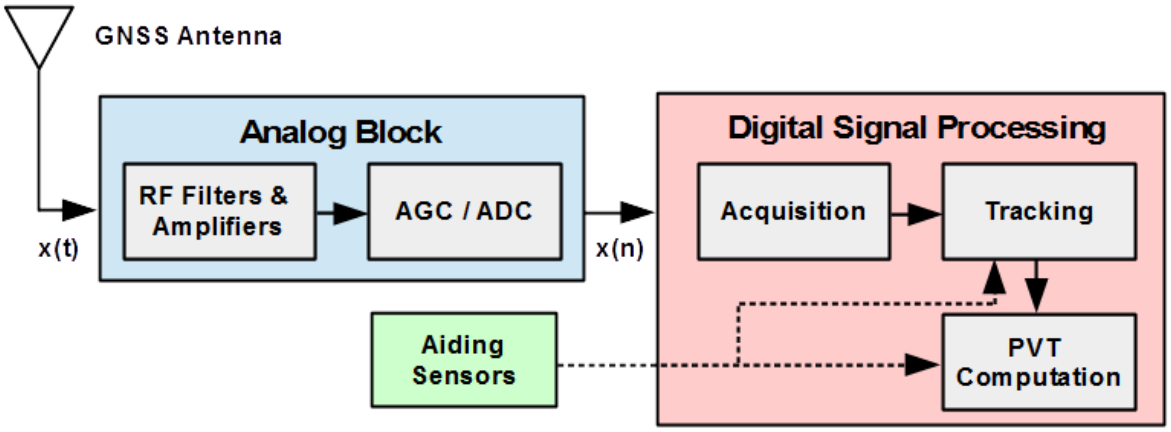

Figure 1.1: General Structure of a GNSS Receiver

According to Van Dierendonck (1996), the main functions of these three sub-blocks within the DSP module, as shown in Figure 1.1, are as follows:

- Signal acquisition from all navigation satellites currently in view of the receiver. Specifically, by correlating the incoming signal samples with a local replica, the acquisition algorithm attempts to detect the signals from all observable navigation satellites. Also, the acquisition procedure provides coarse estimates of the signal parameters, namely Doppler frequency and code delay.
- Tracking of the acquired signal parameters and raw measurement computation. The measurements of interest are pseudoranges and pseudorange rates, which are essentially the noisy and biased measurements of ranges and range rates between the SV and the user's antenna, respectively. In other words, the tracking module performs fine estimation of the signal parameters, which are produced by the acquisition algorithm, and generates GNSS observations for the PVT module.

- Navigation solution computation using pseudorange and pseudorange rate observations. It is known that observations from at least four SVs should be available to compute the PVT solution (Misra & Enge 2011).

As Figure 1.1 depicts, PVT computation and GNSS signal tracking can be aided by the data from other sensors, such as IMU, camera, barometer, etc. Moreover, other data such as 3D city models can be utilized to aid the GNSS receiver (Kumar & Petovello 2014, Wang et al 2012). Such data fusion from navigation satellites and external sources yields improved robustness, continuity and accuracy of positioning in GNSS challenged environments (e.g. Noureldin et al 2013, Aumayer et al 2014, and Soloviev et al 2007).

1.2 Related Research in RFI Detection and Mitigation

This section provides an overview of the RFI detection and mitigation methods in various domains of a GNSS receiver. In general, interference signals can be identified and supressed at the antenna, pre-correlation and post-correlation levels as discussed by Gustafson et al (2000) and Landry & Renard (2014). Term pre-correlation means that the RFI identification happens before the incoming signal is correlated with a local replica, and, post-correlation means that the RFI detection is done either in code or frequency domain after the correlation process.

1.2.1 Multi-Antenna and Pre-Correlation Methods

A wide range of interference signals can be detected and mitigated at the antenna level or in hardware (RF front-end) of a GNSS receiver. Much effort was successfully spent to detect and mitigate multipath, jamming and spoofing signals using antenna-array techniques that comprise multiple-antenna usage and advanced signal processing methods.

The main concept of antenna array techniques is that the RFI signals are separated from useful GNSS signals using so-called spatial filtering known as a beamforming. Generally, there are two types of beamforming methods as shown by Van Veen & Buckley (1988). The first one samples the incoming signal in space (it is used to mitigate the narrowband RFI), and the second one samples the signal in both space and time (to mitigate wideband RFI). The high-level description of beamforming is the following: a beamformer creates a scalar output signal as a weighted combination of the data received at an array of antennas. The weights determine the spatial filtering characteristics of the beamformer and enable separation of signals if they arrive from different locations, even if the signals have overlapping frequencies.

Many different approaches that use antenna arrays for RFI identification and cancellation could be found in the open literature. A few examples are provided in this section. For instance, Brown (2000) applied the maximum-likelihood (ML) function to estimate the amplitude, delay and direction of multipath signals. Some approaches,

such as the multiple signal classification (MUSIC) algorithm, attempt to find the direction of multipath components and then put nulls in these directions to cancel the NLOS signals (Moelker 1998). Daneshmand (2013) suggested an efficient two-stage beam forming technique that allows elimination of high power RFI before signal despreading and mitigation of multipath after despreading.

A low-complexity multi-antenna method demonstrated by Daneshmand et al (2012) shows promising anti-spoofing results (authors estimate spatial signature vector of fake and real PRNs); it applies a null steering technique for spoofing signal removal and utilizes power maximization towards the authentic GPS signal. This method offers efficient spoofing mitigation before signal despreading and also has a lower computational load in comparison with other antenna-array methods. Moreover, Nielsen et al (2011) showed that even a single antenna device, provided its antenna is moving, could successfully resist spoofing signals when utilizing so-called synthetic array methods. The key idea of that approach is that fake GPS signals are spatially correlated, while the authentic signals from real SVs are not. Overall, antenna-array techniques offer a very good potential for RFI signal mitigation. However, this is achieved with an increased complexity and price of the system.

With regard to the AGC and ADC methods of RFI suppression, Ndili & Enge (1998) considered the AGC control loop gain as a metric to detect CW, broadband and pulsed interference. In the above work, the authors found that the AGC gain was a beneficial

resource for interference type identification when used in conjunction with other post-correlation metrics such as correlator power output, correlator output power variance, and carrier phase vacillation; however, it is not very sensitive to signal attenuation from individual SVs (AGC gain only reacts to the change in the total signal power received). Also, Moelker (1998) investigated and compared the performance of three various amplitude domain RFI mitigation techniques known as multi-level ADC conversion and Amplitude Domain Processor (ADP) in the presence of an Adaptive White Gaussian Noise (AWGN) and constant amplitude interference. In *ibid.* the evaluated parameter was the post-correlation Signal-To-Noise Ratio (SNR), and its degradation in the presence of interference was studied by the author. Although the ADP technique outperformed the ADC method, it is much more complex in terms of implementation, because it converts the incoming signal from in-phase (I) and quadrature (Q) to polar representation (this new signal needs to be processed additionally by a special function), and the result is only then converted back to the I and Q samples. Furthermore, both ADP and ADC RFI mitigation methods showed poor performance in the scenarios when multiple CW interference signals were present.

Several important facts should be reviewed when considering the AGC/ADC detection and mitigation methods. According to Abdizadeh (2013), low-resolution quantization units introduce several harmonics in the signal spectrum, even when only a simple CW interference signal is present, meaning all signal processing RFI mitigation techniques are additionally challenged. This is especially relevant for consumer-grade hardware,

where ADC units usually have one or two quantization bits. Additionally, Abdizadeh (2013) demonstrated that increased quantization resolution (amount of ADC bits) not only offers superior performance, but it also reduces the sensitivity to AGC gain tuning in the quantizer design.

It is known that Notch Filters (NF) are a good countermeasure against interference signals. The basic concept of these filters is that they pass all frequencies of the signal spectrum except those located in the stop or rejection band (Giordanengo 2010). According to *ibid.*, there are three different implementation approaches of the NFs, which can be categorized as follows:

- Fast-Fourier Transform (FFT);
- Finite Impulse Response (FIR); and
- Infinite Impulse Response (IIR).

The functioning principle of all FFT-based RFI detection and mitigation algorithms is the same: namely the excision of the interference signal is performed by zeroing the frequency bins that pass a certain predefined threshold (Giordanengo 2010).

As shown by Montloin (2010) and Borio (2008), the main advantage of the IIR NFs over FIR NFs is that the former has a frequency response closer to an ideal notch filter. Also, IIR filters have a lower computational complexity compared to FIR NFs, because they use fewer multipliers in their realization. However, both types of notch filters have an

impact on the code delay tracking loop. Firstly, they alter the shape and location of the correlation function in the time domain. Secondly, both FIR and IIR filters increase the tracking jitter of the code delay loop. Detailed analyses of various FIR and IIR NFs and their effects on GNSS signal processing can be found in Giordanengo (2010), Montloin (2010), Borio et al (2008), Borio (2008), and Lin et al (2011), Li Tan et al (2011).

The downside of all the above hardware-based anti-interference methods is that they usually increase the system complexity or require additional modifications in the hardware, which, in turn, leads to an increased cost in the system. The main challenge in the antenna-array applications is that the computational load can be significant if processing data from multiple antennas. Also, conventional antenna array processing techniques may fail to deal with multipath due to the fact that there is a high degree of correlation between the LOS and multipath signals. Moreover, adaptive filtering can negatively affect the signal processing chain in a GNSS receiver by introducing undesired biases.

1.2.2 Post-Correlation Methods

There are numerous approaches to combat RFI signals in the tracking and navigation domains of a GNSS software receiver.

Extended coherent integration time can be successively applied to cancel the multipath effects as demonstrated by Ren (2014) and Petovello et al (2008a). However, users' dynamics and oscillator quality are limiting factors when increasing the coherent

integration time. Moreover, extended coherent integration time may not help while dealing with strong RFI signals.

Monitoring the carrier-to-noise ratio values is an effective way to detect Pulsed and CW interference signals according to Balaei et al (2009) and Thompson et al (2010). However, the major drawback of the C/N_0 approach of interference detection is that the carrier-to-noise ratio can degrade not only because of interference, but also due to environmental change (for instance, when the user travels between open-sky and foliage). As a result, the C/N_0 method cannot be not fully reliable and additional RFI identification techniques should be used in parallel.

Several contributions focused on spoofing signal detection and mitigation within the tracking domain of a GPS software receiver. For instance, Cavaleri et al (2010) showed that a Cross-Ambiguity Function (CAF) distortion could be exploited to identify a spoofing attack. Specifically, by introducing a test metric (which is calculated using the Early, Late and Prompt correlator values) that is applied against the predefined threshold, it is possible to identify a spoofing signal. Another attempt to combat spoofing was done by Jafarnia-Jahromi et al (2012), where the authors proved that the distributions of squared Prompt, Early, Late, Very Early and Very Late correlator values follow a non-central Chi-Squared distribution with two degrees of freedom, but in the presence of a counterfeit spoofing signal, the correlator output distribution does not follow the Chi-Square distribution anymore. This knowledge was used in *ibid.* to

implement a spoofer detector in the tracking domain of a vector-based GPS receiver, which was still able to provide a reliable PVT solution during a spoofing attack, which targeted few of the observable SVs.

Bastide et al (2001), Macabiau et al (2000) and Ouzeau et al (2008) proved that a multi-correlator approach might be used for CW, and WB interference detection, characterization and mitigation. The multi-correlator technique allows shape analysis of the correlation peak and consists of two main stages: FFT computation of raw correlator outputs (to detect the jamming signal) and Prony estimation (Therrien & Velasco 1993, Bastide et al 2001) of the interference parameters, such as frequency, amplitude or bandwidth.

Vector-tracking implementation approach is known for its ability to improve a software receiver's overall performance in case the GPS signal is weak or during the presence of jamming signals, as reported by Pany et al (2009) and Lin et al (2011). In particular, as showed by the two above mentioned sources, vector-tracking algorithms help mitigate the multipath effects in the Doppler domain, deal with cross-correlation effect (Balaei & Akos 2012), and reduce the squaring loss (if the coherent integration time is longer than 20 ms). In the vector-based realization of a software receiver, traditional tracking loops for signals from GPS satellites are eliminated and, instead, replaced by the navigation filter. There are several advantages of the vector-based (VB) version of the receiver: it can operate with momentary blockage of the signals from one or more satellites, it can

be better optimized than a traditional scalar-based software receiver, and it inherently provides inter-channel aiding (Petovello & Lachapelle 2006, Ward et al 2006).

The ultra-tight (also called deeply coupled) receiver, which uses the data from both GPS and Inertial Navigation System (INS), inherently has an increased level of RFI resistance (Ohlmeyer 2006). The ultra-tight GPS/INS receiver is an extension to the vector-based receiver (where individual tracking loops are eliminated and are effectively replaced by the navigation filter) due to utilization of the data from the external sensors (inertial or vision). Additionally, it was shown by Pany et al (2009) that GNSS (GPS + Galileo)/INS ultra-tight coupling provides a very robust solution for tracking signals with extremely low power levels. It was shown by Petovello et al (2008a) that in case of weak GNSS signal conditions, an ultra-tight GNSS/INS receiver has an enhanced ability to track the carrier frequency. It was further concluded that quality of the IMU plays a minor role in the overall performance of the channel filter (one filter corresponds to one GNSS satellite), which estimates the tracking errors. Instead, the oscillator quality was shown to have significant impact on the tracking and navigation performance.

The performance the GPS/INS ultra-tight integrated systems under the influence of RFI signals has also been investigated (Ohlmeyer 2006, Kim et al 2007, Gustafson & Dowdle 2003). However, these analyses were based only on a few types of interference sources (Kim et al 2007, Sheridan et al 2010), or only for high-dynamics applications (Kamel et al 2013). Important work was done by Chiou et al (2002), where the authors

tested Doppler-aided GPS/INS receivers for car applications when using different quality oscillators. The result of their work is that it is possible to reduce the PLL bandwidth due to INS aiding that in turn improves the phase jitter performance. Chiou et al (2002) also showed that for high quality stand-alone GPS measurements, quality of IMU does not significantly affect the accuracy of the Doppler estimation and phase-jitter performance. However, these tests were done for a very good quality GPS signals (with large carrier-to-noise ratio (C/N_0) values) and the authors confirmed that in the case of weak signal scenario and in the presence of RFI system performance should be studied separately. Moreover, results were shown without any interferers, and only theoretical discussion for a future work was provided.

To summarize the above, the following limitations in the previous research were found:

- Most of the research contributions were centered on RFI detection and mitigation at the antenna level, in hardware, acquisition and navigation domains.
- Several tests of the ultra-tight GPS/INS system were performed using only simulated data where high dynamics applications (flight vehicle) were considered (Gustafson et al 2000). Although an improvement in code tracking of 15 to 20 dB was demonstrated in comparison with a tightly coupled GPS/INS system, experiments were done using only simulated GPS, inertial and interference data. It should be pointed out there was an assumption that the 50 Hz data bit switching was known *a priori* in experiments fulfilled by Gustafson et al (2000). This is, of

course, an idealization because in a stand-alone GNSS receiver the assistance data is not provided to obtain data bit transitions. Therefore, special data bit transition estimation techniques should be additionally applied in a stand-alone GNSS receiver (Ren 2014).

- To the best of the author's knowledge, RFI detection abilities in the tracking domain of the VB and UT software receivers were not previously addressed. Also, no attempts were found to investigate the channel-based observations quality, while simultaneously performing the RFI detection in tracking on the channel-by-channel basis.
- Only few works evaluated tracking and navigation performance of the VB and UT receivers under the impact of strong CW interference in vehicle applications employing real GPS data.

The above limitations open the door to the research and analysis conducted in this thesis. Specifically, implementation of an interference detection algorithm within the tracking domain of vector-based and ultra-tight GPS receivers and mitigation of CW interference effects on the navigation solution are explored herein. The objectives of this thesis are described in the next section.

1.3 Research Objective and Motivation

Given the limited amount of research directed towards RFI signal detection within the tracking stage of the vector-based GPS software receiver and further usage of detection

information to mitigate the interference effects in the navigation domain, this thesis expands upon the work described in the previous section with the ultimate goal of improving the navigation performance of vector-based and ultra-tight GPS/INS software receivers in CW jamming environments.

Taking into account the shortcomings discussed in the previous section, the objectives of this thesis are the following:

1. Develop an Interference Detection (ID) module to be incorporated in the tracking domain of a GPS software receiver. The reason for this kind of implementation is the following: if there is an interference signal present, it may or may not affect the GPS signal from all observable SVs (Macabiau et al 2007). Basically, every tracked PRN should be monitored for the presence of interference. Thus, it is interesting to investigate if there are cases when interference affects some of the PRNs more than others. If so, is it possible to use the observations (Doppler and pseudorange) from less affected satellites for navigation solution computation?
2. Evaluate detection abilities of the ID unit in the presence of CW interference with changing signal power. Also, it is expected that there is a tracking threshold after which it is not possible to track and perform jamming monitoring for any of the jammed SVs.
3. Design a strategy for a GPS observation weighting using information obtained from the ID module. Because of the fact that the CW signals can affect the navigation

signals in a different manner, it is suggested to develop a special observation classification method, which will allow a proper sorting of “clean” and “corrupted” observations.

4. Assess tracking and navigation performance of the vector-based GPS receiver as well as the ultra-tight GPS/INS receiver (both accompanied by the ID and newly designed observation weighting algorithm) under influence of a strong CW signal in an open-sky scenario.

Data collection for the proposed research is a challenging task, because GPS signals should be jammed during tests; however this is not possible as transmission of RFI signals is prohibited by law. Nevertheless, data from a GNSS signal simulator is used at the initial stage to validate the developed algorithm, and real data collected on a vehicle in an open-sky scenario with injected post-mission CW interference is employed to further examine the method implemented.

A strong motivation is the fact that any interference signals (e.g., CW) pose a very serious danger for satellite-based navigation services, and although there are numerous approaches of interference detection and suppression at the antenna, hardware, and acquisition levels of a GPS receiver, it is still desirable to include interference monitoring in tracking as an additional check, because it is not always guaranteed that interference is completely removed at the preceding stages (this is especially relevant if the RFI source has a very strong power).

1.4 Author's Contributions

This research focuses on identification of a strong interference signal within the tracking domain of a GPS software receiver and mitigation of its effects in the navigation domain. Specifically, tracking and navigation performance of the VB and UT GPS/INS receivers, accompanied by the ID module, is analyzed using the data sets from simulated and real open-sky scenarios.

The main contributions of this thesis to the field of satellite-based navigation include:

1. Implementation of a software module capable of detecting CW signals in the tracking domain of vector-based and ultra-tight GPS/INS software receivers;
2. Characterization of the ID performance in tracking including when to raise the detection flag, and a discussion of its advantages and drawbacks;
3. Investigation of other metrics in the tracking domain, which can additionally identify when a CW signal is present;
4. Development of a special GPS observation weighting scheme that appropriately weights raw measurements (Doppler frequency and pseudorange) using information received from the ID and employing other signal quality parameters, available in tracking; and
5. Investigation of benefits and limitations of using the proposed ID algorithm and observation weighting scheme to mitigate interference effects in the navigation

solution while operating in an open-sky dynamic environment with a limited amount of observable GPS SVs.

All the algorithms in this thesis are implemented and evaluated in a software-based GNSS receiver platform known as GSNRx™. The GSNRx™ software receiver was developed in C++ by the Position, Location And Navigation (PLAN) Group at the University of Calgary (Petovello et al 2008c).

This thesis includes some materials (e.g. figures or text) previously published in a conference paper:

1. **Krasovski, S.,** M.G. Petovello and G. Lachapelle (2014) "Ultra-tight GPS/INS Receiver Performance in The Presence of Jamming Signals", Proceedings of the 27th International Technical Meeting of The Satellite Division of the Institute of Navigation (ION GNSS+ 2014), Tampa, Florida, September 2014, pp. 2220-2232.

The conference paper was fully written by the author during the research phase of his MSc degree. The co-authors' valuable feedback on the above materials is acknowledged. Use of the original parts from the above material in this thesis is allowed by the co-authors.

1.5 Thesis Outline

This thesis contains five chapters organized as described below.

Chapter 1 presents the background, motivation, objectives and contributions of this thesis. An overview of previous work with its shortcomings is presented to justify the choice of the research subject.

In **Chapter 2**, the basic methodology of GPS software receiver architecture is reviewed. Specifically, attention is paid to acquisition, tracking and navigation domains. Several tracking methods, which include Frequency, Phase and code Delay Lock Loops (FLL, PLL and DLL, respectively), are presented. Moreover, the Kalman Filter (KF) based tracking method is reviewed and all relevant equations for the measurement and system models are provided. Furthermore, navigation solution generation is briefly introduced and navigation filter design, which is based on the Extended KF, is also discussed. Comparison between the scalar (SC), vector-based (VB), and ultra-tight GPS/INS (UT) software receiver implementation approaches concludes this chapter.

Chapter 3 presents a strategy of RFI signal detection within a GPS receiver. Particularly, some practical results from a multi-correlator RFI detection method are presented and discussed. Choice of the multi-correlator RFI identification method for the undertaken research is also justified, and relevant equations are provided. Also, a novel observation weighting approach is presented which allows distinguishing corrupted and "clean" GPS measurements while operating in jamming environments.

Chapter 4 begins with a description of a simulated testing scenario and the equipment used. Subsequently, tracking and navigation domain results obtained using the VB and

UT receivers without and with an incorporated ID module are compared. Finally, a comparative analysis of the navigation solution accuracies obtained from all software receivers (VB, UT, VB+ID, and UT+ID) which operated in CW jamming scenario is provided.

Results obtained from processing the real data collected on a vehicle in an open-sky are presented in **Chapter 5**. Also, interference injection issues for a real-world test are addressed. Chosen equipment is discussed followed by the assessment of the tracking and navigation domain results, obtained from all four modifications of GSNRx™ which operated in jamming.

Chapter 6 summarizes and concludes the work presented in this thesis; also several steps are recommended to further expand the topic.

Chapter Two: GPS Software Receiver Architecture

2.1 Overview

This chapter describes the GPS L1 signal structure and a GPS software receiver. In particular, signal acquisition is briefly discussed along with the signal tracking algorithms. Moreover, common signal lock metrics are described, which are useful for the interpretation of the results obtained in Chapters 3, 4 and 5. Next, the GPS observation model is given and some aspects of the navigation filter design are addressed. Comparison between three various GPS receiver architectures concludes the chapter.

2.2 GPS L1 Signal Structure

This section provides an overview of the civil GPS L1 C/A signal. More detail about the GPS signal structure can be found in Misra & Enge (2011), Tsui (2005), and NavStar (2013).

The GPS satellites, travelling approximately 20,000 km above the surface of the Earth, broadcast the following signal at L1 frequency (military P(Y) code is omitted in this thesis)

$$S_{L1}(t) = AC(t)D(t)\cdot\cos(2\pi f_{L1}t + \phi) \tag{2.1}$$

where

- A is the amplitude line-of-sight signal;
- $C(t)$ is the C/A spreading (ranging) code;
- $D(t)$ is the navigation message consisting of satellite ephemeris and almanac data, ionospheric corrections, etc. (refer to NavStar 2013 for more detail);
- f_{L1} is the GPS L1 carrier frequency equal to 1575.42 MHz;
- ϕ is the carrier phase offset;

Propagation of the transmitted signal incurs some degradation caused by atmospheric effects (i.e., ionospheric and tropospheric delays), multipath, inter-system interference, thermal noise, etc. After the signal is received at the antenna of a receiver, it undergoes amplification and down-conversion; these procedures are usually referred to as signal-conditioning (see Figure 1.1). If the signal is brought to baseband, and then sampled and digitized by the ADC unit, it can be represented as

$$s(n) = AC(n - \frac{\tau}{T_s})D(n - \frac{\tau}{T_s})\cos(2\pi \cdot f_D T_s n + \phi) + \eta(n) \tag{2.2}$$

where

- n denotes the discrete nature of the signal;

- τ is the code phase delay caused by the transmission from the satellite to the receiver;

- $T_S = \frac{1}{F_S}$ is the sampling rate of a front-end and F_S is the sampling frequency;

- f_D is the Doppler frequency;

- $\eta(n)$ is the additive Gaussian noise.

2.3 GPS Signal Acquisition

The main purpose of the acquisition block (see Figure 1.1) of a GPS receiver is to search for satellites that are visible to the user and acquire the signal from them. In other words, the acquisition block aims to roughly estimate the code-phase ($\hat{\tau}$) and Doppler frequency ($\hat{f}_D$) of signals from all visible to the user satellites.

To perform the acquisition, a receiver builds the local replica of the signal that is then multiplied with the incoming signal $s(n)$ and such mixing is usually referred to as a signal correlation (Tsui 2005). Figure 2.1 shows the typical correlation unit (also known as a matched filter) of a GPS receiver (Curran 2010).

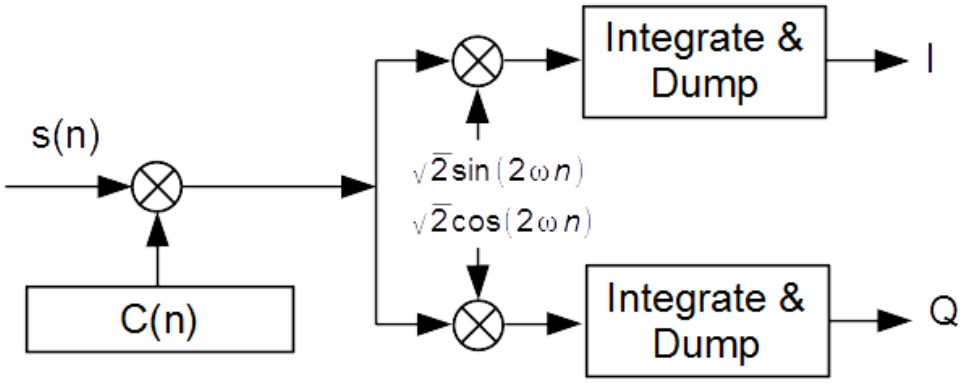

Figure 2.1: Block Diagram of a Typical Correlator in a GPS Receiver

Figure 2.1 shows that the product of signal multiplication is then integrated, or accumulated, over a period T_i, known as the integration period (or the correlation period). Note that in Figure 2.1 $\omega = \pi \cdot \hat{f}_D$. As shown by Misra & Enge (2011), the in-phase and quadrature (I and Q) correlator outputs can be approximated by

$$\begin{aligned} I(n) &= \frac{A}{2} \cdot D(n) \cdot R(\delta\tau) \cdot \cos(2\pi\delta f_D n + \delta\phi) + \eta(n)_I \\ Q(n) &= \frac{A}{2} \cdot D(n) \cdot R(\delta\tau) \cdot \sin(2\pi\delta f_D n + \delta\phi) + \eta(n)_Q \end{aligned} \tag{2.3}$$

where

- D is the navigation data bits;
- R is the autocorrelation function of the ranging code;
- $\delta\tau = \tau - \hat{\tau}$ is the code phase error over the integration interval T_i;

- $\delta f_D = f_D - \hat{f}_D$ and $\delta\phi$ are the Doppler frequency and carrier phase errors over T_i, respectively;

- η_I and η_Q are the noise components in the I and Q channels over T_i, respectively.

As Figure 2.1 shows, the result of correlation is a complex I + jQ value. At the signal acquisition stage a receiver attempts to find both code delay and Doppler frequency of the incoming signal. Simple acquisition procedure performs a serial search of the unknown code phase delay and Doppler frequency in the code-frequency uncertainty space. Thus, after multiple correlations are performed, the set of all I and Q pairs forms a Cross-Ambiguity Function (CAF), and the peak of this function represents an acquired signal (if present). From the above, it is clear that the CAF is two-dimensional, i.e. it has components in the code and frequency domains. Normally, in case of the GPS L1 C/A signal the code step is chosen to be 0.5 chip and the Doppler frequency step depends on the integration time. In the code domain, the search is performed between 0 and 1023 chips, and the scanning range in the frequency domain is ± 5 kHz (see Tsui 2005). In other words, the acquisition process tries to match the replica and the incoming signal multiple times.

Because the acquisition process is probabilistic, it is normally associated with a detection threshold. If both $\hat{\tau}$ and $\hat{f}_D$ closely match τ and f_D, respectively, and the

amplitude of the CAF exceeds a detection threshold, then the signal acquisition is deemed to be successful.

Since the C/A code is 1 ms long, the acquisition is performed on at least one millisecond of the sampled signal. Usually, up to 20 ms is used for signal acquisition (in the worst case, there will be one data bit transition after 10 ms and that can negatively affect the acquisition).

It is worth mentioning that there are multiple signal acquisition techniques, which allow fast and effective signal identification. For example, these methods include but not limited to parallel code and parallel frequency search. More detail is available in Tsui (2005) and Borio (2008).

2.4 GPS Signal Tracking

As mentioned above, the acquisition procedure provides only coarse estimates of code phase and Doppler frequency and the ultimate goal of tracking is to refine these two estimates. Specifically, the tracking procedure is a recursive process that utilizes the I and Q correlator outputs to continuously evaluate the code phase and Doppler frequency and tries to reduce the residual errors of these two parameters.

The process of tracking the carrier parameters and of tracking the code parameters can be implemented either as two independent loops (one for the code and one for the

carrier) or as one composite loop. Common tracking algorithms are addressed in the subsequent sections.

2.4.1 Frequency Lock Loop and Delay Lock Loop

Having coarsely determined the signal code phase and carrier frequency in acquisition, a Delay Lock Loop (DLL) and Frequency Lock Loop (FLL) can be employed to accurately estimate these two parameters.

Figure 2.2 and Figure 2.3 show a common structure of the DLL and FLL chains, respectively. Generally, the tracking loop consists of three fundamental blocks as shown by Ward et al (2006), namely non-linear discriminator, loop filter and Numerically Controlled Oscillator (NCO). The non-linear discriminator is responsible for computing an error function of the quantity (code or frequency) to be tracked. The loop filter tries to supress the noise in the discriminator output, and it also aims to extract the measure of the dynamics to be later used by the NCO. In other words, loop filters must be capable of finding a trade-off between the noise suppression performance and dynamics performance. Finally, the NCO is used to generate the local code and carrier replicas based on the values obtained from the loop filter. More detail description of the functionality of each of these blocks can be found in Ward et al (2006), Tsui (2005), and Curran (2010).

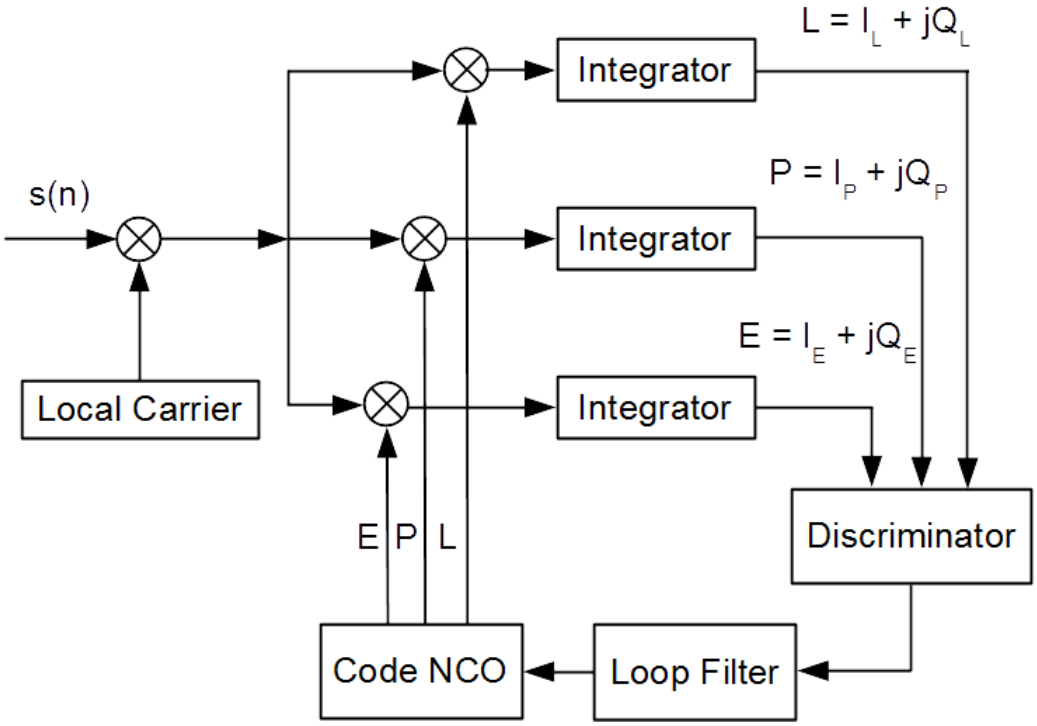

Figure 2.2: Generic DLL Block Diagram

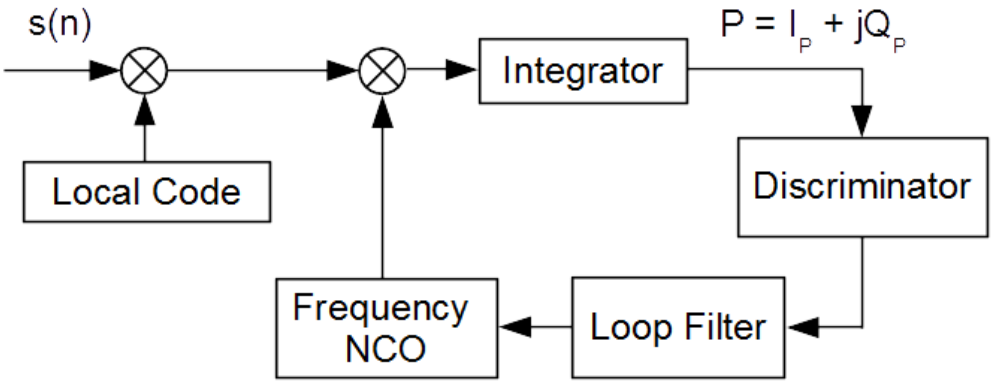

Figure 2.3: Generic FLL Block Diagram

The main parameters affecting the tracking loop performance are the discriminator type, loop filter order, loop bandwidth, and coherent integration. As stated earlier, the discriminator is a non-linear function of the error that the tracking loop is trying to

minimize. Thus, when choosing the discriminator type, one should make sure that it will be operating in its linear region, otherwise, the tracking loop will not perform reliably. The loop order determines the ability of the tracking loop to follow the dynamics, with higher dynamics applications requiring higher loop orders. Also, loop bandwidth establishes the quantity of the noise transferred from the input signal to the final estimate of the code/frequency parameter.

More detail about the discussed parameters, how they can be chosen for a specific application and how the tracking loop performance can be evaluated is available in the open literature (Ward et al 2006, Misra & Enge 2011, Curran 2010, Van Dierendonck 2006).

To understand the interference detection approach that will be discussed in Chapter 3, one should appreciate the generation of multiple code correlator samples in the DLL tracking loop. As can be seen from Figure 2.2, there are three complex I + jQ pairs in this implementation of the DLL loop. However, only two correlators, Early (E) and Late (L), are usually required by the code discriminator to assess the code correlation function (which has a triangular shape in case of the C/A spreading code). To obtain E and L correlators, a local code replica is deliberately shifted by $-d$ and $+d$ chips (where d is the code chip spacing) with respect to the best peak estimate, referred to as Prompt (P) correlator, and then the shifted replica is correlated with the incoming signal. However, as shown by Tsui (2005), sometimes more than three correlator

outputs at one integration epoch are required, hence multiple shifts can be performed to produce multiple code correlator samples (e.g., $-md$ and $+md$ shifts are used to generate m Early and Late code correlator values, respectively).

2.4.2 Phase Lock Loop

Similar to the FLL, the PLL is a recursive estimator (Misra & Enge 2011). The block diagram of the PLL tracking loop implementation does not differ from that of the FLL shown in Figure 2.3. Of course, a suitable phase discriminator should be chosen to process the I and Q values to estimate the carrier phase error. A suitably designed PLL loop can therefore be useful in the estimation of Position, Velocity and Time (PVT) as it can provide good quality estimates of the relative satellite-user dynamics (Misra & Enge 2011, Van Dierendonck 1996).

The function of the PLL is very similar to that of the FLL; it must appropriately track the signal dynamics, providing a recursively estimated control frequency to the NCO, while establishing sufficient thermal noise rejection. The increased sensitivity to the carrier parameters that the PLL offers, which are needed for PVT estimation, comes at a cost. For instance, the degree of carrier phase dynamics required to cause loss of lock in the PLL loop is generally lower than that required to induce loss of lock in the FLL. Moreover, receiver effects such as oscillator phase perturbations, which can generally be neglected in FLL analysis, must be considered in the design of the PLL tracking loop (Misra & Enge 2011, Curran 2010).

2.4.3 Kalman Filter Based Tracking

This section discusses a Kalman Filter (KF) based estimator as an alternative to the conventional DLL and PLL tracking loops. Investigations on KF-based tracking have been conducted by Psiaki (2001), Petovello & Lachapelle (2006) and Ziedan & Garrison (2004). The primary advantage of KF-based tracking over the PLL loops is that the former method provides supreme carrier phase estimation in degraded environments (see Petovello & Lachapelle 2006, O'Driscoll et al 2011).

In this thesis, one possible KF-tracking loop implementation is reviewed. Specifically, the I and Q correlator outputs are directly used in a Kalman Filter to estimate the amplitude, code phase error, carrier frequency error, carrier frequency rate error and carrier phase error. As shown by Petovello & Lachapelle (2006), the KF continuous-time system model for this kind of tracking loop implementation is the following:

$$\frac{d}{dt}\begin{bmatrix} A \\ \delta\tau \\ \delta\varphi \\ \delta\dot{\varphi} \\ \delta\ddot{\varphi} \end{bmatrix} = \begin{bmatrix} 0 & 0 & 0 & 0 & 0 \\ 0 & 0 & 0 & \beta & 0 \\ 0 & 0 & 0 & 1 & 0 \\ 0 & 0 & 0 & 0 & 1 \\ 0 & 0 & 0 & 0 & 0 \end{bmatrix} \cdot \begin{bmatrix} A \\ \delta\tau \\ \delta\varphi \\ \delta\dot{\varphi} \\ \delta\ddot{\varphi} \end{bmatrix} + \begin{bmatrix} 1 & 0 & 0 & 0 & 0 \\ 0 & 1 & \alpha & 0 & 0 \\ 0 & 0 & 1 & 0 & 0 \\ 0 & 0 & 0 & 1 & 0 \\ 0 & 0 & 0 & 0 & 1 \end{bmatrix} \cdot \begin{bmatrix} w_A \\ w_{ccd} \\ w_{clk} \\ w_{drift} \\ w_{accel} \end{bmatrix} \tag{2.4}$$

where

- $\delta\varphi$, $\delta\dot{\varphi}$ and $\delta\ddot{\varphi}$ are the phase, frequency and frequency rate errors, respectively;

- β converts units of radians into units of chips;

- α converts units of metres into units of chips;

- w_A, w_{ccd}, w_{clk}, w_{drift}, w_{accel} are the process noise values for the amplitude, code-carrier divergence due to the ionosphere, clock bias, clock drift and phase acceleration (related to the receiver dynamics), respectively.

This model uses the carrier frequency and frequency rate errors to propagate the carrier phase and code phase in time. Basically, the estimated code phase and frequency errors from Equation (2.4) are fed to the NCO to correct the local code phase and frequency.

The computation of the process noise parameters from Equation (2.4), covariance matrix of the observations as well as other details about the KF-based tracking loop design are given by O'Driscoll et al (2011) and Petovello & Lachapelle (2006).

2.5 Signal Lock Metrics

If a signal from a particular satellite is acquired and being tracked, it is important to know the quality of the tracking. To this end, signal lock detectors are designed to determine code, frequency or phase lock. Since the autocorrelation function of the GPS L1 signal is two dimensional (it is represented in the frequency and code domains),

frequency lock and phase lock detection automatically infer code lock. This section reviews signal lock detectors that are usually available in a GPS receiver.

2.5.1 Carrier-to-Noise Ratio (C/N_0)

The carrier-to-noise ratio (C/N_0), measured in the units of dB-Hz, is the ratio of the received carrier power to the power spectral density of the noise (Misra & Enge 2011).

If a very good code lock is maintained, meaning that the peak of the code correlation triangle is being properly tracked, then the carrier-to-noise ratio (C/N_0) will be highest (Misra & Enge 2011). In fact, “good” code lock essentially means “good” (or “high”) C/N_0 values as shown by Van Dierendonck (1996).

A commonly used C/N_0 estimator relies on the computation of the narrow band power (NBP) versus wide band power (WBP) ratio (Van Dierendonck 1996). The method employs 1 ms complex correlator outputs (I and Q samples) over one data bit period of 20 ms to compute the NBP and WBP values. When the NBP and WBP are found, they are divided and the resulting value is used to compute the C/N_0 (Van Dierendonck 1996). As shown by Muthuraman & Borio (2010), the C/N_0 can be estimated using

$$\left(\frac{C}{N_0}\right)_{dB-Hz} = 10\log_{10}\left(SNR_{post}\right) - 10\log_{10}\left(\frac{T_i}{2}\right) \tag{2.5}$$

where

- $SNR_{post} = \frac{A_R{}^2}{2 \cdot \sigma_n^2}$ is the post correlation Signal-to-Noise ratio

- A_R is the amplitude of the code correlation function;

- σ_n is the noise variance.

It is commonly known that GPS receivers operating outdoors provide the C/N_0 values that range from 40 dB-Hz to 50 dB-Hz (Misra & Enge 2011). A sudden drop in C/N_0 below 20 dB-Hz typically indicates that a GPS receiver failed to maintain lock on a particular satellite. However, one should be careful declaring a loss of lock in such cases because C/N_0 can also decrease due to instant signal attenuation that can be caused by partial line-of-sight signal blockage (for instance, when moving between open-sky and dense foliage). Thus, other signal lock metrics should be additionally evaluated.

2.5.2 Frequency Lock Indicator (FLI)

The FLI metric serves to evaluate the alignment of the locally generated frequency and the frequency of the incoming signal. As shown by Mongrédien et al (2006), the FLI can be calculated as

$$FLI = \frac{cross^2 - dot^2}{cross^2 + dot^2}$$
$$cross = I_{k-1} \cdot Q_k - I_k \cdot Q_{k-1} \quad (2.6)$$
$$dot = I_{k-1} \cdot I_k + Q_{k-1} \cdot Q_k$$

where

- I_k and I_{k-1} are the I-channel values at the coherent epochs k and $k-1$, respectively;
- Q_k and Q_{k-1} are the Q-channel values at the coherent epoch k and $k-1$, respectively.

As discussed by Mongrédien et al (2006), the FLI metric given in Equation (2.6) approximately measures $\cos(4\pi \cdot \delta f \cdot T_i)$. Van Dierendonck (1996) showed that the rule of thumb for choosing the detection threshold for the frequency loss of lock is $|\delta f| > \frac{1}{4T_i}$.

For instance, if $T_i = 20$ ms, then the false frequency lock is detected when the frequency error $\delta f > 12.5$ Hz.

2.5.3 Phase Lock Indicator (PLI)

The PLI used in this work measures differential power across in-phase and quadrature components to obtain an estimate of the phase alignment between the incoming and

local carrier signal replica. According to Van Dierendonck (1996), the PLI metric can be mathematically represented as

$$PLI = \frac{I^2 - Q^2}{I^2 + Q^2} \tag{2.7}$$

It can be shown that the PLI metric from Equation (2.7) approximately measures $\cos(2 \cdot \delta\phi)$. Normally, if a Costas discriminator is employed (this discriminator is insensitive to bit transition as shown by Ward et al 2006), phase loss of lock is declared when the phase mismatch is greater than 15 degrees as shown by Van Dierendonck (1996).

2.6 Navigation Solution

This section reviews a typical observation model used in GPS as well as how to compute the PVT solution, or navigation solution. Also, some aspects of Kalman Filter design are discussed. The full procedure of a PVT computation, which is a well-known but also rather complex process, will not be reviewed in detail herein. Instead, only the material relevant to this work is provided. For more details on the PVT computation, refer to Misra & Enge (2011), Noureldin et al (2013), and Grewal & Andrews (2011).

2.6.1 Observation Model

In civilian GPS receivers PVT is computed employing Doppler (pseudorange-rate) and pseudorange observations. Specifically, the measured pseudorange (PR) is obtained using the ranging C/A code and represents the time required for the signal to travel from the satellite to the receiver; pseudorange observations are ultimately used to compute the position of the user. Term “pseudo” arises because a measured pseudorange contains clock biases of the satellite and receiver (Rx) as well as other errors such as ionospheric, tropospheric, multipath, etc. The pseudorange observation to the i-th satellite can be expressed using

$$PR_i = \rho_i + c \cdot (dt_i^{SV} - dt^{Rx}) + \varepsilon_i^{PR} \tag{2.8}$$

where

- ρ_i is the geometric range between the satellite and the user receiver (m);
- c is the speed of light in vacuum (m/s);
- dt_i^{SV} and dt^{Rx} are the satellite and receiver clock biases relative to the true GPS time (s), respectively;

- ε_i^{PR} is the combined effect of satellite orbit error, troposphere delay, ionosphere delay, multipath and noise (m).

The geometric range can be further expanded as

$$\rho_i = \sqrt{\left(x_i^{SV} - x^{Rx}\right)^2 + \left(y_i^{SV} - y^{Rx}\right)^2 + \left(z_i^{SV} - z^{Rx}\right)^2} \tag{2.9}$$

where $(\bullet)_i^{SV}$ is the known coordinate of the satellite in the Earth-Centred-Earth-Fixed coordinate frame (Misra & Enge 2011), known as the ECEF frame, and $(\bullet)^{Rx}$ is the unknown coordinate of the user in the same frame.

Typically, a GPS receiver corrects the PR for the known errors using parameters obtained from the navigation message from the satellite. As discussed by Misra & Enge (2011) the main corrections available to a civil user are satellite clock offset relative to GPS time, relativity effect and ionospheric delay.

The Doppler observations, measured in Hz, represent the frequency shift caused by the relative receiver-satellite motion. When the Doppler frequency is multiplied with the GPS L1 carrier wavelength, it gives the pseudorange rate (PRR). The PRR represents the derivative of the satellite-receiver range and thus can be utilized to calculate the user velocity. As shown in (Misra & Enge 2011) the PRR model to the i-th satellite can be expressed as

$$PRR_i = \dot{\rho}_i + c \cdot (\dot{dt}_i^{SV} - \dot{dt}_i^{Rx}) + \varepsilon_i^{PRR} \tag{2.10}$$

where the dot represents the time derivative of a PR parameter and

- $\dot{\rho}_i$ is the geometric range rate between the satellite and the receiver (m/s);
- $c\dot{dt}_i^{SV}$ and $c\dot{dt}_i^{RX}$ are the satellite and receiver clock drifts (m/s);
- ε_i^{PRR} is the combined effect of satellite orbit error, troposphere delay, ionosphere delay, multipath and noise and is independent of ε_i^{PR} in the pseudorange equation.

The geometric range rate can be expressed as

$$\dot{\rho}_i = \frac{\Delta\vec{v}_i \bullet \Delta\vec{r}_i}{\rho_i} \tag{2.11}$$

where

- $\vec{v}$ is the velocity vector of the satellite or receiver;
- $\vec{r}$ is the position vector of the satellite or receiver;

- $\Delta(\bullet)_i = (\bullet)_i^{SV} - (\bullet)^{Rx}$, where $(\bullet)_i^{SV}$ is the parameter corresponding to the i-th satellite and $(\bullet)^{Rx}$ is the corresponding receiver parameter.

The effect of errors on the GPS measurements is not included in the scope of this thesis and detail can be found in (Misra & Enge 2011, Olynik 2002). Also, measurements to different satellites are usually considered independent.

Since there are four unknowns in Equation (2.8), namely the x, y, z coordinates of the receiver and the receiver's clock bias, at least four simultaneously visible satellites are necessary to form a set of equations to solve the unknown position; usually it is done using iterative techniques based on linearization as discussed in Angrisano (2010) and Misra & Enge (2011). Note that the same logic is applied when solving for the user velocity (at least four pseudorange rates are required). As shown by Grewal & Andrews (2011), the Least-Squares (LS) or Kalman Filter (KF) estimators are usually used to linearize a set of equations about an approximate user position and velocity, and solve them iteratively. The key idea is to start with rough estimates of the user position and velocity and determine them accurately using the LS or KF navigation filter.

2.6.2 Kalman Filter Design Considerations

The main difference between a Kalman Filter and Least-Squares is that the former estimator uses the system model (or state model) describing how the state vector evolves in time. In terms of the position and velocity (possibly, acceleration and attitude)

estimation, this effectively means that position and velocity (acceleration and attitude) at the previous time epoch are used to predict the position and velocity in the subsequent epoch.

As shown by Gelb (1974), the KF discrete-time system model can be written as

$$x_{k+1} = \Phi_{k,k+1} \cdot x_k + w_k \tag{2.12}$$

where

- k is the epoch number;
- x is the state vector;
- Φ is the state transition matrix between epochs k and $k+1$;
- w is the process noise vector that basically determines the amount of uncertainty in the dynamics model.

In addition, the measurement model is given by

$$z_k = H_k \cdot x_k + v_k \tag{2.13}$$

where

- z is the observation vector;
- H is the design matrix (known as geometry matrix or observation matrix);
- v is the measurement noise vector.

It is assumed that both process noise and measurement noise are both white and uncorrelated with each other, as well as uncorrelated with the state vector (Gelb 1974).

The goal of the estimation process is to find the best estimate ($\hat{x}$) of the state vector. As shown by Gelb (1974), the KF algorithm is based on the following equations:

$$\hat{x}_{k+1}^{-} = \Phi_{k,k+1} \cdot \hat{x}_{k}^{+} \tag{2.14}$$

$$P_{k+1}^{-} = \Phi_{k,k+1} \cdot P_{k}^{+} \cdot \Phi_{k,k+1}^{T} + Q_k \tag{2.15}$$

$$\begin{aligned} \hat{x}_{k+1}^{+} &= \hat{x}_{k+1}^{-} + K_{k+1} \cdot \upsilon_{k+1} \\ \upsilon_{k+1} &= z_{k+1} - H_{k+1} \cdot \hat{x}_{k+1}^{-} \end{aligned} \tag{2.16}$$

$$K_{k+1} = P_{k+1}^{-} \cdot H_{k+1}^{T} \cdot (H_{k+1} \cdot P_{k+1}^{-} \cdot H_{k+1}^{T} + R_{k+1})^{-1} \tag{2.17}$$

$$P_{k+1}^{+} = (I - K_{k+1} \cdot H_{k+1}) P_{k+1}^{-} \tag{2.18}$$

where

- "$-$" and "$+$" denote the prediction and update stages, respectively;
- Q is the process noise matrix associated with w from Equation (2.12);
- P is the covariance matrix of the estimated states;
- R is the covariance matrix of the observations associated with v from Equation (2.13);
- υ_{k+1} is the innovation sequence vector that defines the new information brought from the measurements;
- K is the Kalman gain matrix that weights the innovation sequence vector (i.e., it determines how much of the new information should be accepted by the system);
- I is the unity matrix.

From the above it is clear that there are two fundamental stages in the KF operation: prediction (see Equations (2.14) and (2.15)) and update (see Equations (2.16) to (2.18)). The KF concept can be explained as follows: the state estimate at epoch k is used to predict the state vector at epoch $k+1$, and after the measurements at epoch

$k+1$ are available, the predicted state is updated. In particular, the state prediction process is based on the system model design, while the update stage is based on the usage of the measurements.

When designing the system model defined by Equation (2.12) the choice of the process noise w plays a paramount role because it determines the amount of uncertainty in the system. In addition to this, variances of Doppler and pseudorange observations (elements which form R matrix) must be properly set because these values are used in the KF to weight the measurements during the update stage. Specifically, analyzing Equations (2.15) and (2.17) one may conclude that if the elements of R matrix are too large, and, at the same time, the values in Q matrix are too small, then the Kalman gain matrix will be small meaning that the system will not trust observations, but rather it will rely on the system model. Conversely, if R is very small and Q is large, the elements of K will be large, indicating that the measurements should be given more trust than the system model.

Since interference can induce additional errors in the measured pseudorange and Doppler values, it is important to have an appropriate covariance model of the measurements. In other words, if GPS observations are corrupted by interference, the variances in the R matrix should be scaled properly to make the KF filter relying more on the system model rather than using erroneous observations. However, the system model should be also designed properly.

For further details, readers can refer to the open literature (Gelb 1974, Noureldin et al 2013, Grewal & Andrews 2011, Angrisano 2010, Petovello 2003).

2.6.3 Reliability Testing in Kalman Filtering

As discussed by Teunissen & Salzmann (1989) and Petovello (2003), raw GPS measurements should be tested for the presence of outliers (or blunders) prior to being used for the PVT computation. Specifically, innovation sequence testing is employed for blunder detection in Kalman Filtering as opposed to residual testing in the context of Least-Squares. The innovation sequence testing is normally performed using the KF equations as shown for example in Petovello (2003). Recall that the innovation sequence is the difference between the current observations (available at the update stage) and the predicted by the KF states (see Equation (2.16)).

In this work, innovation sequence testing was implemented using the approach described by Petovello (2003). The test statistic, which is derived using the covariance matrix of the innovation sequence, is tested against a threshold, and if the outlier is found, the corresponding biased observation is rejected. If multiple blunders are identified, the observation with the largest bias is removed and the reliability testing is repeated with the remaining observations until no more blunders are found. The confidence level used herein is 99.9%.

According to Petovello (2003) the covariance matrix of the innovation sequence can be expressed as

$$C_{\upsilon} = H \cdot P^{-} \cdot H^{T} + R \tag{2.19}$$

One may observe that Equation (2.19) is a part of the Kalman gain matrix, hence, it is always available during normal filter operation. The test statistic can then be written as

$$\gamma_i = \frac{M_i^T \cdot C_{\upsilon}^{-1} \cdot \upsilon}{\sqrt{(C_{\upsilon}^{-1})_{ii}}} \tag{2.20}$$

where

- i denotes the observation index;
- M_i^T is the shaping vector (for more detail see Petovello 2003).

Analyzing Equation (2.19) and Equation (2.20) one can deduce the following link between the test statistic and the observation covariance matrix R :

- If the variances of the observations are too large, then γ_i is very small. This means that the blunder may not be identified when testing γ_i against a predefined threshold;

- Conversely, if elements of R matrix are too small, γ_i values are large meaning that there may be too many detected blunders (i.e., the testing is very “strict”).

From the above it is clear that proper choice of the variances of Doppler and pseudorange observations is crucial to allow meaningful reliability testing.

2.7 Receiver Implementation Approaches

Generally, receiver architectures are mainly distinguished by their tracking schemes. Three receiver implementation approaches, namely scalar, vector-based and ultra-tight, are reviewed in the subsequent sections. Only a high-level interpretation of receiver architectures is provided and more information can be found in the literature (Misra & Enge 2011, Van Dierendonck 1996, Tsui 2005, Petovello et al 2008a, 2008b, Lashley 2009).

2.1.1 Scalar GPS Receiver

The scalar (also known as standard) implementation approach is shown in Figure 2.4. This architecture contains independently operating channels (one channel per signal tracked), hence no channel can corrupt another channel. Specifically, every channel comprises the correlation unit and the tracking loop, which process the baseband signal. Each tracking loop, as discussed earlier in Section 2.4, usually has a non-linear discriminator function (typically, one for code delay, Doppler and, possibly, carrier phase), loop filter and NCO (denoted as the Local Signal Generator in Figure 2.4). The

information obtained from the tracking loops (normally the pseudorange and Doppler frequency, and, possibly, carrier phase) is passed to the navigation filter (NF), which estimates position, velocity and time. However, the fact that the signals are inherently related to each other via the receiver's position and velocity is neglected.

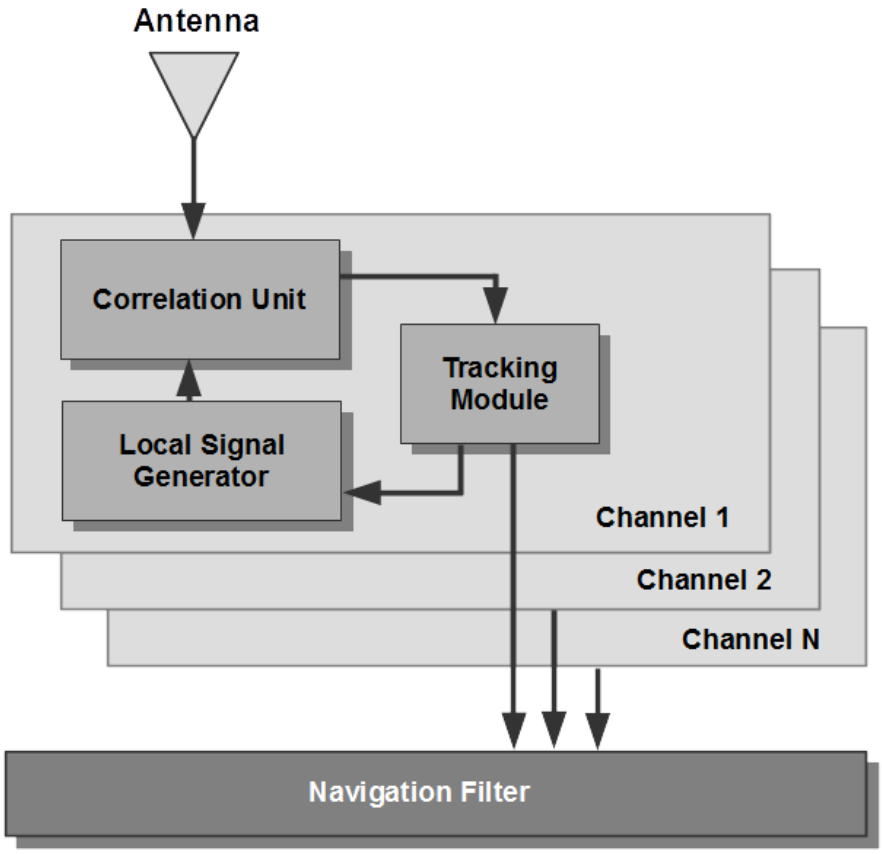

Figure 2.4: Standard GPS Receiver Architecture

More information about the scalar receiver architecture is available in Tsui (2005), Misra & Enge (2011), and Van Dierendonck (1996).

2.1.2 Vector-based GPS Receiver

Figure 2.5 shows two alternatives to the scalar receiver architecture, namely the vector based and ultra-tight implementations. The vector-based architecture will be reviewed in this section, and the ultra-tight receiver will be addressed in the next section.

The main difference between the vector and scalar architectures is that the former receiver eliminates the individual tracking loops (Petovello & Lachapelle 2006, Petovello et al 2008a, O'Driscoll et al 2011, Lashley 2009). The navigation filter is used to control the NCOs in lieu of the tracking loops. Specifically, when the position and velocity are known, the feedback to the code and carrier frequency NCOs is obtained from the reconstructed range and range rate to each satellite. Term "reconstructed" means that the pseudorange and pseudorange rate are computed based on the computed position and velocity of the user and the satellite, the latter in turn requires the knowledge about the satellite ephemeris data.

The vector-based receiver can be only initialized when the position and velocity are available. As such, scalar-based receivers are usually used to obtain the first navigation solution fix, and then the receiver transfers to vector mode.

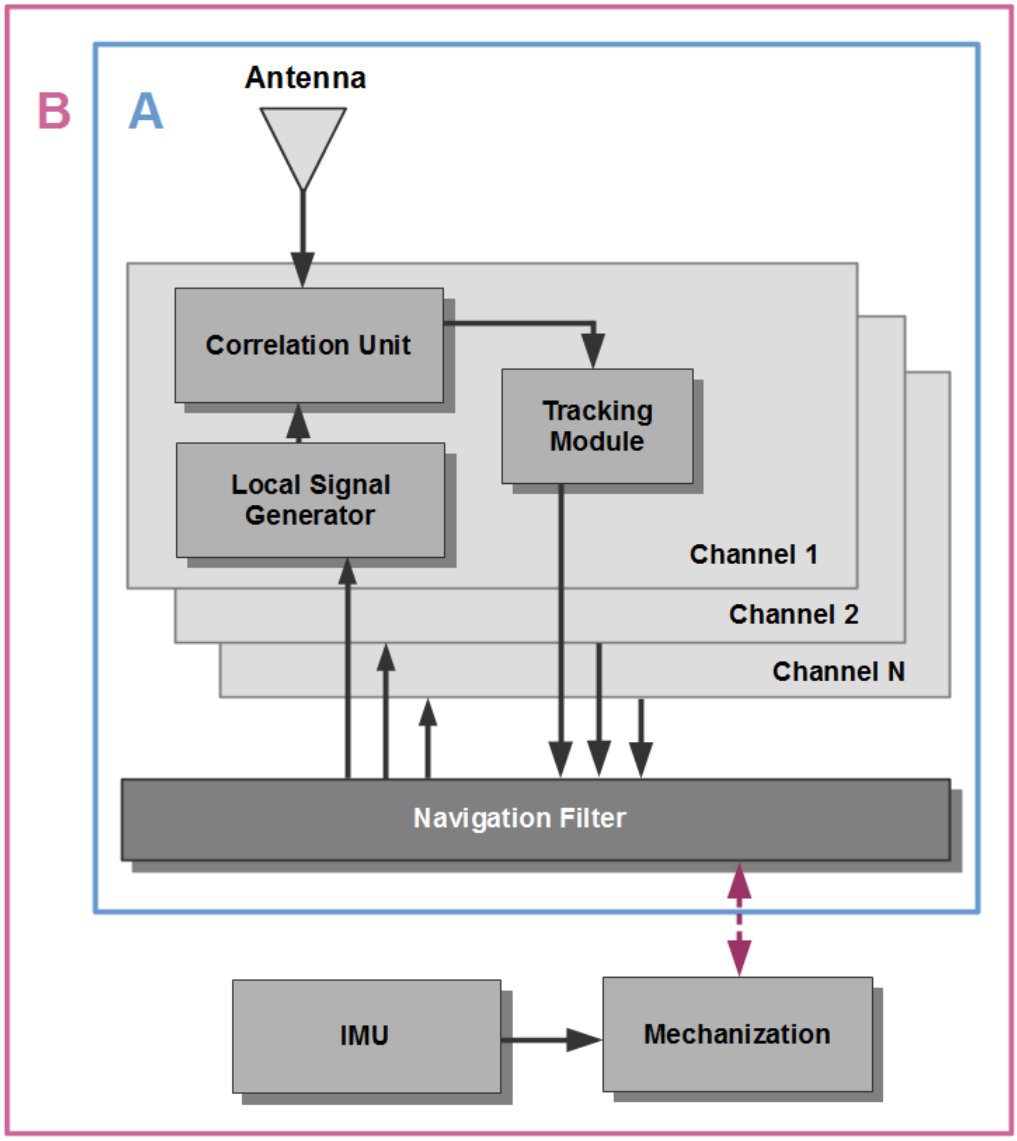

Figure 2.5: Vector-based (A) and Ultra-tight (B) GPS Receiver Architectures

The primary advantages of the vector-based architecture over the scalar-mode are the following (Petovello & Lachapelle 2006, Lashley 2009):

- It inherently provides inter-channel aiding, and this leads to enhanced code and carrier phase tracking;

- It can operate with a momentary blockage of the signal from one or several satellites;

- It offers better resistance to jamming signals (Ohlmeyer 2006);

- As shown by Ren (2014) and O'Driscoll (2011), the vector-based receivers with extended coherent integration time significantly outperform the scalar mode in degraded signal environments (e.g., multipath, urban-canyons, and foliage).

The main disadvantage of the vector-tracking architecture is that any bias or error in one channel can manifest in other channels via the navigation solution leading to overall degradation of the receiver performance.

In this thesis, the Kalman Filter-based tracking algorithm, described in Section 2.4.3, was used instead of the traditional tracking loops, and the output from the KF loop was directly passed to the navigation filter, which is also a KF. The navigation filter, in turn, controlled the local signal generators (NCOs).

2.1.3 Ultra-tight GPS/INS Receiver

As illustrated in Figure 2.5, the ultra-tight receiver is an extension to the vector-based implementation. Specifically, external sensors, such as the IMU, are used to aid the

navigation filter of the vector-based GPS receiver. In other words, the navigation solution in the ultra-tight mode is generated using both GPS and INS measurements utilizing an integrated GPS/INS navigation filter. As shown by Lashley (2009), Ohlmeyer (2006) and O'Driscoll (2011), ultra-tight GPS/INS receivers offer enhanced positioning in GPS challenged environments. Moreover, quality of the IMU has a limited role in the tracking performance of the ultra-tight mode as shown by Li et al (2010). However, quality of the front-end oscillator affects the carrier phase estimation as shown by Petovello et al (2008a, 2008b).

Usage of the IMU data implies that the mechanization equations should be implemented and all deterministic and stochastic sensor errors should be removed or compensated. However, these are well-known steps and all aspects related to inertial navigation can be found in Noureldin et al (2013), Petovello 2003, Angrisano (2010) and Grewal & Andrews (2011). Nonetheless, the state vector of the navigation filter (specifically, extended KF) of the ultra-tight GPS/INS receiver used in this work is formulated herein. Bear in mind that a three-dimensional IMU was used in this research, thus data from three gyroscopes and three accelerometers were available. The state vector of the GPS/INS navigation filter has the following form:

$$x_{23\times1} = \begin{bmatrix} P_{1\times3} & V_{1\times3} & A_{1\times3} & C_{1\times2} & B_{1\times3}^{accel} & B_{1\times3}^{gyro} & S_{1\times3}^{accel} & S_{1\times3}^{gyro} \end{bmatrix}^T \tag{2.21}$$

where

- $P_{1\times3}$ is the position vector (m);
- $V_{1\times3}$ is the velocity vector (m/s);
- $A_{1\times3}$ is the attitude vector including pitch, roll and azimuth, measured in radians;
- $C_{1\times2}$ is the vector including clock bias (m) and clock drift (m/s);
- $B_{1\times3}^{accel}$ and $B_{1\times3}^{gyro}$ are the vectors of accelerometer (m/s/s) and gyroscope (rad/s) biases, respectively;
- $S_{1\times3}^{accel}$ and $S_{1\times3}^{gyro}$ are the vectors of accelerometer and gyroscope scale factors, respectively.

2.2 Summary

This chapter discussed the GPS L1 signal structure and an overview of GPS receiver architectures. In particular, GPS signal acquisition and tracking were considered.

For a better understanding of the tracking results provided in the subsequent chapters, code, frequency and phase lock metrics were introduced. Also, pseudorange and Doppler observation models were given. Furthermore, several important topics, such as the KF observation variance design and reliability testing were highlighted. Last but not

least, three different GNSS receiver architectures were presented, namely, scalar, vector-based and ultra-tight architectures.

Chapter Three: Interference Detection in a GPS Receiver

3.1 Overview

This chapter introduces a multi-correlator FFT-based interference detection (ID) approach that is then implemented within a GPS receiver. The multi-correlator method, introduced by Macabiau et al (2001), processes code correlator samples in the tracking domain of a GPS receiver. Moreover, due to the fact that interference signals affect such GPS signal quality metrics such as Carrier-to-Noise density ratio (C/N_0) and Frequency Lock Indicator (FLI), this chapter provides the analysis of C/N_0 and FLI behaviour under the influence of strong CW signal, which can be also utilized to detect the RFI signals as shown by Betz et al (2001). Finally, a novel observation weighting strategy is presented in the presence of CW interference.

3.2 Multi-correlator Interference Detector

The ID implemented in this research is based on the multi-correlator FFT technique, proposed by Macabiau et al (2001). According to *ibid.* if the CW signal interferes with the GPS L1 C/A signal, it is possible to determine the presence of the jamming signal by analyzing multiple correlator values in the code phase domain (i.e., code samples). Even though the multi-correlator ID is capable of detecting various RFI signals (e.g., CW and FM) as shown by Bastide et al (2001) and Macabiau et al (2001), only CW interference signals were chosen for this thesis.

3.2.1 Methodology

When the incoming GPS L1 signal is corrupted by the CW signal, an additive sinusoidal component resulting from the correlation between the local code and the interference will appear on the in-phase and quadrature (I and Q) correlator channels. Bastide et al (2001) and Macabiau et al (2001) demonstrated that in the presence of CW interference, the I and Q correlator outputs at every coherent integration epoch *n* can be described as

$$
\begin{aligned}
I(n) &= \frac{A}{2} R(\delta\tau - d)\cos(\delta\varphi) + \frac{A_J}{2} T_{coh} \times D(n) \,|\, C_{\text{sinc}}(k_0) \,|\, \frac{\sin(\pi \delta f T_{coh})}{\pi \delta f T_{coh}} \times \\
&\times \cos(2\pi k_0 f_R d + \psi(n)) + n_I(n) \qquad (3.1) \\
Q(n) &= \frac{A}{2} R(\delta\tau - d)\sin(\delta\varphi) + \frac{A_J}{2} T_{coh} \times D(n) \,|\, C_{\text{sinc}}(k_0) \,|\, \frac{\sin(\pi \delta f T_{coh})}{\pi \delta f T_{coh}} \times \\
&\times \sin(2\pi k_0 f_R d + \psi(n)) + n_Q(n)
\end{aligned}
$$

where

- $I(n)$ and $Q(n)$ are the in-phase and quadrature code correlator outputs at coherent integration epoch *n*;
- A and A_J are the amplitudes of the line-of-sight GPS and CW jamming signals, respectively;
- D is the navigation data bits;
- R is the correlation function between the incoming and locally generated code;
- $\delta\tau$ is the code phase tracking error;
- d is the code correlator offset from prompt in chips;
- $\delta\varphi$ is the carrier phase tracking error;

- T_{coh} is the coherent integration time (up to 20 ms in this work);
- k_0 is the number of the C/A code spectrum line, which varies from 0 to 1022;
- $k_0 f_R \in \left[\Delta f - \frac{f_\alpha}{2}; \Delta f + \frac{f_\alpha}{2} \right]$, where $f_R = 1$ kHz is the C/A code repetition frequency and $f_\alpha = \frac{1}{T_{coh}}$;
- $C_{\text{sinc}}(k_0) = \frac{1}{1023} \frac{\sin(x)}{x} C_0(k_0)$, where $x = \frac{\pi k_0}{1023}$ and C_0 is the discrete Fourier Transform of the tracked C/A Gold Code (periodic with period 1023);
- $\delta f = k_0 f_R - \Delta f$, where Δf is the frequency difference between the jamming signal with respect to the nominal carrier frequency (assumption is made that tracked Doppler frequency is 0 Hz);
- $\psi(n)$ is the composite phase component of the interference signal and GPS signal;
- n_I and n_Q are the signals resulting from the integration of the noise samples;

One notices from Equation (3.1) that both I and Q correlator outputs are disturbed by multiplicative cosine and sine terms, respectively. In case when CW interference is not present, these additional cosine and sine terms, which are multiplied by $\frac{A_J}{2}$ in Equation (3.1), are equal to zero. As discussed in Macabiau et al (2001), the effect of the CW jamming signal on I and Q correlator outputs depends entirely on the relative amplitude of these additive terms with respect to the amplitude of the received signal. Analysis of Equation (3.1) allows one to conclude that the influence of the CW signal on I and Q code correlators is determined by the Jammer to Signal (J/S) ratio, the frequency offset of the interference signal with respect to Doppler frequency of a

satellite and the amplitude of the C/A code line which is being targeted by the jamming signal.

3.2.1.1 Interference Detection Concept

It is worthwhile to elaborate on the theoretical discussion of Equation (3.1) to illustrate how CW signals can be detected using the multi-correlator FFT approach. A MATLAB simulation was used to generate Figure 3.1, which depicts code correlator outputs at one coherent integration epoch for PRN 6 when it is and it is not affected by the CW signal (red and blue curves, respectively). In this example, the sampling frequency was 5 MHz, J/S was equal to 10 dB, CW frequency was 227 kHz and coherent integration time was 1 ms. Such sampling frequency leads to the chip spacing value of 0.2046 chips per code correlator sample. Figure 3.1 shows that in the presence of a CW signal, code correlator values are disturbed by an additive cosine component, while in the absence of the interfering signal the Auto-Correlation Function in code domain has an ideal triangular shape (Misra & Enge 2011). In other words, when the CW signal is mixed with the incoming PRN code, and the resulting signal is correlated with a local replica, additional wave-like component appears after the correlation procedure as shown in Equation (3.1). Basically, this property is exploited when detecting the interference signal. The CW detection concept is shown below.

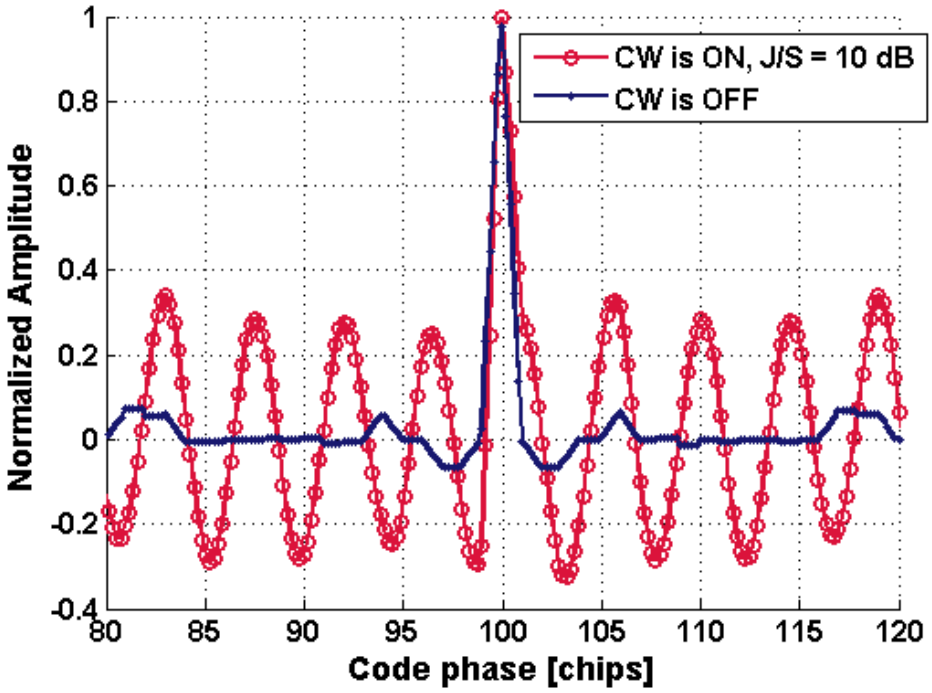

Figure 3.1: Code Correlator Output
(red: w/ interference, blue: w/o interference)

To demonstrate the procedure of CW signal detection using the multi-correlator ID approach, the Fourier transform of 5000 code correlator samples (fragments of all samples are depicted in Figure 3.1) was computed. Figure 3.2 clearly illustrates that the FFT of “clean” code samples (left plot) resulted in the spectrum of the PRN 6 code (maximum normalized amplitude is centred at 227 kHz that is the strongest spectrum line of PRN under test). The right plot in Figure 3.2 shows that the maximum value of the normalized amplitude of FFT of 5000 code correlator samples (also centred at 227 kHz) is 37 times stronger than in case of the “clean” signal. Taking into account that the CW signal frequency was set to 227 kHz, it is reasonable to conclude that the CW

signal can be successfully identified by taking the FFT of *N* code correlator samples and setting a threshold somewhere between 1 and 37.

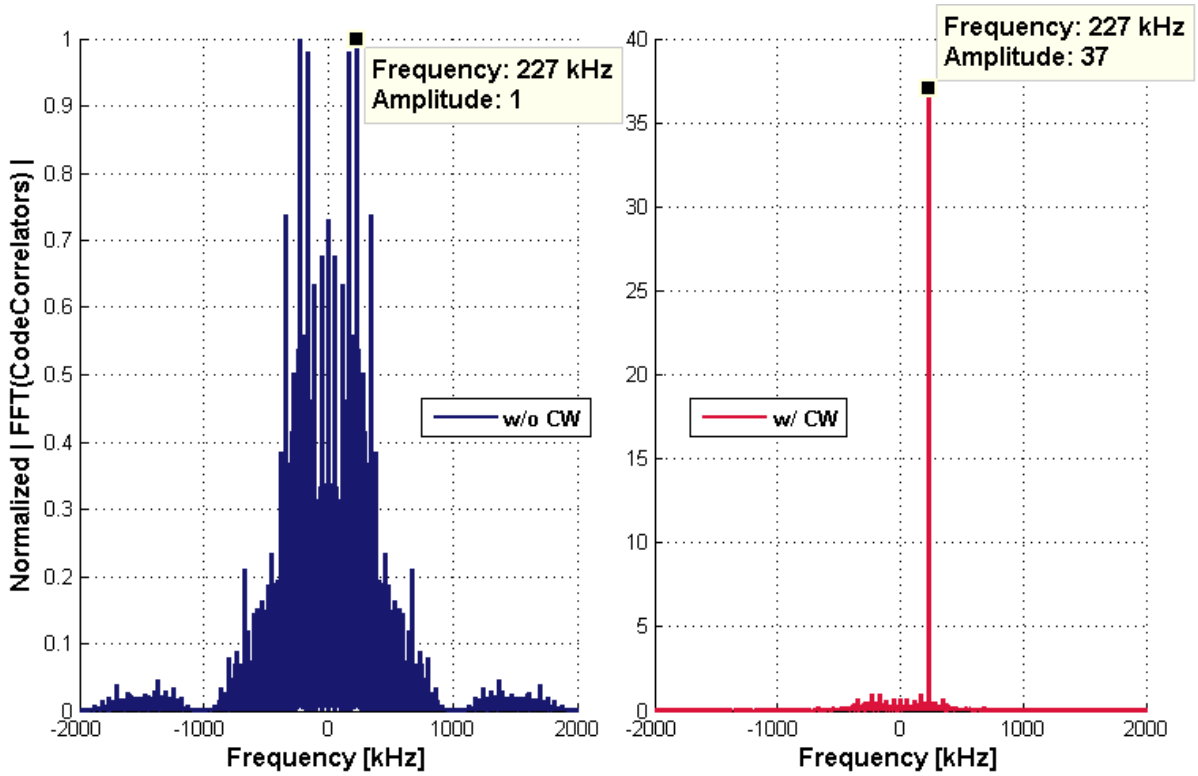

Figure 3.2: FFT of Code Correlator Samples (N = 5000)
CW Frequency = 227 kHz, J/S = 10 dB
(both spectrums are normalized by the maximum value, located at 227 kHz, obtained from the left spectrum)

As shown by Ouzeau et al (2008), at every coherent integration epoch *n* the multi-correlator ID decides whether the interference signal is present or not, using

$$
\begin{aligned}
&A \geq Threshold \\
&A = \left|\max(FFT_i) - mean(\max(FFT_{tr}))\right| \\
&Threshold = \theta \cdot std(\max(FFT_{tr}))
\end{aligned}
\tag{3.2}
$$

where $\max(FFT_i)$ is the maximum value of the *FFT* of *N* code correlators at current *n,* $\max(FFT_{tr})$ is the maximum value of the *FFT* of *N* code correlators per training epoch and θ is the scaling factor (design parameter) for the detection threshold, determined as a standard deviation of $\max(FFT_{tr})$. Note that in real scenarios, the detection threshold shown in Equation (3.2) is unique for each channel, because the standard deviation of $\max(FFT_{tr})$ accumulated during the training stage varies between channels. Also, the scaling factor θ is set to be the same for all channels and it scales the 1 sigma value which is equal to $std(\max(FFT_{tr}))$. In this work θ was set to 3; this value can be considered pessimistic (low power interference may not be detected) because the interference should be powerful enough to result in *A* that exceeds the 3 sigma of $std(\max(FFT_{tr}))$. However, this choice is reasonable due to the fact that CW interference with low power (resulting in low J/S) does not drastically affect the navigation performance of GNSS receivers as shown by Wildemeersch & Fortuny-Guasch (2010). The choice of the threshold from Equation (3.2) is discussed in more detail in Section 3.2.1.2.

3.2.1.2 Description of the ID Settings

Several important facts and assumptions should be mentioned regarding the implementation of the multi-correlator ID developed in this work.

First of all, both the amount of code correlator samples (*N*) and code chip spacing should be set properly (Bastide et al 2001). The choice of these parameters entirely depends on the desired frequency resolution of the ID, which should be correctly chosen to sample the CW signal. On the one hand, it is desirable to choose a sufficiently large number of code correlator samples *N*, so that it will allow to sample at least one period of low-frequency CW signals. On the other hand, the smaller the chip spacing, the better the high-frequency resolution. Figure 3.1 demonstrates that *N* and chip spacing were chosen to sufficiently sample several periods of CW interference signal with a frequency of 227 kHz. However, due to the fact that very small chip spacing and very large *N* will drastically slow down the overall processing speed, a compromise should be found while specifying these two parameters.

To illustrate the above, consider the following example. If the frequency of the CW jammer is equal to $f_J = 10$ kHz, then the minimum amount of code samples that will establish the required frequency (in the context of code samples, not the sampling frequency of a RF front-end) to sample one period of this interference signal should be found. Satisfying the Nyquist-Shannon's sampling theorem $f_S = 2f_J = 20$ kHz is needed. It is known that the duration of one code chip t_{chip} is approximately equal to

$\frac{1}{1.023MHz} = 0.978$ μs (Misra & Enge 2011). In the time domain, $f_S = 20$ kHz, required to sample $f_J = 10$ kHz, corresponds to $t = 50$ μs, and this t allows to compute *N*. This yields a total $N = \frac{50\mu s}{0.978\mu s} \approx 51.15$ chips to sample the CW signal with $f_J = 10$ kHz. If the code correlators are available with 0.25 chip spacing, it leads to 205 code samples per channel; this is a very significant number that will slow down the signal processing.

However, if the frequency of the CW signal is $f_J = 1000$ kHz, then $f_S = 2000$ kHz leading to $t = 0.5$ μs, and chip spacing should be chosen appropriately to sample one "quick" period of this interference signal. Since $t_{chip} \approx 1$ μs, the minimum chip spacing should be $\frac{t}{t_{chip}} = 0.5$ chip.

In the ideal case, when the potential jamming frequency is known, it is easy to choose proper *N* and chip spacing. However, this situation is rather impossible in a real scenario because normally jammer parameters are not known. Thus, relatively large numbers of code samples and smaller chip spacing should be chosen (pessimistic case). Overall, this can be considered as a major drawback of the multi-correlator RFI detection technique.

3.2.1.3 Structure of the Multi-correlator ID

Figure 3.3 illustrates the structure of the ID unit implemented in the GSNRx™ receiver. The ID is comprised of three main stages: initialization, training, and detection. Before proceeding to the description of each of these stages, two important assumptions about the ID functionality should be stated:

- It is assumed that during the training stage, signals from the GPS satellites are not affected by any jamming signals.
- The second important assumption is that in case of loss-of-lock and re-acquisition of a signal from one of the tracked PRNs, the ID does not reset. If re-acquisition happens, the ID immediately begins the interference signal detection, employing training information that was obtained beforehand. Implicitly, this assumes that the statistics collected during training still apply (i.e., there has not been a significant change in the operating environment).

In the initialization stage, the multi-correlator ID must be initialized with four parameters. These values include the number of code correlators (*N)* at every coherent integration epoch *n*, the distance between code correlator samples in chips (chip spacing), the threshold for interference detection and the training duration $T_{training}$. The choice of the amount of code correlators *N* and chips spacing is discussed in more detail in Section 3.2.1.2.

Every ID unit (one per channel in the receiver) has to complete the training procedure before proceeding to the detection stage as shown in Figure 3.3. The training stage can be described as follows: at every coherent integration instance *n*, the ID computes the FFT of *N* code correlators and stores the maximum value of the FFT output ($\max(FFT_{tr})$). At the last training iteration, the ID finds the mean and standard deviation of the accumulated maximum values that are needed to determine the detection threshold. These two statistical parameters (see Equation (3.2)) will be consecutively used for the interference detection.

Eventually, after the training stage is complete, the ID begins monitoring a channel for the presence of RFI signals.

The interpretation of the interference detection process is the following: if a PRN is affected by RFI signals, the ID detector will set a detection flag to 1, otherwise the flag is set to 0.

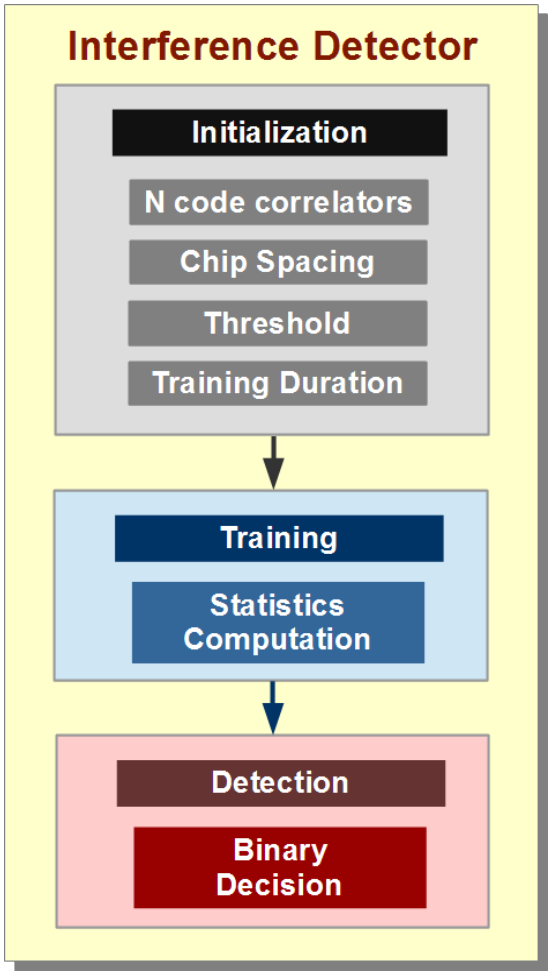

Figure 3.3: Block-diagram of the ID Module

3.2.2 Performance Evaluation of the Multi-correlator ID

The multi-correlator ID unit was implemented in the VB and UT modifications of GSNRx™ developed by researchers from the PLAN Group (Curran et al 2013, Petovello & Lachapelle 2006). Specifically, it was incorporated in the tracking domain as shown in Figure 3.4. Note that the VB and UT versions of GSNRx™, aided by the ID unit, will be referred to as VB+ID and UT+ID in this thesis.

The multi-correlator ID can also be implemented in the scalar modification of a GPS software receiver, as it was done by Macabiau et al (2001). The ID developed in this work is capable of operating in the scalar GPS receiver. However, analysis of the scalar receiver, aided by the ID, was not included in the scope of the thesis.

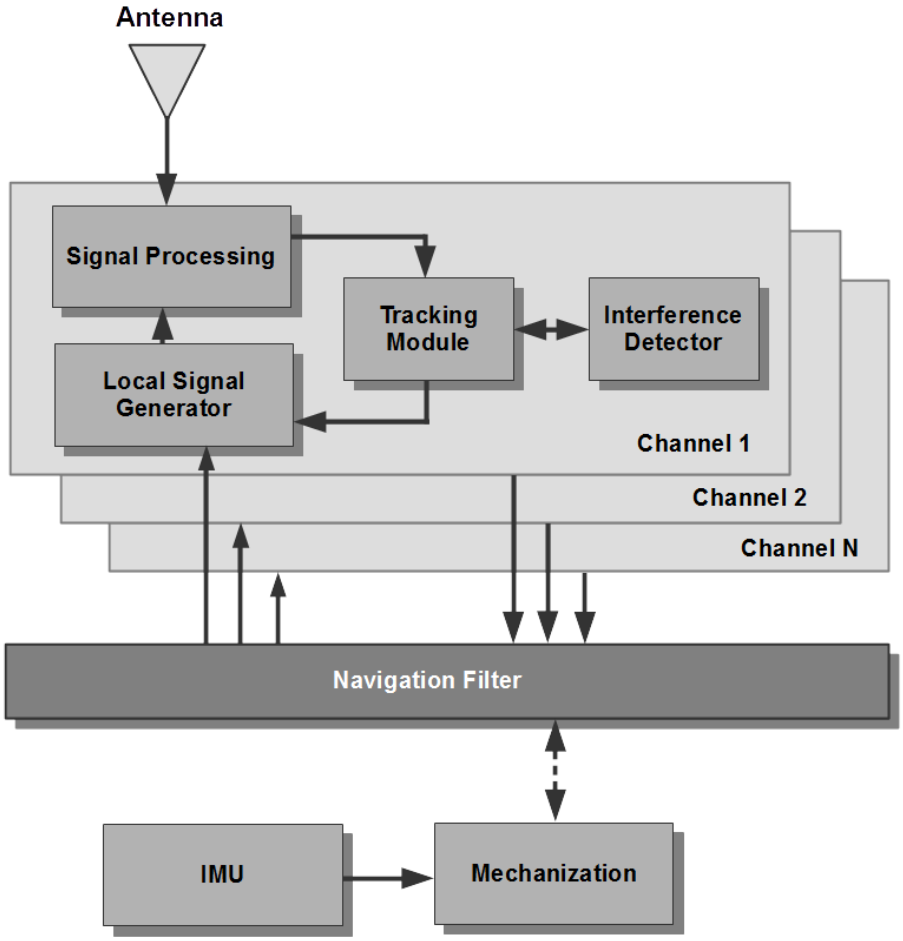

Figure 3.4: Architecture of the Vector-based or Ultra-tight GPS/INS Software Receiver Aided by the ID Unit

This section demonstrates the performance of the ID, while processing the simulated data from a Spirent GSS 7700 simulator (I/Q samples with F_s = 5 MS/s) and collected

using an NI PXIe front-end. The GPS signal power was set to be -125 dBm and the CW interference power was gradually increased from -125 dBm to -95 dBm with 2.5 dB steps (this establishes J/S ratios in the range of 0 dB and 30 dB); frequency f_{cw} of the CW signal was set to be 1575.42 MHz plus 227 kHz (to hit the strongest spectrum line of PRN 6 whose Doppler frequency was near zero in this simulation). The CW interference was injected after 40 s from the simulation start for a total duration of 65 s (interference power was not changed during the last 5 s, yielding to J/S = 30 dB).

This data is used to show two things. First, the operation of the ID module during the training stage is discussed. Second, two examples of the ID performance are provided to illustrate how one of the channels can be adversely affected by the CW interference signal, while the other one will not be affected at all.

As shown in Figure 3.3, every ID module should undergo training before proceeding to the detection mode. In this research, training duration was set to be half a second for all ID units, which is equal to 500 iterations if T_{coh} = 1 ms. Since the acquisition time varies amongst all satellites, all ID enter the detection mode asynchronously. Figure 3.5 illustrates the behavior of the ID in the vector-based receiver, when it stays in training mode. Interestingly, it was observed that $T_{training}$ > 0.5 s does not significantly improve the performance of the ID. This can be counted as an advantage of the method, because there is no need for extensive statistics to be accumulated to initiate the interference detection.

In the case of simulated data, PRN 6 was targeted by the CW signal with varying power P_J, while spectrum lines from four other PRNs were not closely located to f_{cw} (this is due to the fact that each of those PRNs had different Doppler frequencies, which effectively shifted the spectrum).

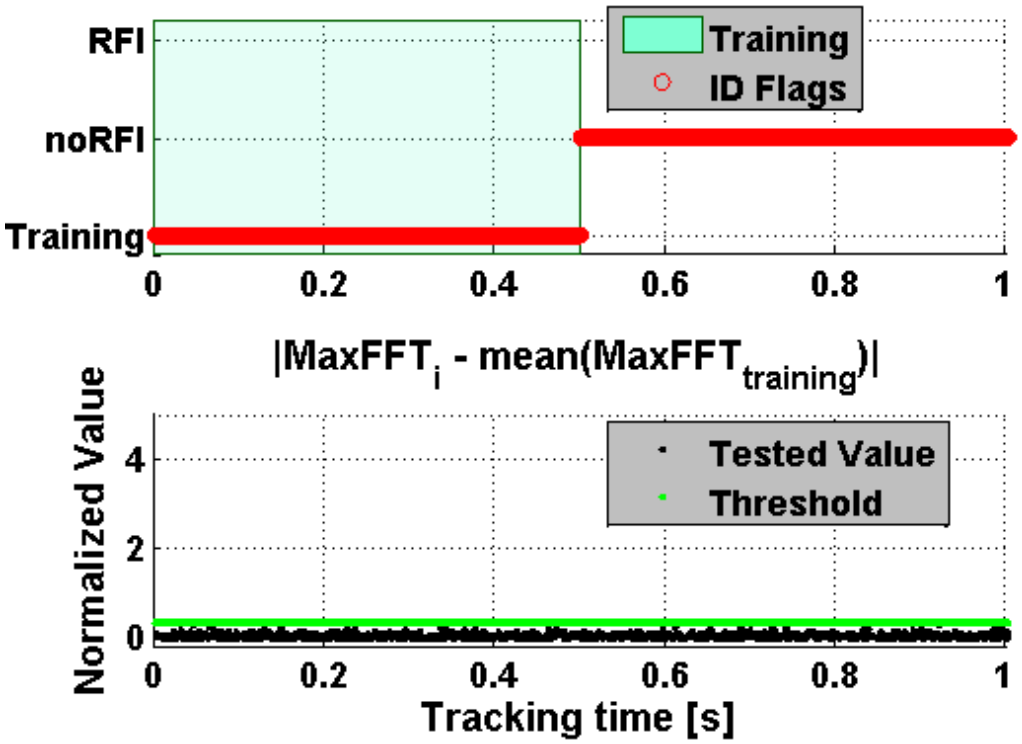

Figure 3.5: ID in Training Mode, $T_{training}$ = 0.5 s

Figure 3.6 and Figure 3.7 provide a very good example of how one channel can be more adversely affected by the jammer than another channel. In fact, the ID never identified the presence of the CW signal while monitoring the non-targeted PRN (see Figure 3.6). Note that in both cases, tested values were normalized by the maximum value of all max(FFT_{tr}) calculated during the training stage.

In contrast, Figure 3.7 shows that the ID started identifying the presence of interference signal at t = 80 s until the jammer was turned OFF. Interestingly, the ID did not identify the presence of CW signal until J/S ratio reached 15 dB. This indicates that the detection threshold from Equation (3.2) is set pessimistically. However, such a choice of the detection threshold allows to avoid multiple false alarms.

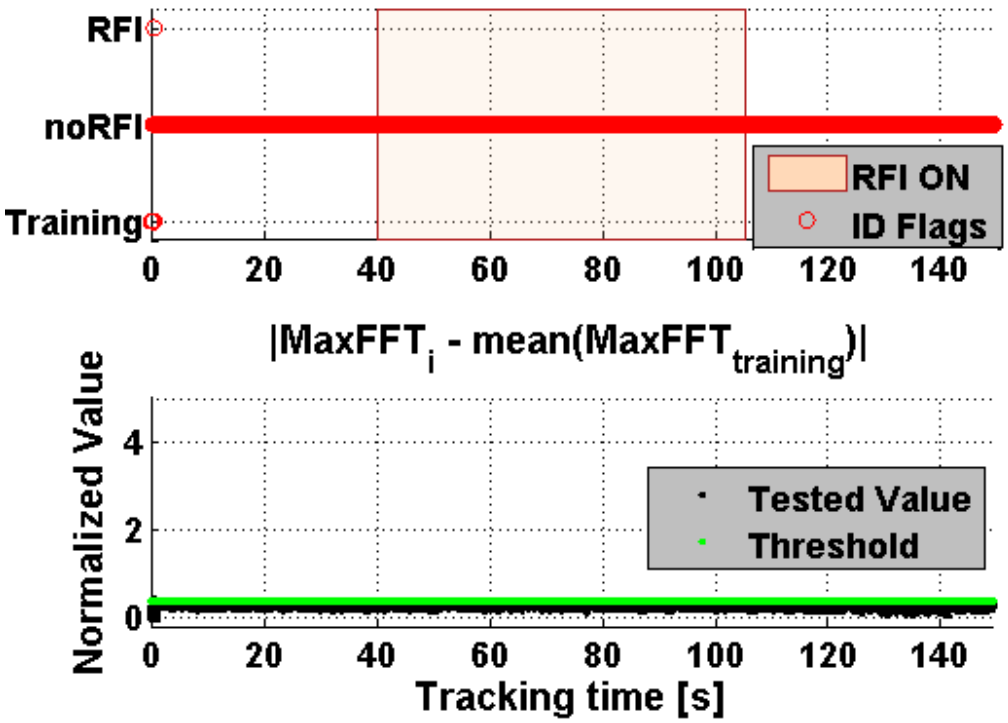

Figure 3.6: ID Performance for PRN Non-Targeted by CW Signal

Moreover, tracking and navigation performance may not be drastically affected when the J/S ratio is low and the GPS signal power is high, so that the choice of the detection threshold is reasonable for this particular scenario. The bottom plot in Figure 3.7 illustrates that A values from Equation (3.2) started growing in a stair-like manner, indicating the presence of a jamming signal.

This is entirely correlated with a gradual increase in J/S values, which were incremented by 2.5 dB in this particular scenario. Note that there are some false detections in Figure 3.7, nevertheless, they did not affect the overall performance of the software receiver.

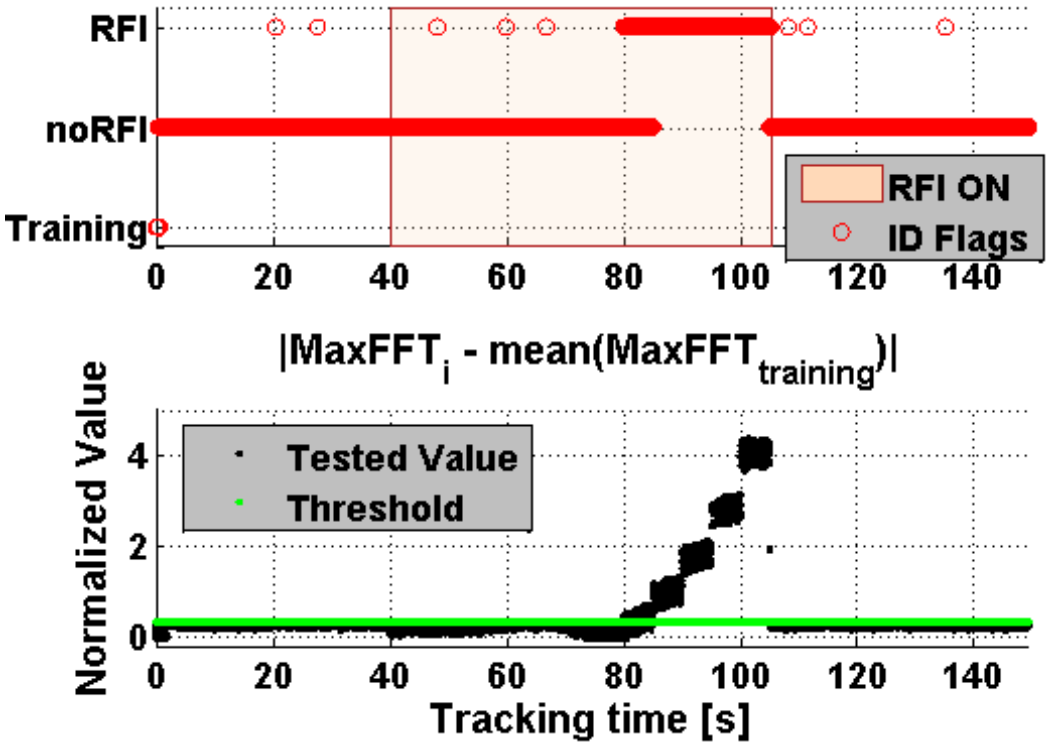

Figure 3.7: ID Performance for PRN Targeted by CW Signal

Although it is demonstrated that the CW signal can significantly affect a signal from one of the available PRNs, it should be stressed that this interference signal still affects all other available PRNs to some extent, because it raises the noise floor of the incoming signal. More detailed analysis of how the CW signal affects signals from all observable PRNs is provided in Section 3.3.

To support the discussion about the choice of the detection threshold in Figure 3.6 and Figure 3.7, Figure 3.8 shows the distribution of $\max(FFT_i)$ computed for different time periods, when the GPS signal was corrupted by CW interference and J/S varied from 0 to 35 dB. Analysis of Figure 3.8 allows one to conclude that proper selection of the detection threshold is important when initializing the ID. On the one hand, if the threshold is selected to be very small it may lead to a large number of False Alarms (FA). On the other hand, when the threshold value is too high, then medium-power CW (J/S < 20 dB) signals will not be detected, leading to an increased number of Missed Detections (MD). The separation of two groups of $\max(FFT_i)$ values (colored in brown) in Figure 3.8 is correlated with the different J/S ratios, which varied between 25 and 35 dB, while the $\max(FFT_i)$ values (green), computed when J/S was less than 20 dB, are located closer to non-jammed samples (blue).

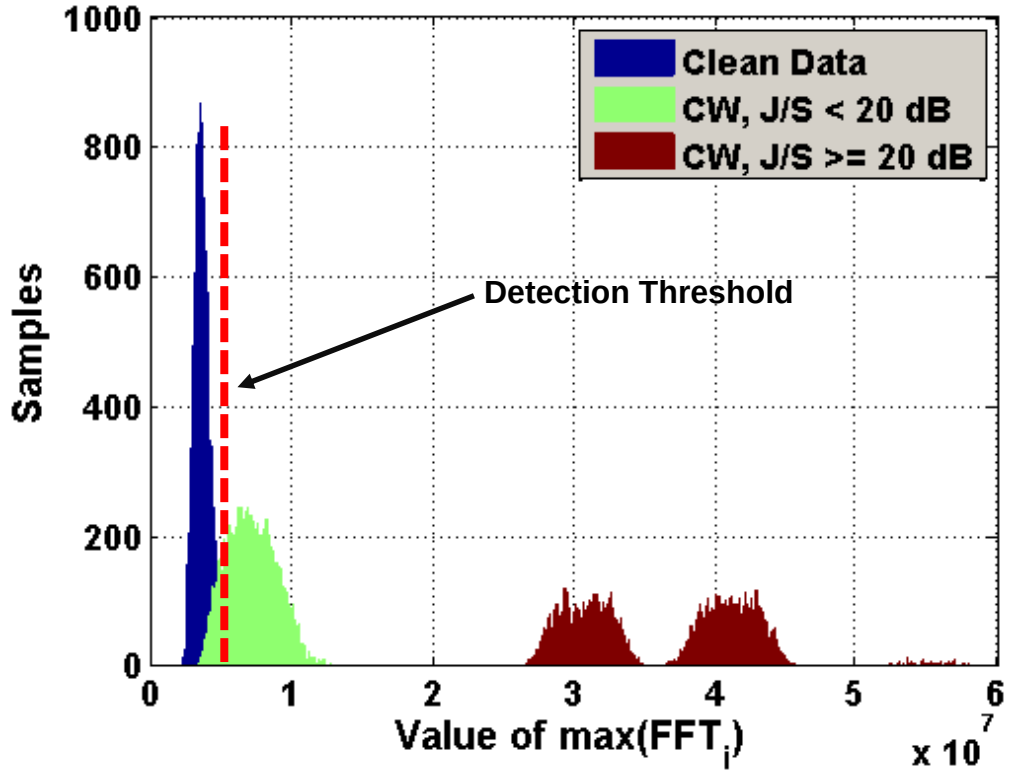

Figure 3.8: Distribution of max(FFT_i) of *N* code correlator samples (blue: w/o interference, green: w/ medium power CW, brown: w/ strong CW)

3.3 Frequency Lock Indicator and Carrier-To-Noise Ratio in the Presence of CW Jamming

It is commonly known that the C/N_0 ratio degrades in the presence of interfering signals (Ward et al 2006, Betz 2001, Balaei et al 2009, Grooves 2005). Specifically, Betz (2001) demonstrated that the effective C/N_0 degrades significantly in the presence of narrowband interference signals. The effective C/N_0 is computed after the correlation between the incoming signal with the local replica and it takes into account the increase in the noise floor which can be caused by the RFI signal. Assuming Binary Phase-Shift

Keying (BPSK) signal modulation and a chipping rate f_c, the effective C/N_0 can be written as follows:

$$\left(\frac{C}{N_0}\right)_{eff} \cong \frac{C}{N_0}\left[1+\frac{C_I}{N_0}T_c\right]^{-1} \tag{3.3}$$

where

- $\frac{C}{N_0}$ is the carrier-to-noise-power ratio without any interference;
- C and C_I are the carrier and interference signal power, respectively;
- $T_c = \frac{1}{f_c}$;
- N_0 is the noise density;

Also, Betz (2001) demonstrated that even the effective C/N_0 may not reliably reflect the impact of RFI signals on a GPS receiver's performance. Hence, other metrics, such as FLI or PLI, should also be considered in conjunction with C/N_0.

Many researchers considered the performance of carrier tracking loops in the presence of a CW signal. For instance, Jang et al (2012) derived the analytical equations representing the effective C/N_0, DLL error, and PLL error when CW interference is present. Results obtained by Jang et al (2012) show that in the worst case scenario,

when a CW signal hits the strongest spectrum line of the PRN code, the performance of the carrier tracking loop can be significantly degraded. Moreover, Karsi & Lindsey (1994) demonstrated that the higher the carrier tracking loop order, the better its resistance to carrier and phase tracking errors. In the above-mentioned work, the authors also showed that a jammer-to-signal ratio equal or greater than 5 dB can cause detuning of the carrier tracking loops.

Given this, it is interesting to observe the behavior of the effective C/N_0 and FLI metrics in the presence of a CW signal. Such analysis will help to characterize the impact of CW signals on the quality of observations generated by the receiver (Doppler and pseudorange).

3.3.1 MATLAB Simulation

As reported by Jang et al (2009) and Bastide et al (2001), CW interference negatively affects a GPS receiver only when the frequency of the interferer is near a strong spectral line of the Gold code and the difference between the spectral lines' frequencies and of the narrowband interferer is falling within low pass filter bandwidth of the tracking loop. On the one hand, due to the fact that every PRN has a unique spectrum, the CW signal with a certain frequency will affect some of the PRNs much more than others. On the other hand, if the CW signal has a significant power with respect to the GPS signal (case of large J/S ratio), it will drastically increase the overall noise floor (effective C/N_0 will drop). In such a case, the GPS receiver may suffer from poor tracking or, in the worst case, loss of lock on the signal may happen.

To demonstrate how the CW signal can affect the effective C/N_0 for one of the SVs, Figure 3.9 and Figure 3.10 were generated using a simple MATLAB simulation. Figure 3.9 illustrates the spectrum of the PRN 1; the strongest spectrum line is located at f = 42 kHz. In this example, J/S ratio was set to 25 dB, and CW frequency ranged from 37 kHz to 47 kHz. Figure 3.10 shows the degradation of the effective C/N_0 in the presence of CW interference that hits the strongest spectrum line of the PRN 1.

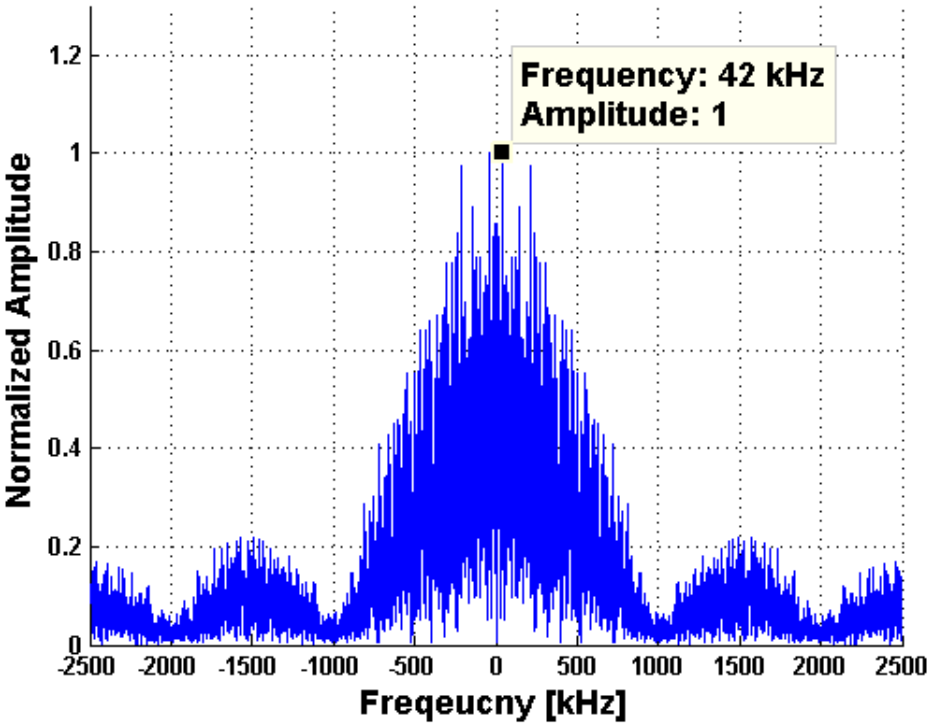

Figure 3.9: C/A Code Spectrum of PRN 1

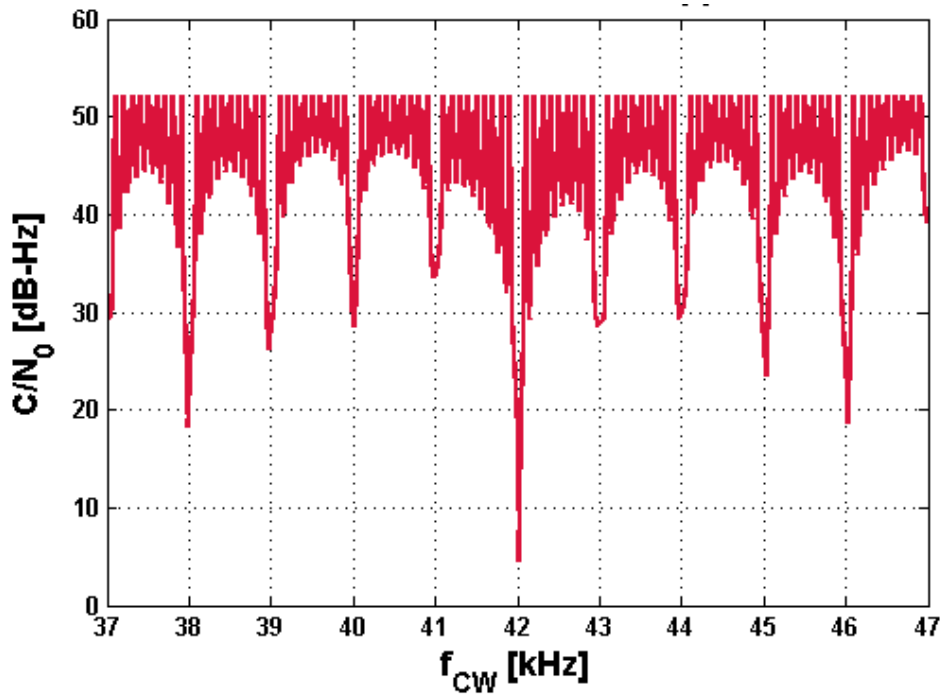

Figure 3.10: Effective C/N_0 of PRN 1 Under Influence of CW Signal
T_{coh} = 10 ms, f_{CW} = 42 kHz, J/S = 25 dB

The result shown in Figure 3.10 totally corresponds with theory and moreover, it matches the results provided in Bek et al (2013). Particularly, Figure 3.10 demonstrates that in cases when the CW signal hits the strongest spectrum line of the PRN code, effective C/N_0 experiences a significant drop. It is expected that this effect will drastically affect the tracking performance of a GPS receiver.

To expand the above discussion, Figure 3.11 shows the behaviour of the effective C/N_0 in the presence of a CW signal as a function of the CW frequency and the Doppler frequency of the incoming signal. In this example, J/S = 25. Analysis of Figure 3.11 allows one to conclude that the most negative effect of a CW signal on the effective C/N_0 occurs when the difference between the CW and Doppler frequencies is an integer

multiple of 1 kHz. Also, if the sum of the CW and Doppler frequencies is close to an integer multiple of 1 kHz, then the CW interference will also negatively affect the C/N_0, but less severely than in the first case.

Note that the intersection of blue lines observed at Doppler = 0 Hz and CW frequency $f_{CW} = 42$ kHz in Figure 3.11 corresponds to the effective C/N_0 drop in Figure 3.10 at $f = 42$ kHz.

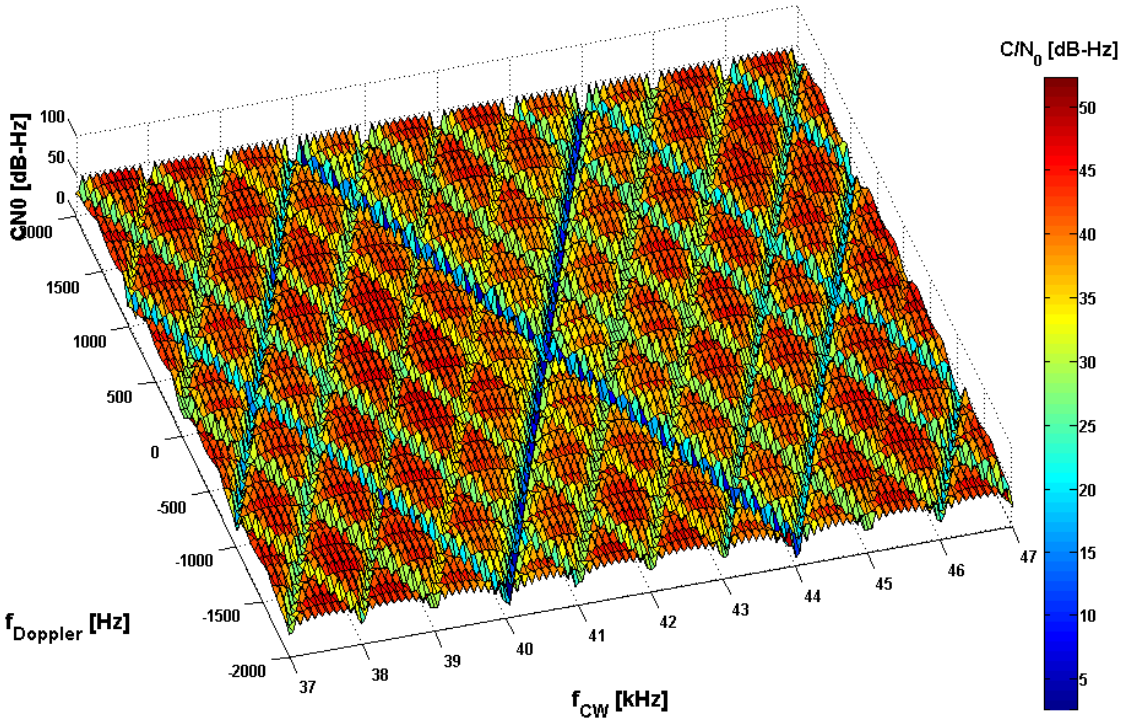

Figure 3.11: Effective C/N_0 of PRN 1 with Varying Doppler vs. CW Signal with Varying Frequency, J/S = 25 dB, T_{coh} = 10 ms.

Also, Figure 3.11 clearly illustrates that the effect of the CW signal on the effective C/N_0 may be negligible or even constructive when f_{CW} is located away from the strong

spectrum lines of the PRN 1 (this is indicated by the red zones in Figure 3.11; blue regions correspond to the C/N_0 degradation).

Having looked at the effect of CW on C/N_0, the carrier tracking performance can be assessed by the Frequency and Phase Lock Indicator (FLI and PLI, respectively) metrics discussed by Van Dierendonck (1996) and Mongrédien et al (2006), as reported in Chapter 2.

Following the approach described in Bhaskar (2014), a MATLAB simulation was performed to obtain the FLI and PLI values employing I and Q samples which were simulated using Equation (2.3). The result of this simulation is shown in Figure 3.12. In this implementation, coherent integration time was 20 ms and $1 \cdot e^5$ samples were used to obtain I and Q samples, which were later employed to calculate the mean FLI and mean PLI values (at every C/N_0 with a step of 0.5 dB). Note that the following assumptions were made: code and carrier are perfectly locked and no RFI is present.

Both FLI and PLI metrics are non-linear at lower C/N_0. This means that both of these metrics should be used with caution when operating at low C/N_0.

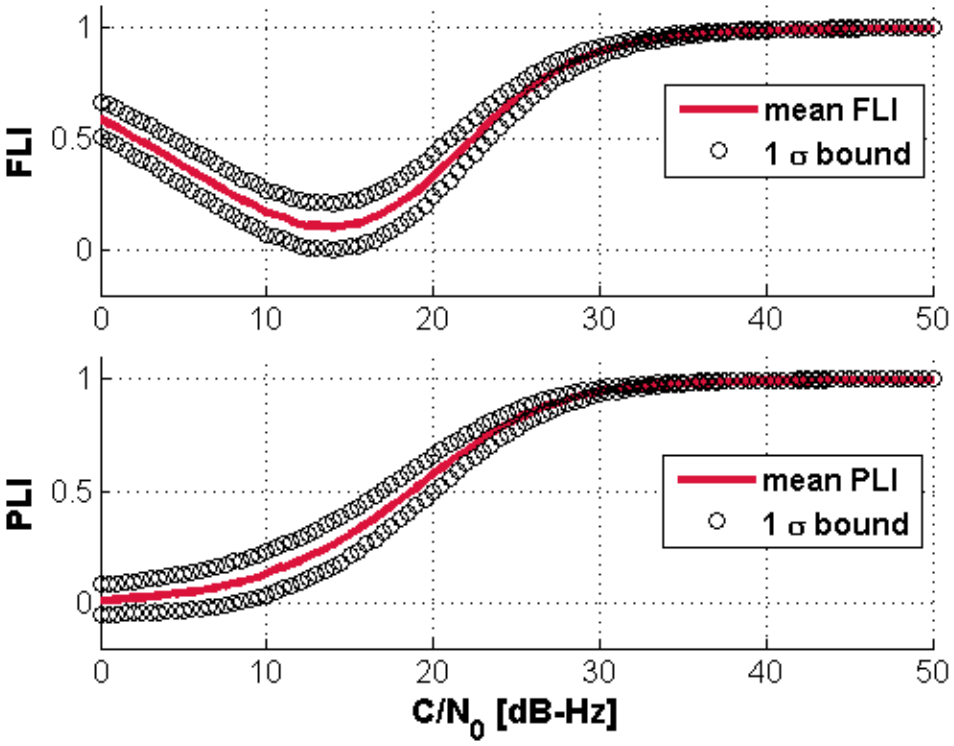

Figure 3.12: Theoretical FLI and PLI Metrics w/o Interfering Signals

Also, simulation of the FLI and PLI behaviour in the presence of a CW signal is a very challenging task. This is owing to the fact that the additional terms in I and Q channels (see Equation (3.1)), which are introduced by cross-correlation between CW interference and local replica in a GPS receiver, have a complicated structure that is determined by the following factors:

- Jammer to Signal (J/S) ratio;
- Frequency offset of the interference signal with respect to Doppler frequency of a satellite; and
- Amplitude of the C/A code line which is being targeted by the jamming signal.

However, given the results shown in Figure 3.10 to Figure 3.12, it is reasonable to assume that the CW signal will negatively affect the FLI and PLI metrics (the effective C/N_0 degrades in the presence of an interfering signal and this, in turn, reduces the FLI and PLI as shown in Figure 3.12).

Thus, it follows that C/N_0 and FLI metrics can be used in combination with the ID flags when assessing the quality of pseudorange and Doppler observations.

3.3.2 Real Data Test

To support the discussion about the C/N_0 and FLI behaviour in the presence of CW signal in Section 3.3.1, Figure 3.13 to Figure 3.15 were generated using the same data set that was used to obtain the results shown in Section 3.2.2.

Analysis of Figure 3.13 indicates that the CW signal affected all of the PRNs tracked to some extent, because the effective C/N_0 values dropped for all these satellites. Interestingly, PRN 6 and PRN 19 are less affected by the jammer, although PRN 6 was targeted by the CW signal. This is due to the fact that all satellites had different Doppler frequencies, which were varying with time due to satellite and antenna motion, so that the CW interference did not exactly hit the strong spectrum lines of all observed PRNs. This coincides well with the results observed in Figure 3.10.

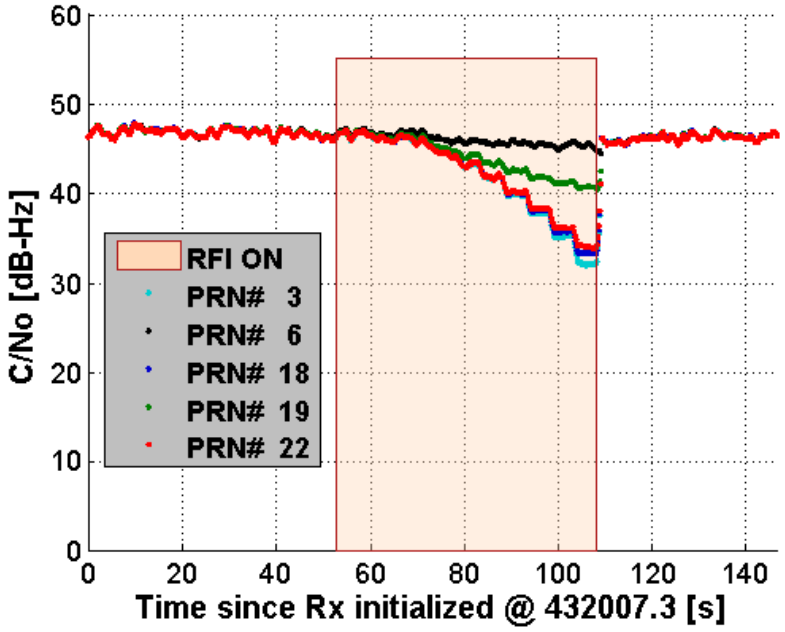

Figure 3.13: Estimated C/N_0 in the Presence of CW Jamming, J/S Ratio Ranging from 0 to 30 dB

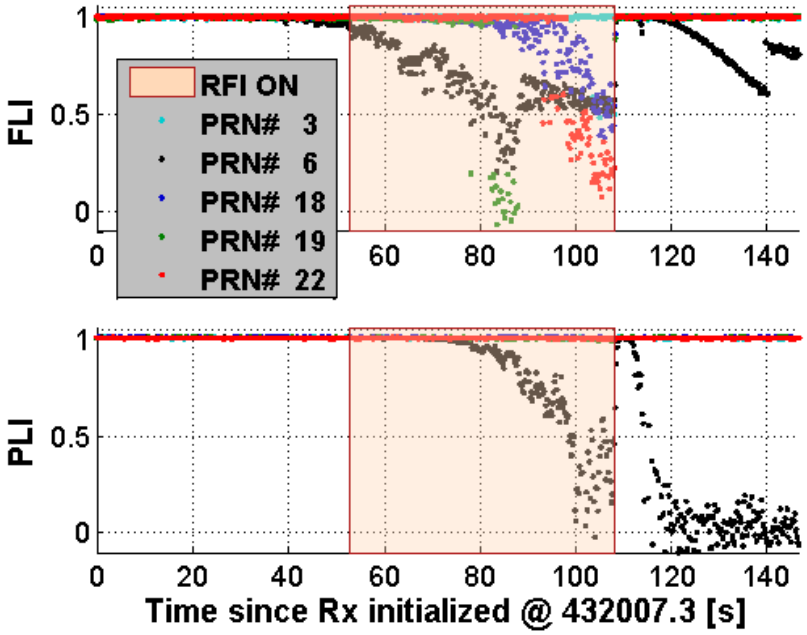

Figure 3.14: FLI and PLI in the Presence of CW Jamming, J/S Ratio Ranging from 0 to 30 dB

As discussed in Section 3.3.1, both PLI and FLI metrics degrade at lower C/N_0 values. Since interference signals impact the effective C/N_0 (see Figure 3.13), results depicted in Figure 3.14 were somewhat expected. An interesting fact is that even though the C/N_0 for PRN 3 dropped (light blue color), the frequency lock on this PRN was still maintained. This means that most likely the Doppler and pseudorange observations from PRN 3 can be used for navigation solution computation and should not be outright rejected.

It is interesting to observe the dependency between the effective C/N_0 and the FLI values illustrated in Figure 3.15. On the one hand, it was expected to see lower FLI values at lower C/N_0 (see blue and red dots). On the other hand, even though PRN 6 and PRN 19 had “good” C/N_0 values, frequency lock was significantly disturbed and this is indicated by the FLI metric (see black and green dots in Figure 3.15). This observation shows that C/N_0-based interference detection algorithms may not be reliable enough, mainly because the RFI effect on the effective C/N_0 can be constructive, and other metrics should be additionally evaluated to identify the presence of the RFI signals.

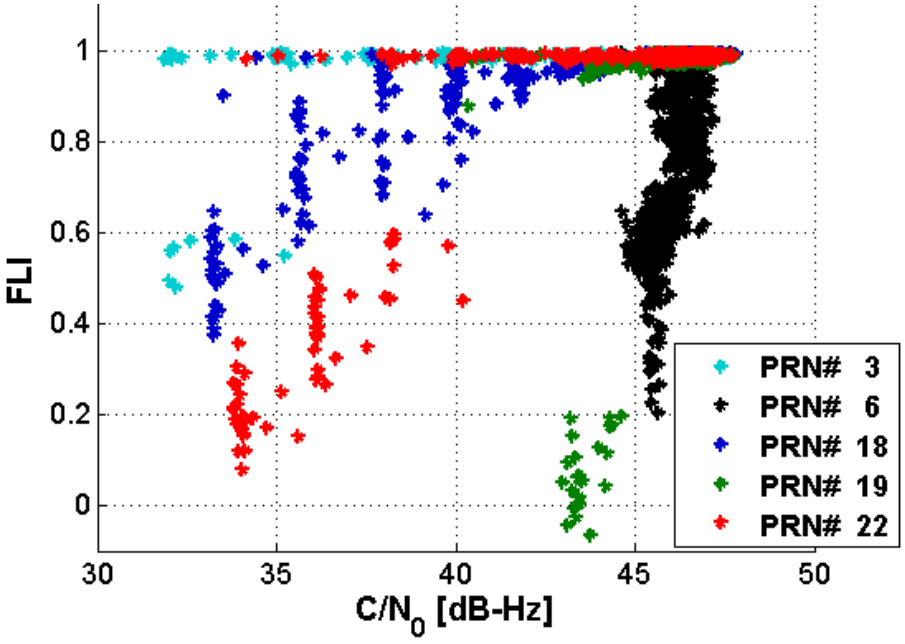

Figure 3.15: FLI vs. C/N$_0$ in the Presence of CW Jamming, J/S Ratio Ranging from 0 to 30 dB

Thus, this research suggests to use combination of the ID flag, FLI and C/N$_0$ metrics to identify whether the CW signal is present and, more importantly, whether it is strong enough to negatively affect the accuracy of pseudorange and Doppler observations.

3.4 Novel GPS Observation Weighting Approach

Typical navigation filters (both GPS and GPS/INS) rely on the assumption that the measurement covariance matrix *R* is known or can be computed. However, the error characteristics of GPS measurements vary depending upon the surrounding environments. Generally, several methods are available to estimate the GNSS measurement covariance (applicable to Doppler and pseudorange measurements in this research), namely (a) a fixed value of noise covariance, (b) an elevation weight model, and (c) a C/N$_0$ model as shown by Dhital et al (2012) and very well described in

Aminian (2011). Often these methods cannot characterize the actual measurement statistics and this can lead to sub-optimal or even unreliable performance, especially if the user navigates in areas with varying GPS signal conditions. In the context of this work, if the GPS signals are subject to jamming signals, the GPS observation covariance should be scaled properly to take into account possible effects of RFI signals.

To this end, Figure 3.16 summarizes the GPS observation weighting method proposed in this work. While based on the signal to noise ratio weighting model, the new observation covariance method takes into account cases when GPS signals are corrupted by CW interference signal with varying power. In particular, the weighting technique employs three parameters, namely ID flag, FLI, C/N_0 ratio which, in combination, give a more reliable interpretation of measured Doppler and pseudorange errors when jamming signals are present, compared to the C/N_0-based only observation weighting approach.

Because the effect of the jamming signals on the GPS signal depends on several factors, the C/N_0 observation weighting approach may not be fully sufficient since, as shown in Figure 3.11, the CW signal can affect the desired signal constructively or destructively. Usually, the C/N_0 parameter degrades in the presence of strong jamming signals (Betz 2001, Balaei 2007, Grooves 2005). However, there might be a situation when the C/N_0 does not drop significantly (constructive effect of the jamming signal). In

this case, the C/N0 method does not perform reliably. Therefore, it is necessary to check not only C/N0 values, but the FLI metric as well. Thus, several FLI and C/N0 thresholds were identified to characterize the GPS measurements properly.

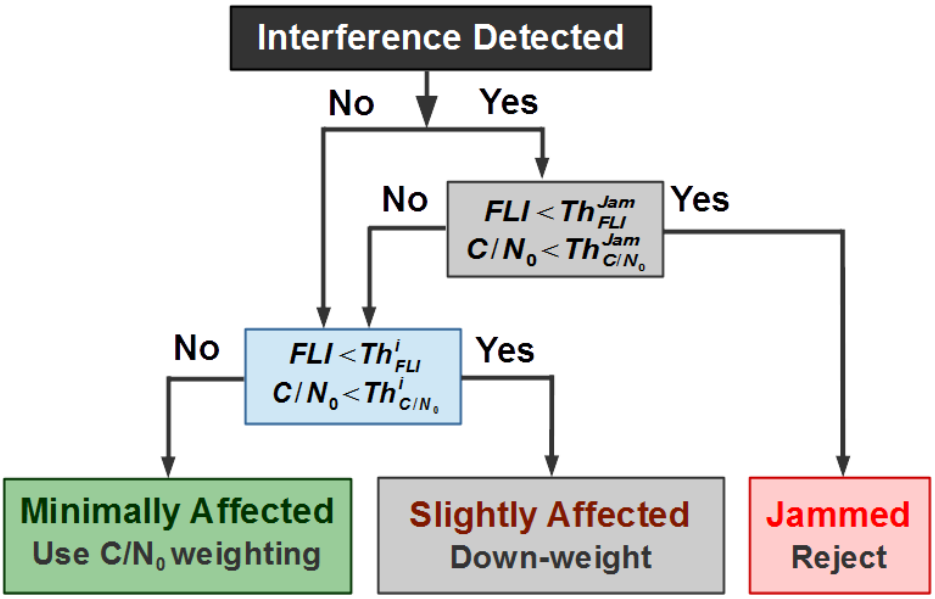

Figure 3.16: Novel Observation Weighting Scheme

From Figure 3.16 one can see that there are two sets of FLI and C/N0 thresholds, namely Th_{FLI}^{Jam}, Th_{FLI}^{i}, and Th_{C/N_0}^{Jam}, Th_{C/N_0}^{i}. The first set, Th_{FLI}^{Jam} and Th_{C/N_0}^{Jam}, is chosen to deal with observations for which the ID sets the detection flag to be 1, while another set of threshold, Th_{FLI}^{i} and Th_{C/N_0}^{i}, is designated to deal with GPS measurements which were not interpreted by the ID as being jammed. If the observation was not rejected, it is either weighted ($\lambda = 1$) or down-weighted ($\lambda > 1$) using

$$\sigma_{f_D}^2 = \lambda \cdot \sigma_{f_{D,}0}^2 \cdot 10^{\frac{(C/N_0 - C/N_{0_i}) \cdot (1 - FLI_i)}{10}} \tag{3.4}$$

$$\sigma_{PR}^2 = \lambda \cdot \sigma_{PR,0}^2 \cdot 10^{\frac{(C/N_0 - C/N_{0_i}) \cdot (1 - FLI_i)}{10}} \tag{3.5}$$

where $\sigma_{f_{D,}0}^2$ and $\sigma_{PR,0}^2$ are the nominal variances of Doppler and pseudorange observations which are scenario specific parameters set by the user at the receiver initialization stage, λ is the down-weighting coefficient, C/N_0 is the carrier-to-noise of the signal at the zenith in open sky (set as 48 dB-Hz in this work), C/N_{0_i} is the carrier-to-noise value at time i and FLI_i is the FLI value at time i.

The choice of the thresholds shown in Figure 3.16 is discussed in Chapter 4.

3.5 Summary

This chapter described the multi-correlator FFT technique of CW interference detection. The method was tested employing the simulated data and demonstrated reliable identification of a strong CW signal. The multi-correlator ID approach was chosen for this research due to several reasons. First, it can be incorporated in the tracking domain of a GPS software receiver. Second, it allows every channel to be monitored separately for the presence of various RFI signals (even with low signal power). Third, this method

may be realized in a chain with other pre-correlation RFI detection and mitigation techniques.

The behaviour of the three signal quality metrics (C/N_0, FLI and PLI) was examined in the presence of a CW signal. Based on this analysis, a novel observation weighting technique was proposed.

With this in mind, tracking and navigation performance of the VB and UT receivers, accompanied by the multi-correlator ID and the new observation weighting method will be tested on simulated and real data in Chapter 4.

Chapter Four: Performance Assessment of Vector-based and Ultra-Tight Receivers aided by Interference Detector Using Simulated Data

Chapter 3 presented the ID module and a novel observation weighting technique for use in VB and UT receivers. In this chapter, tracking and navigation performance of four receivers, namely VB, UT, VB+ID and UT+ID, are analysed using simulated data with injected CW interference. Details of the data collection and data processing procedures as well as the software receiver settings are presented first followed by the results themselves. Results address the objectives listed in Chapter 1 and include evaluation of Doppler and pseudorange tracking errors and assessment of position and velocity accuracy during pre-, in-, and post-interference injection periods. Also, the weighting of Doppler and pseudorange observations is discussed.

4.1 Experiment Details

Simulated data was collected using a GPS hardware simulator. The primary advantage of this experiment is that it was possible to have full control over the CW signal parameters (J/S ratio and interference frequency) and GPS signal parameters (Doppler frequency, signal power and elevation of all GPS satellites). The main pieces of equipment used for this part of the research were as follows:

1. Spirent GSS 7700 simulator, which was used for GPS and inertial data generation;

2. Agilent E4431B signal generator as a source of CW interference signal;

3. Spirent GSS 4766 interference combiner was used to mix the GPS and interference signals at the radio-frequency (RF) level; and,

4. National Instruments (NI) PXIe-1075 front-end with 16 bit ADC was configured to log the intermediate frequency (IF) samples with a sampling frequency of 4 MS/s. Note that the front-end did not have the AGC unit.

Generally, if the jammer power is very strong, it can cause the AGC to enter the non-linear region of operation, so that the AGC fails to match the ADC dynamic range. For a more detailed explanation of this issue, see Bastide et al (2003) and Van Dierendonck (1995). Also, if there is no AGC unit present, strong RFI signals can saturate the ADC of a front-end with limited quantization levels (1 or 2 bits) as discussed by Grewal et al (2009). In this case, performance of a RF front-end will not be reliable, restraining a GNSS receiver from reliable signal processing. When an ADC unit has a sufficiently large amount of quantization bits, it is less susceptible to strong interference (Grewal et al 2009). However, neither AGC nor ADC saturation was explicitly assessed in this work (the ADC of the NI front-end has a 16 bit quantizer that provides a very good resistance to strong RFI signals).

Only the GPS L1 C/A code signal was simulated with a constant signal power for all five satellites; the sky plot of this simulation is shown in Figure 4.1. PRN 6 is located near zenith, which establishes a Doppler frequency (f_D) of approximately 0 Hz (if the user

receiver does not move quickly). In this simulation, a GNSS antenna was simulated to be on a vehicle moving towards East with a constant speed of 10 m/s.

Attention should be also paid to the CW signal frequency generation (f_{CW}). It is known that higher elevation satellites have Doppler shifts closer to 0 Hz, and it is more convenient to jam one of the signals from these satellites using the test equipment employed. From Equation (3.1) and Figure 3.10 it was already concluded that a greater effect of the CW signal on GPS signal will be obtained when the jammer hits the frequency of the strongest code spectrum line ($f_{C/A}$) of a particular PRN. Hence, if the f_D of one of the observed satellites is relatively close to 0 Hz, f_{CW} should be equal to $f_{L1} = 1575.42$ MHz plus $f_{C/A}$ of that PRN. In this specific scenario PRN 6 was near the zenith, thus the observed Doppler frequency was nearly 0 Hz. Therefore, f_{CW} was set to be $f_{L1} + f_{C/A}$ for PRN 6, which is equal to 227 kHz (Ward et al 2006).

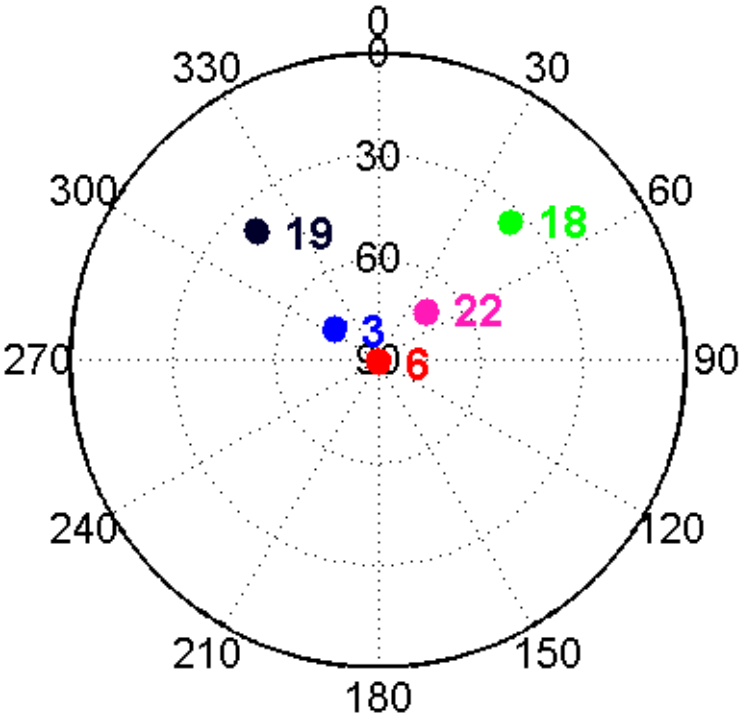

Figure 4.1: Satellite Sky Plot of the Simulated Data Set

During the test, the J/S ratio was varying from 0 dB to 35 dB with 2.5 dB increments. A CW signal was injected after 45 s for a duration of 75 s. By increasing the J/S ratio, any effects of the jamming signal on the L1 signal can be identified by the ID module, with tracking degradation expected at higher J/S levels. Note that the Spirent GSS simulator was configured to start at GPS time t = 42000 s and the simulation lasted approximately 150 s.

The ionospheric and tropospheric conditions during the test corresponded to default settings of the SimGEN software.

The SimGEN software package was used to control both the Spirent GNSS simulator and Agilent signal generator. With regard to the reference data, the SimGEN software provided the true Doppler, pseudorange, position and velocity measurements.

It is worth mentioning that in this simulated scenario, data from the inertial measurement unit (IMU) was essentially perfect. This means that there were no deterministic nor stochastic errors in the IMU measurements. Results obtained are therefore optimistic, but still useful for initial assessment of the proposed algorithms.

4.2 Software Receiver Parameters and Navigation Filter Tuning

In order to process the simulated data, all four versions of the software receiver were used. The tracking and navigation filter parameters presented in Table 4.1 and Table 4.2, respectively, were used for data processing in all cases. Also, the ID settings are listed in Table 4.3

For the results presented herein, a navigation Kalman Filter was used and employed GPS pseudorange and Doppler observations to estimate position, velocity and clock terms.

The NI PXIe-1075 front-end has a very stable ovenized crystal oscillator (OCXO) onboard, and the oscillator parameters for this type of clock were taken from NovAtel (2010).

Table 4.1: Tracking Parameters for Simulated Data Processing

FLLDLL Tracking Parameters	Unit	Value
Frequency Loop Filter Order	Unitless	2
Frequency Loop Filter Bandwidth	Hz	8.00
Delay Loop Filter Order	Unitless	1
Delay Loop Filter Bandwidth	Hz	0.10
Coherent Integration Time	ms	1
KF Tracking Parameters	**Unit**	**Value**
Amplitude Spectral Density	$dB/\sqrt{Hz}$	2.00
Code Carrier Divergence	$m/\sqrt{Hz}$	0.04
Line of Sight Spectral Density	$m/s^2/\sqrt{Hz}$	0.50
Frequency Error Threshold	Unitless	2.00
Coherent Integration Time	ms	20
Oscillator H-Parameter h0	$Hz/\sqrt{Hz}$	2.51E-26
Oscillator H-Parameter h-1	$Hz^2/\sqrt{Hz}$	2.51E-23
Oscillator H-Parameters h-2	$Hz^3/\sqrt{Hz}$	2.51E-22

Note that Doppler and pseudorange standard deviation values as well as the horizontal and vertical velocity spectral density parameters are scenario and application specific. In this particular processing it was decided to apply pessimistic values, which normally characterize the real open-sky GPS data collected on a vehicle (Chan 2013).

Table 4.2: Navigation Filter Parameters for Simulated Data Processing

Navigation Filter Parameters	Unit	Value
GPS Measurement Rate	Hz	2.00
GPS Pseudorange Standard Deviation	m	5.00
GPS Doppler Standard Deviation	Hz	0.50
C/N_0 Mask	dB-Hz	30.00
Minimum Lock Time	s	0.50
Elevation Mask	degrees	15.00
North Velocity Spectral Density	$m/s^2/\sqrt{Hz}$	2.00
East Velocity Spectral Density	$m/s^2/\sqrt{Hz}$	2.00
Vertical Velocity Spectral Density	$m/s^2/\sqrt{Hz}$	1.00
Oscillator H-Parameter h_0	$Hz/\sqrt{Hz}$	2.51E-26
Oscillator H-Parameter h_{-1}	$Hz^2/\sqrt{Hz}$	2.51E-23
Oscillator H-Parameters h_{-2}	$Hz^3/\sqrt{Hz}$	2.51E-22

The ID initialization parameters were addressed in Chapter 3, and they are summarized in Table 4.3. Moreover, as it was discussed in Chapter 3, several thresholds should be chosen to configure the novel observation weighting algorithm that is shown in Figure 3.16. Analysis of Figure 3.15 allows one to choose the following thresholds:

- If the observed FLI or C/N_0 is less than $Th_{FLI}^{Jam} = 0.7$ or $Th_{C/N_0}^{Jam} = 30$ dB-Hz, respectively, and at the same time the ID returns 1, then the observation is rejected (if the ID returns 0, the observation is accepted);

- If current FLI is less than $Th_{FLI}^{i} = 0.9$, C/N_0 is greater than $Th_{C/N_0}^{i} = 40$ dB-Hz and the ID flag = 1 (this indicates that CW interference affects the C/N_0 metric constructively, but the FLI is not fully reliable), then the observation is down-weighted (using $\lambda = 50$ in Equation (3.4) and Equation (3.5));

- In all other cases the observations are weighted using the same equations with $\lambda = 1$.

Note that when CW signal affects the computed C/N_0 constructively, the FLI metric may still drop (see Figure 3.15), and the observation from that PRN should not be trusted, i.e. variance of the measurements from this specific SV should be increased. However, one may notice that if C/N_0 is large, the resulting variance obtained from Equation (3.4) and Equation (3.5) can be small. Thus, a large down-weighting coefficient λ is required ($\lambda = 50$ was chosen in this work).

Table 4.3: ID Parameters for Simulated Data Processing

ID Parameters	Unit	Value
Training Duration	s	0.50
Chip Spacing	chip	0.20
Amount of Code Correlator Samples *N*	Unitless	151.00
Scaling Factor θ	Unitless	3.00

The IMU parameters for the ultra-tight receiver are found in Table 4.4. In this test, the Spirent GSS hardware simulator provided errorless inertial measurements (without deterministic and stochastic errors), and it was decided to apply the “pessimistic” parameters (applicable to the tactical-grade LCI NovAtel IMU used in Chapter 5) to model the errors of the “ideal” IMU.

Note that both VB and UT receivers do not operate in the vector mode at the beginning of the data processing. Initially, the standard receiver is initialized (scalar mode) and it transitions to the vector mode only after bit and navigation synchronizations are obtained for at least four SVs. Moreover, in this work satellite ephemeris was fed into GSNRx™, so that the first navigation solution was extracted within 5-6 s after the signal acquisition from four or more SVs.

Table 4.4: IMU Modelling Parameters for Simulated Data Processing

Parameters	Unit	Value
Data Rate	Hz	100.00
Gyro Parameters		
Noise Spectral Density	$\deg/h/\sqrt{Hz}$	5.558
Bias Standard Deviation (STD)	$\deg/h$	1.00
Scale Factor STD	ppm	0.20
Accelerometer Parameters		
Noise Spectral Density	$m/s/s/\sqrt{Hz}$	4.07E-3
Bias STD	$m/s/s$	0.01
Scale Factor STD	ppm	0.20

Note that the IMU parameters that are shown in Table 4.4 will be used in Chapter 5, because the LCI IMU manufactured by NovAtel was used in the real data collection. Furthermore, similar tracking, navigation and ID parameters as those used in this chapter, will be applied for data processing in Chapter 5 (differences will be discussed later on). Such choice of the parameters makes for a more direct (or “fair”) comparison between the simulated and real results.

4.3 Tracking Domain Results

In order to evaluate and compare the tracking performance of the VB and VB+ID, UT and UT+ID receivers, the tracking sensitivity of four receivers in jamming scenario was studied employing the C/N_0, FLI and PLI values observed throughout the test.

Additionally, the robustness of the code and frequency tracking in CW jamming environment was compared based on the pseudorange and Doppler tracking errors.

To compare the tracking sensitivity of the four receivers under the presence of a CW source with varying signal power and constant frequency, FLI, PLI and C/N_0 metrics are examined. Figure 4.2 and Figure 4.3 show these three metrics as a function of time for four receivers in the simulated open-sky scenario with injected CW interference.

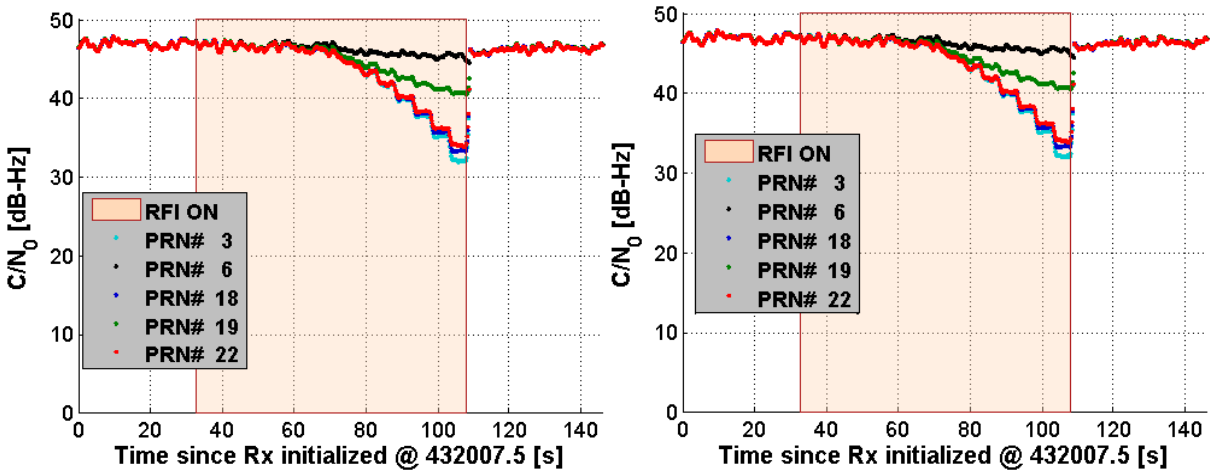

Figure 4.2: Estimated C/N_0 of all PRNs (left: VB Rx, right: VB+ID Rx)

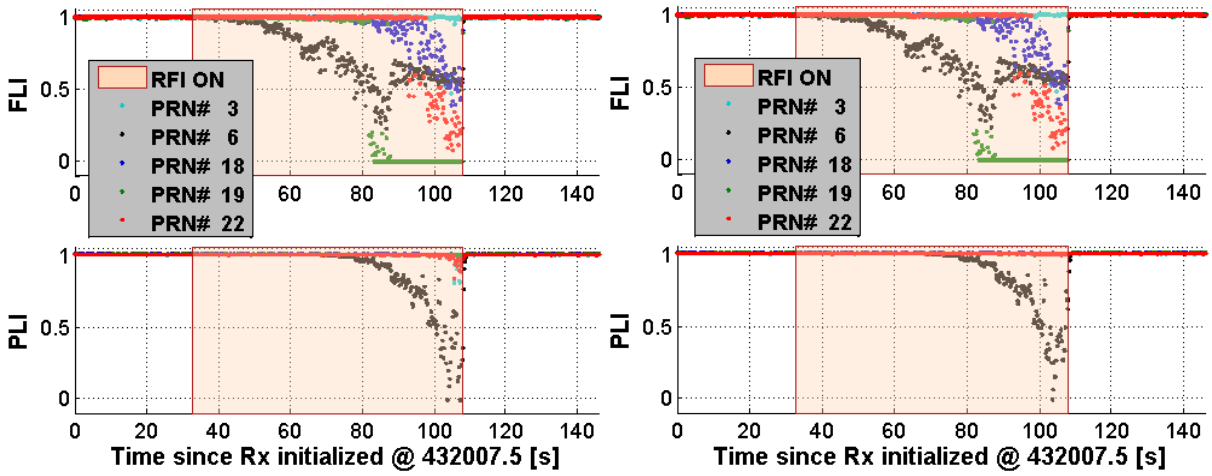

Figure 4.3: Estimated FLI and PLI of all PRNs (left: VB Rx, right: VB+ID Rx)

What is immediately apparent in Figure 4.2 is that several C/N_0 metrics do not differ between the VB and VB+ID receivers. This is due to the fact that the same tracking approach was utilized in all four receivers. Also, Figure 4.2 shows that during the impact of the CW signal, C/N_0 metric drops; this is in a good agreement with the theoretical results, provided in Chapter 3. Noticeably, the C/N_0 degradation between t = 55 s and t = 115 s has a stair-like shape, which is due to the fact that in this scenario the J/S ratio was gradually changing between 0 and 35 dB with a 2.5 dB step every 5 s. Analysis of Figure 4.2 allows one to conclude that both receivers were insensitive to J/S ≤ 15 dB (J/S = 15 dB corresponds to $t \approx$ 70 s). Additionally, Figure 4.2 clearly demonstrates how differently the CW signal can affect the computed C/N_0 estimates of the tracked PRNs: the C/N_0 metric of PRN 3, 18 and 22 degrades more significantly than the C/N_0 of PRN 6 (targeted by CW signal) and PRN 16. This supports the results obtained from MATLAB simulations in Chapter 3, i.e. CW interference can constructively affect the observed C/N_0.

Before proceeding to FLI and PLI evaluation, these values should be interpreted. The FLI metric allows the receiver to determine the frequency tracking performance for a particular SV. Logically, the PLI metric allows the receiver to gauge the phase tracking performance for a specific SV. The full range of the FLI and PLI employed in GSNRx™ is from -1 to +1. As the frequency (or phase) error tends toward 0, the FLI value will converge towards +1 (Mongrédien et al 2006, 2008, Petovello et al 2008b, Bhaskar 2014). Since poor (or "biased") frequency lock results in a loss of power on the tracked signal, a drop in the FLI should also correspond to a drop in the effective C/N_0. This dependency between the FLI and C/N_0 is valid when no RFI signals are present (Chan 2013). The FLI, PLI and C/N_0 values are computed and also filtered (using moving average filter) at each integration period (20 ms), however, all tracking results are plotted at 2 Hz rate (the reason for choosing such data rate will be addressed later in this section).

Referring to Figure 4.3 it is immediately apparent that the CW interference affected frequency tracking in a different way for various PRNs. Specifically, the FLI values for PRN 6 started decreasing at $t \approx 50$ s. Low FLI values indicate that the frequency lock may not be reliable. However, the FLI values of all other SVs were affected at $t > 80$ s, particularly, a very noticeable drop in the FLI values was observed for PRN 19 (see green dots in Figure 4.3). These observations also prove that some of the PRNs were less affected by the CW jammer than others. Also, while the FLI values for PRN 3 did not drop, the effective C/N_0 values of this PRN degraded drastically. These results

efficiently demonstrate that the C/N_0-based only observation weighting technique is not fully appropriate when operating in interference environments. Moreover, these results also support the choice of the novel observation weighting method, which was discussed in Chapter 3.

Interestingly, the PLI metric also decreased for both VB and VB+ID receivers, but only for PRN 3 (see Figure 4.3). This means that neither the frequency nor phase locks were reliably maintained by the VB or VB+ID receivers for that specific SV. Furthermore, close analysis of Figure 4.3 allows one to conclude that the PLI values of the VB receiver were slightly disturbed at $t \approx 110$ s (time when J/S = 35 dB), while the VB+ID receiver was able to maintain a perfect phase lock for all PRNs, except PRN 3.

The C/N_0, FLI and PLI values for the UT and UT+ID receivers are provided in Appendix A:. The behaviour of the carrier-to-noise ratio as well as the frequency lock indicators do not differ between all four receivers. This was expected, because these metrics are derived from I and Q correlator samples, which do not directly depend on the IMU data that is employed in the UT and UT+ID receivers.

To appreciate the tracking robustness of the four receivers in the presence of CW signal with varying power, Figure 4.4 shows the pseudorange tracking errors (which were calculated as the difference between the reference values, obtained from the Spirent GSS 7700 simulator, and the estimated GSNRx™ values). The pseudorange

observations were taken at 2 Hz and the reason for this will be discussed later in this section.

Figure 4.4 shows that all four receivers provided very similar estimated pseudoranges. Obviously, there is no difference in the estimated pseudorange values between the four receivers before the CW signal was injected. After the J/S ratio exceeded 15 dB (corresponds to $t \approx 80$ s) all receivers started providing biased pseudoranges for PRN 6 and PRN 19. This effect was expected from the analysis of the effective C/N_0 estimates. One should recall from Chapter 2 that when a GPS receiver cannot maintain a good code lock (tracking loop does not track the true peak of the correlation triangle in the code domain), the C/N_0 values will be reduced compared to the case when the code tracking loop is perfectly locked. In this situation the estimated pseudorange will be biased. Interestingly, the pseudorange estimated values from all other PRNs (3, 18 and 22) were very accurate for all four receivers. After the jamming source was removed (see $t > 110$ s in Figure 4.4), four receivers under test continued providing biased pseudorange estimates for PRN 6 and 19; noticeably, the bias was gradually increasing with time until the end of the data processing.

One should notice the difference between the estimated one-sigma uncertainties of the pseudorange estimates in Figure 4.4. The VB and UT receivers, which utilized the C/N_0-based observation weighting, produced a very small uncertainty for PRN 6 and PRN 19

(see left plots in Figure 4.4). But from the above analysis and studies of both C/N_0 and FLI values it was deduced that these two SVs are the most affected by the CW signal.

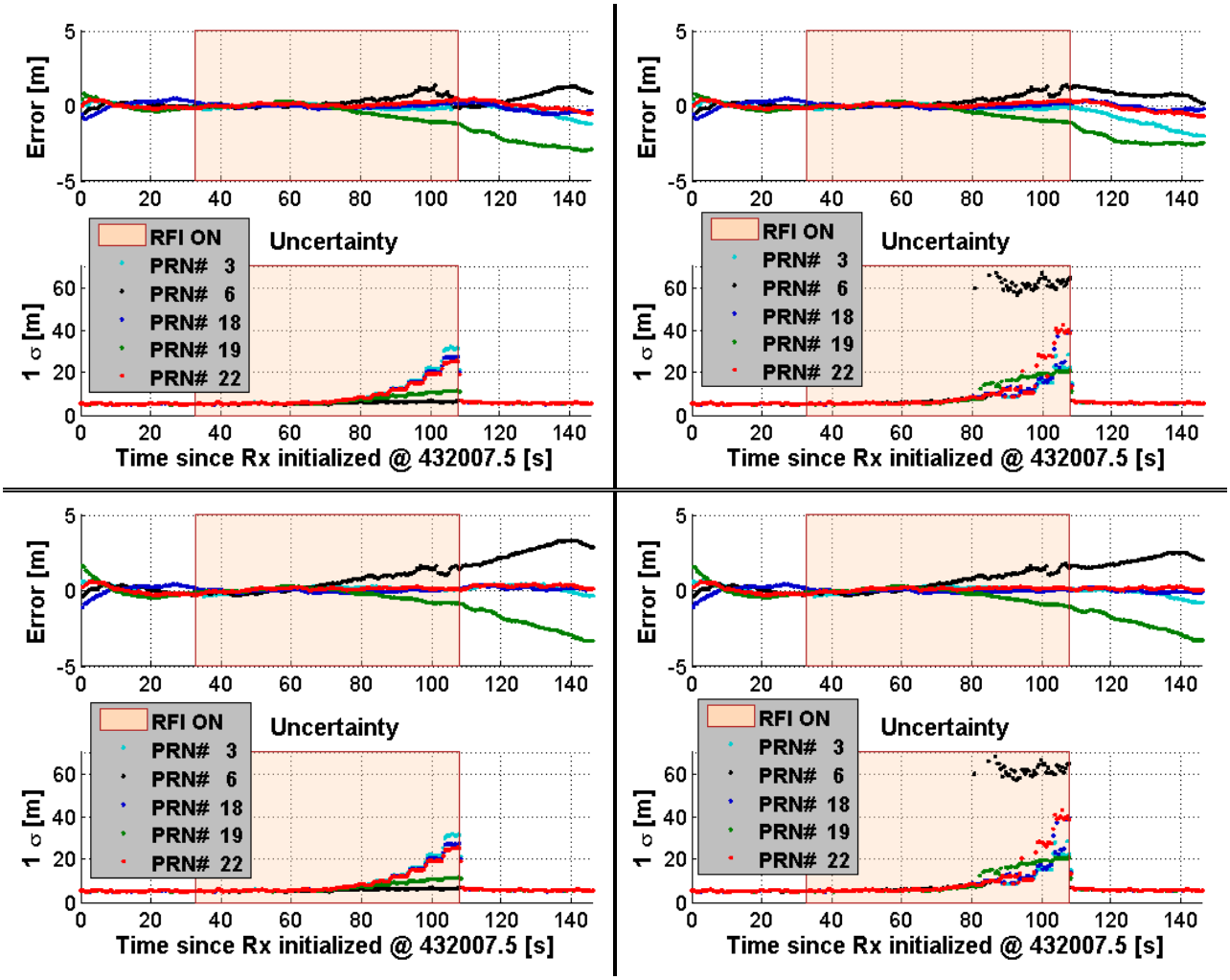

Figure 4.4: Pseudorange Errors and Pseudorange Observation Uncertainties (upper left: VB Rx, upper right: VB+ID Rx, bottom left: UT Rx, bottom right: UT+ID Rx)

However, the observation weighting scheme developed in this work generated larger pseudorange uncertainties for PRN 6 and PRN 19 than those values generated by the C/N_0 model. Thus, it is possible to conclude that the new observation weighting

technique established better variance modelling for Doppler and pseudorange measurements in a CW jamming environment, while having the same performance as the C/N_0 method when interference is absent.

Analysis of Doppler tracking errors allows one to further examine the tracking robustness of the VB, UT, VB+ID and UT+ID receivers. To this end, Figure 4.5 depicts Doppler tracking errors for all four tested receivers.

Note that the "true" tracked Doppler values were calculated employing the estimates of the tracked Doppler frequency and clock drift (converted from m/s to Hz) values using

$$\begin{aligned} f_D &= f + f_{CLK} \\ f_{CLK} &= c\dot{dt} \cdot \frac{1}{\lambda_{L1}} \end{aligned} \tag{4.1}$$

where

- f_D, f and f_{CLK} are the true tracked Doppler frequency, estimated tracked Doppler, and clock drift values, respectively;
- $\lambda_{L1} = \frac{c}{f_{L1}}$ is the wavelength of the GPS L1 frequency f_{L1} equal to 1575.42 MHz;
- c is the speed of light in vacuum (299,792,458 m/s);
- $c\dot{dt}$ is the GPS receiver clock drift (m/s);

Moreover, although Doppler measurements were available at a 50 Hz rate, they were chosen at the lower rate of 2 Hz. This is because the clock drift estimates (which were required to compute the true tracked Doppler) were available at the rate of the navigation filter (2 Hz) and equality of the data rates between the clock drift estimates and Doppler observations are necessary in Equation (4.1). Furthermore, such a data rate was suitable to draw parallels when analysing tracking and navigation domain results. For instance, a drastic change in the Doppler (pseudorange rate) frequency estimates should reflect into velocity estimates, and, similarly, an abrupt variation in pseudorange estimates should affect the estimated position.

Based on the comparison of Doppler tracking errors between the VB, VB+ID, UT and UT+ID receivers in Figure 4.5, it was found that all four receivers demonstrated very similar performance. Also, all receivers generated a Doppler error of approximately 2 Hz for PRN 3 when the J/S ratio was equal or greater than 30 dB (this corresponds to $t >$ 100 s in Figure 4.5). However, it was also found that Doppler frequency uncertainties obtained from the VB+ID and UT+ID receivers are different from those obtained from the VB and UT receivers. This is owing to the fact that the VB+ID and UT+ID receivers utilized the novel observation weighting method, which assigns larger uncertainty to those PRNs greatly impacted by CW interference. Specifically, since the FLI values for PRN 3 and PRN 19 decreased drastically, but the C/N_0 did not drop noticeably, the novel weighting approach assigned larger variances to Doppler (as well as pseudorange in Figure 4.4) observations, which are shown in Figure 4.5, compared with

variances of other three PRNs. This essentially means that both Doppler and pseudorange observations of PRN 3 and PRN 19 should be trusted less when generating the navigation solution, because these observations are less reliable and have larger errors.

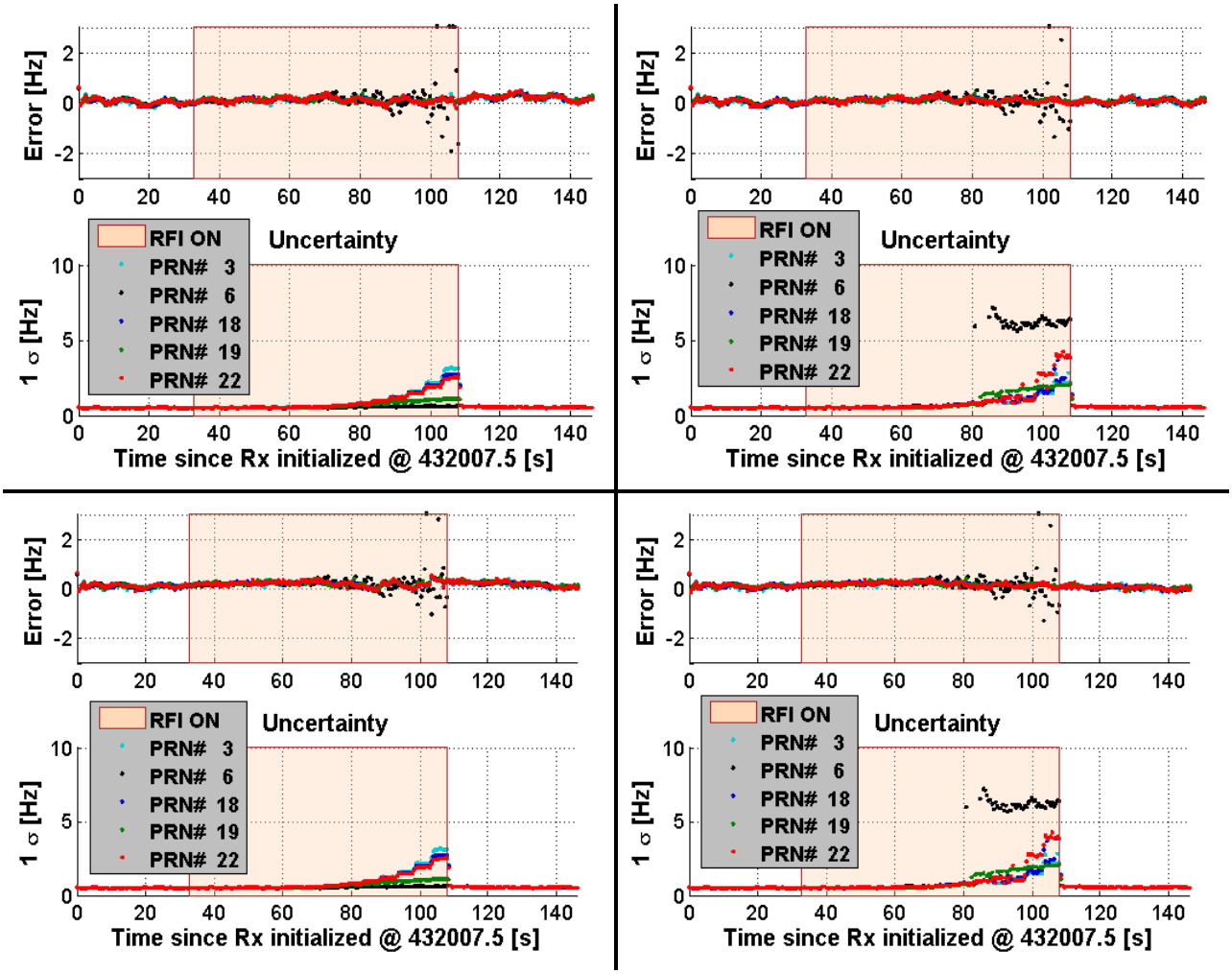

Figure 4.5: Doppler Errors and Doppler Observation Uncertainties (upper left: VB Rx, upper right: VB+ID Rx, bottom left: UT Rx, bottom right: UT+ID Rx)

4.4 Navigation Solution Performance Analysis

This section reviews the navigation performance of the VB, VB+ID, UT and UT+ID receivers. Specifically, given the tracking results presented above, it is interesting to look at the number of observations used by the navigation solution with and without the new observation weighting method. It is important to keep in mind that the C/N_0-only observation weighting approach does not reject the observations, and, moreover, it may assign the weights to Doppler and pseudorange measurements poorly in the presence of interference as was already demonstrated in Figure 4.4 and Figure 4.5. However, innovation sequence testing is the way to reject the erroneous observations in the VB and UT receivers, which utilize the C/N_0 based weighting. Blunder detection in Kalman filtering is accomplished by testing the innovation sequences (in contrast to least-squares where blunder detection is performed using the measurement residuals) as shown for instance by Petovello (2003), Teunissen & Salzmann (1989). Note that the blunder detection algorithm is implemented in all four tested receivers; hence, the VB and UT receivers compared to VB+ID and UT+ID receivers should demonstrate different observation rejection performance in the presence of CW jamming, because the latter two are aided by the novel observation weighting technique, which can additionally reject corrupted observations. Finally, analysis of the amount of used observations is followed by the assessment of the position and velocity errors, which were obtained from all four modifications of GSNRx™.

It was shown in Section 4.3 that the newly developed measurement weighting scheme allocated larger weights to observations from those PRNs, which were largely affected by CW interference. However, since the novel technique also uses information obtained from the ID, it is of interest to see if any of the observations were completely rejected before being used by the VB+ID and UT+ID receivers to compute the navigation solution.

To this end, Figure 4.6 shows the total amount of available Doppler and pseudorange observations (blue line) and the number observations accepted (green circles) or rejected (red crosses) before being used by the VB and VB+ID receivers for the navigation solution computation. Almost no observations were rejected in the VB receiver (two observations were rejected by the blunder detection algorithm in the navigation filter), while there were multiple observations rejected by the novel observation weighting algorithm employed in the VB+ID receiver. Note that the UT and UT+ID receivers demonstrated very similar observation filtering results (see Appendix A:) to those obtained from the VB and VB+ID receivers, respectively.

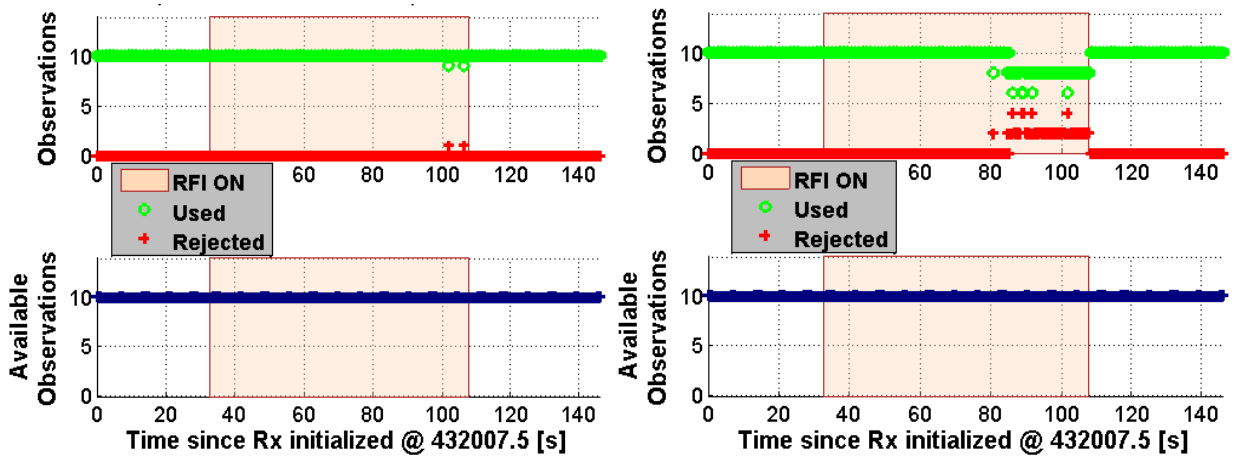

Figure 4.6: Observation Status for all 5 PRNs (left: VB Rx, right: VB+ID Rx)

Figure 4.7 helps to understand the reasons why Doppler and pseudorange observations were rejected in the VB+ID receiver. "ID+" in the legend in Figure 4.7 means that not only ID flags were taken into account, but also FLI and C/N_0 values were assessed to make a joint decision to reject the observation. Specifically, during the period from $t = 80$ s to $t = 115$ s, when the CW signal power was the strongest (J/S varied between 20 and 35 dB), the novel observation weighting method, which utilized information from the ID as well as the FLI and C/N_0 metrics, rejected multiple observations. These rejected measurements are from PRN 3 and PRN 19 (as expected from the analysis of tracking results in Section 4.3). Figure 4.7 also shows that no observations were rejected due to low C/N_0 or low lock time listed in Table 4.2.

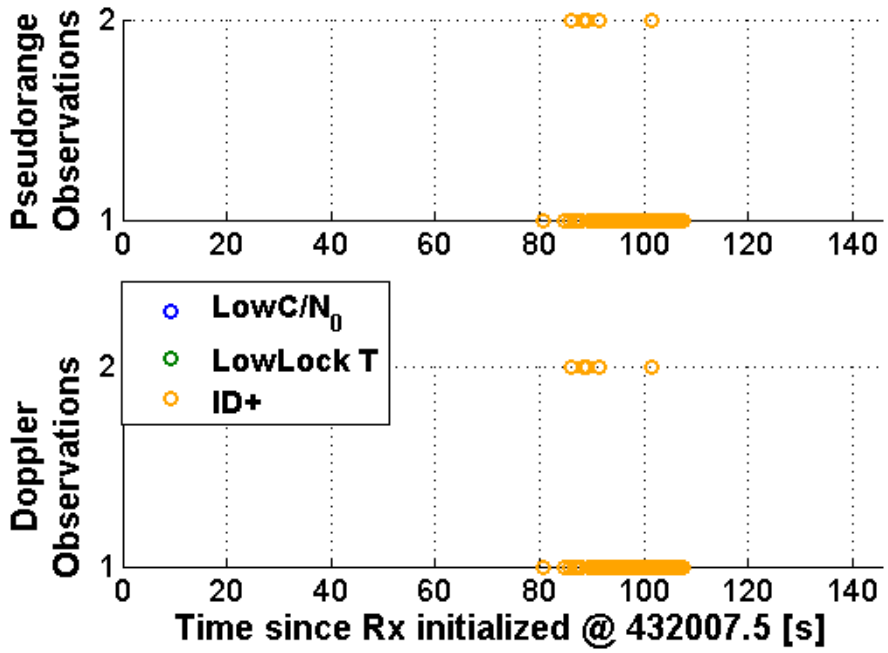

Figure 4.7: Status of Rejected Observations in the VB+ID Receiver

The interpretation of the rejected observations in the UT+ID receiver was the same as in the VB+ID receiver (basically, the ID rejected the same amount of observations in both receivers).

Having evaluated the tracking performance results, it is reasonable to assess the navigation domain results. Despite the fact that a vehicular motion in the horizontal plane was simulated in this test, the horizontal and vertical position and velocity performance of all four modifications of the GPS receiver are discussed. Figure 4.8 and Figure 4.9 show the time evolution of the horizontal position and velocity errors, respectively, which were generated by the VB, VB+ID, UT and UT+ID receivers. Analysis of the vertical position and velocity performance is presented in Appendix A:. Overall, all four receivers showed comparable height estimation in interference,

however, the VB receiver suffered from vertical velocity errors which reached 0.5 m/s when J/S was equal to 35 dB, while the VB+ID, UT and UT+ID receivers did not produce any significant vertical velocity errors.

As Figure 4.8 shows, the horizontal position errors, from all receivers considered, were very similar when the CW signal was turned on. However, during the last several seconds of the interference injection (when J/S varied between 30 and 35 dB), the VB+ID receiver slightly outperformed the VB receiver, because it did not use the observations from corrupted PRN 3 and 19. Several Doppler and pseudorange observations affected by the jammer (see Figure 4.6) were also not used by the UT+ID receiver that generated slightly smaller horizontal position errors than the UT receiver. Also, Figure 4.8 clearly illustrates that the VB+ID and UT+ID receivers produced larger position uncertainties than VB and UT, respectively, during the period when the CW signal reached its strongest power. This increase in position uncertainty can warn the user that the navigation solution is not entirely reliable.

Figure 4.8 shows a slow convergence of the navigation filter, which can be explained as follows. Firstly, as it was shown in Section 4.1, satellite availability in this scenario was poor, i.e. only five SVs were deliberately chosen for this test (this number of satellites can provide five Doppler and five pseudorange observations). It was particularly interesting to study whether the navigation performance of all four tested receivers would drastically degrade due to limited amount of observations in the presence of

jamming. Furthermore, the navigation filter was not necessarily tuned optimally and this, in turn, could lead to unsmoothed transition between the scalar and vector operational modes of all receivers (this explains the slip in the horizontal position errors at $t \approx 10\,\text{s}$ in Figure 4.8). One may observe in Figure 4.8 that the horizontal position uncertainty was slowly converging until $t \approx 60\,\text{s}$ and relatively large position errors at the beginning of the processing were in agreement with one-sigma values. In Figure 4.8 the position uncertainty during the initial 10 s was greater than 15 m, and it is plotted as a constant.

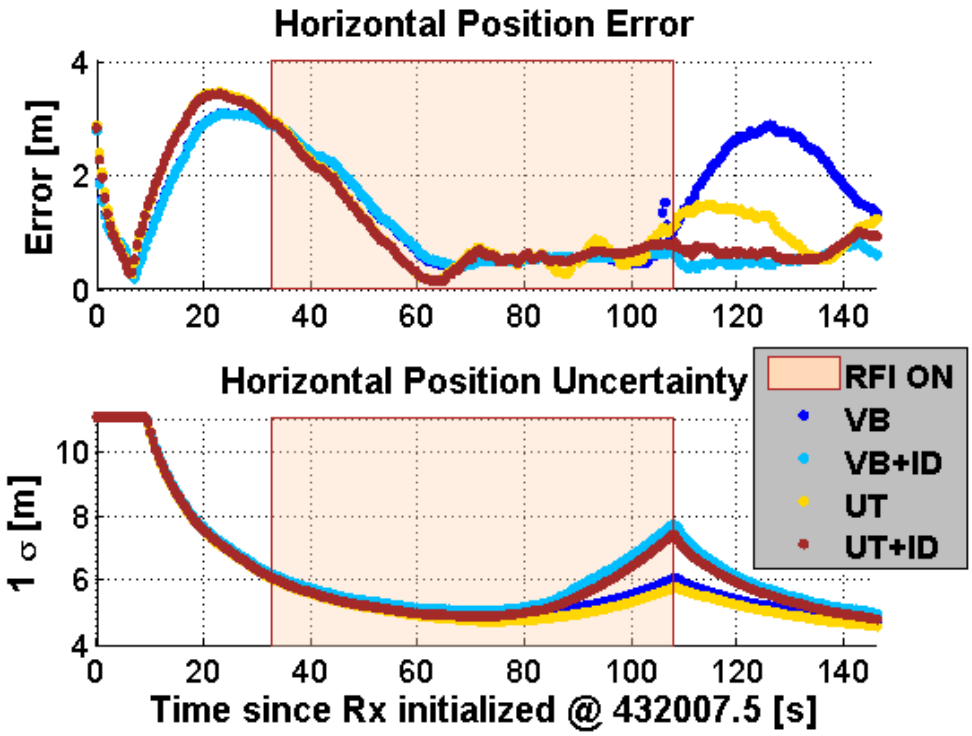

Figure 4.8: Horizontal Position Errors and Horizontal Position Uncertainty vs. Time

From Figure 4.8 it is clear that after the CW source was de-activated, the VB and UT receivers generated greater horizontal position errors than the receivers aided by the

ID. This is owing to the fact that corrupted pseudorange measurements from PRN 3 and PRN 19 (refer to Figure 4.4) introduced a bias into the navigation solution, which could not be detected in VB and UT mode. However, there was no such bias observed in case of the VB+ID and UT+ID, because these two receivers did not use the measurements affected by jamming, and only started using all available measurements when the CW signal was removed.

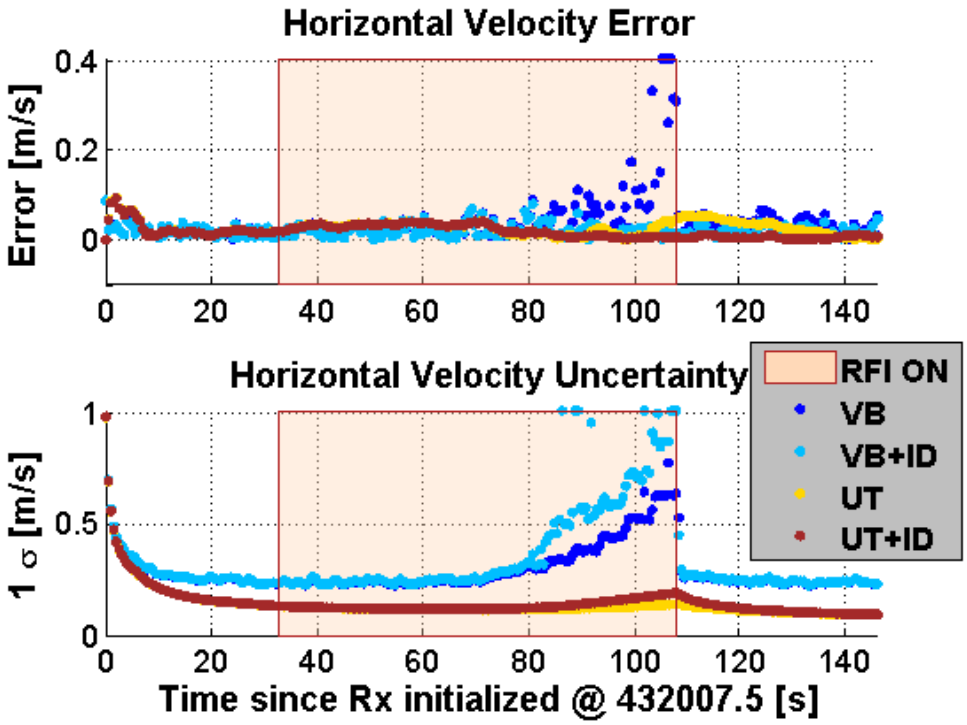

Figure 4.9: Horizontal Velocity Errors and Horizontal Velocity Uncertainties vs. Time

With regard to horizontal velocity estimation during jamming, Figure 4.9 shows that the VB receiver showed the worst performance compared to all other receivers (large horizontal velocity errors were observed between $t \approx 90$ s and $t \approx 110$ s). Even though

all receivers experienced erroneous Doppler frequency estimation of PRN 3 (refer to Figure 4.5), the VB+ID and UT+ID receivers rejected corrupted measurements and this, in turn, lead to smaller overall horizontal velocity errors during interference. One may observe that the UT receiver generated slightly biased velocity estimates when the J/S ratio ranged between 30 and 35 dB. Similar to Figure 4.8, velocity estimation uncertainties of the VB+ID and UT+ID receivers were slightly larger than those values obtained from the VB and UT receivers during the presence of the CW signal. Interestingly, the VB+ID receiver generated much smaller horizontal velocity errors compared to the VB receiver, while the velocity uncertainties of the former receiver were larger. This is owing to the fact that the new observation weighting scheme increased variances of the Doppler measurements (see Equation (3.4)). In other words, increased uncertainty of the velocity (position) estimates means that the VB+ID solution is more reliable compared to the solution obtained from the VB receiver, because the later receiver generated horizontal velocity errors larger than 1 m/s (error values at $t = 110$ s in Figure 4.9 are constrained to 0.4 m/s for convenience), while the one-sigma velocity uncertainty was below 0.6 m/s.

Figure 4.10 and Figure 4.11 summarize the horizontal position and velocity performance of all four versions of GSNRx™ during the simulated test. Figure 4.10 shows the horizontal position and velocity RMS errors during interference, while Figure 4.11 depicts the same performance parameters after the CW signal was switched off.

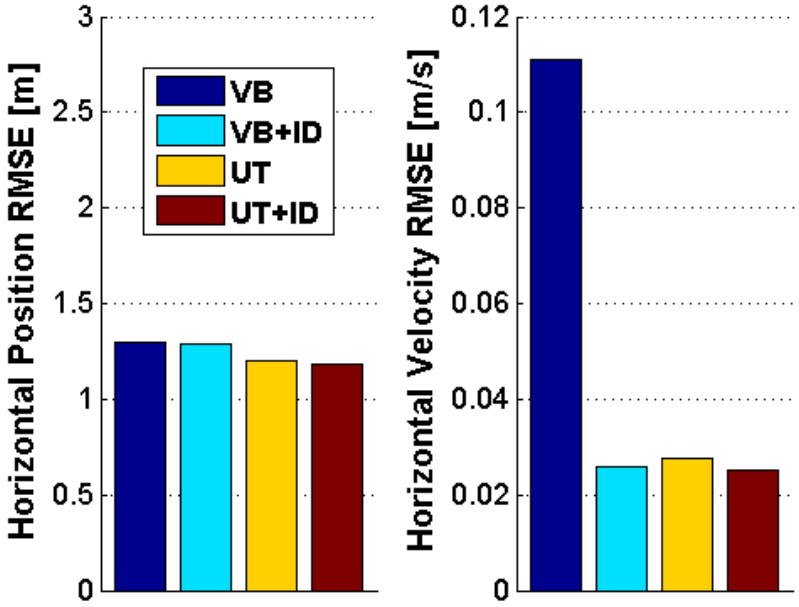

Figure 4.10: Horizontal Position and Velocity RMS Errors in the Presence of CW

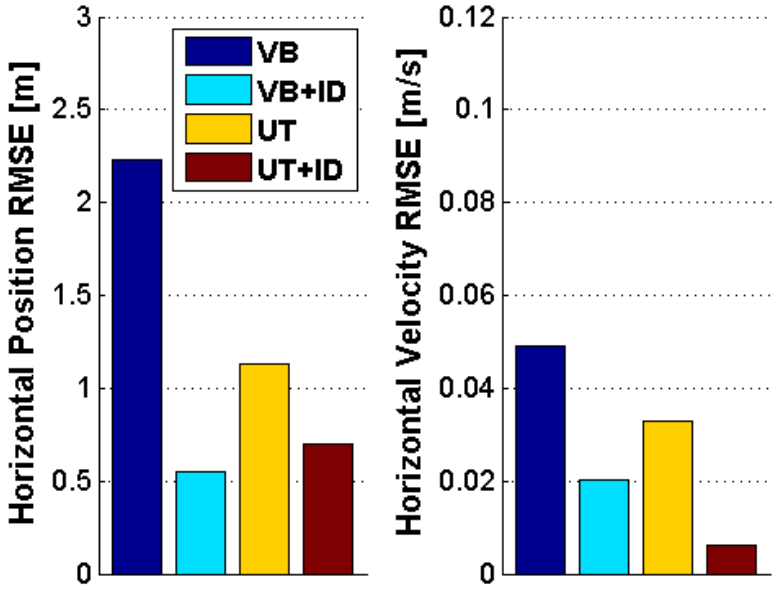

Figure 4.11: Post-Interference Horizontal Position and Velocity RMSE

Once again, while all four receivers showed similar navigation performance during the interference impact, the VB+ID receiver significantly outperformed the VB receiver in terms of the horizontal velocity estimation (compare dark and light blue bars on the right

plot in Figure 4.10). This is due to the fact that the VB receiver used erroneous Doppler measurements from PRN 3 (see Figure 4.5), while the VB+ID receiver rejected corrupted observations from this satellite (see Figure 4.6). Importantly, the VB+ID and UT+ID receivers demonstrated better overall position and velocity estimation than their counterparts after the CW signal was removed. Interestingly, the UT receiver shows better performance than the VB receiver, but this was expected since the IMU data aiding enhances the interference combating abilities of the GPS receiver; this fact was previously reported in the opened literature (see Chapter 1). However, perfect IMU data was used in this test. But in real scenarios the IMU suffers from deterministic and stochastic errors. Thus, testing based on real data is required to further verify the advantage of UT receivers over the VB receivers.

4.5 Summary

This chapter described the tracking and navigation domain results obtained from simulated data processing utilizing GSNRx™. Specifically, the VB, VB+ID, UT and UT+ID versions of the receiver were tested on data with injected CW interference, which were obtained from the Spirent GNSS simulator.

It was shown that the novel GPS observation weighting scheme provides more reliable performance compared to the C/N_0-only based method in the presence of a CW signal with varying power. Particularly, it was verified that the new observation weighting approach is capable of down weighting and rejecting Doppler and pseudorange

observations, which were obtained from PRNs impacted by the jammer. Also, it was shown that the novel observation technique sets larger position and velocity uncertainties during the presence of strong CW jamming.

Even though the overall tracking and navigation performance of the VB, VB+ID, UT and UT+ID receivers was comparable, the VB+ID slightly outperformed the VB receiver, while the UT+ID also showed better performance than the UT receiver. Furthermore, the VB+ID receiver showed better velocity estimation results in comparison with the VB receiver during the presence of CW interference. Importantly, both VB+ID and UT+ID receivers were capable of generating smaller horizontal position and velocity errors than the VB and UT receivers, respectively, in the post-interference period.

Finally, the VB+ID and UT+ID receivers provide more pessimistic values of the estimated position and velocity accuracies as compared to the VB and UT receivers, respectively.

Simulated data allowed to verify the methods which were developed in this work: namely, the implemented ID and new observation weighting scheme, which can be successfully used within a GPS receiver to combat CW jamming.

The results of real data processing are presented in Chapter 5.

Chapter Five: Performance Assessment of Vector-based and Ultra-Tight Receivers aided by Interference Detector Using Real Vehicular Data

5.1 Overview

Chapter 4 considered the tracking and navigation performance of the VB, VB+ID, UT and UT+ID receivers using simulated data. It was found that the vector-based and ultra-tight receivers aided by the multi-correlator ID and novel observation weighting scheme offer better overall interference resistance than the vector-based and ultra-tight receivers only.

This chapter presents a thorough analysis of the tracking and navigation capabilities of the VB, VB+ID, UT and UT+ID receivers employing real data collected on a vehicle in an open-sky scenario with and without interference being injected into the "clean" data samples. Similar to the results presented in Chapter 4, the Doppler and pseudorange tracking errors are assessed, and the tracking sensitivity of four receivers is examined utilizing the effective C/N_0, FLI and PLI metrics. This is followed by the analysis of the horizontal and vertical position and velocity errors. Also, the estimated accuracies of the navigation solution obtained from all four receivers are discussed.

5.2 Experiment Details

This section presents the details of the field test performed to collect the real data.

5.2.1 Equipment

The data collection was conducted in an open sky scenario on October 16th in 2014 in Calgary. The test vehicle was moving towards the West on 24th Avenue NW in Calgary.

The following hardware was used to collect the data:

- NovAtel SPAN-LCI served as a reference;
- NovAtel Pinwheel GPS-702-GG antenna;
- GTEC RFFE Fraunhofer Flexiband IIS front-end was used to collect the complex samples at $F_S = 81.00$ MS/s. The I and Q samples were later down-sampled to $F_S = 10.125$ MS/s using a software developed in the PLAN Group;
- Panasonic Toughbook CF 53 equipped with a Solid-State Drive (SSD) was connected to the GTEC RFFE front-end via the Universal Serial Bus (USB) 3.0 interface. The laptop was used to control the front-end and store the data.

Figure 5.1 demonstrates how the IMU and antenna were installed on the test vehicle. Specifically, the NovAtel LCI IMU and Pinwheel antenna were rigidly mounted to the vehicle's roof.

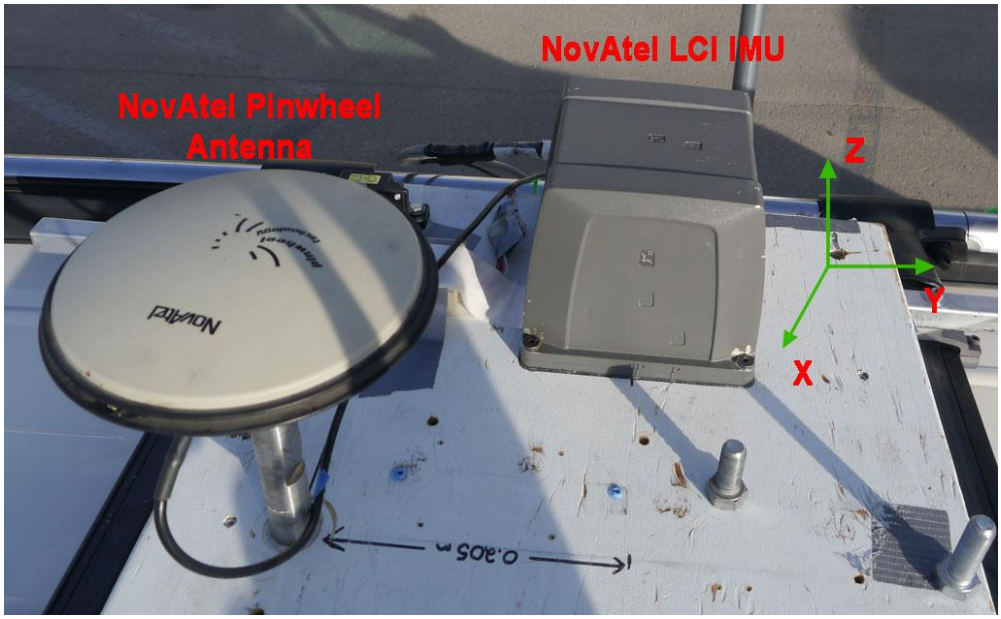

Figure 5.1: NovAtel Pinwheel Antenna and NovAtel LCI IMU Installation

The data logged by the tactical grade NovAtel LCI IMU was utilized in GSNRx™ to perform the ultra-tight integration with GPS. In other words, the data from tactical grade IMU was used in the UT and UT+ID receivers in post-processing. As shown by Li et al (2010), quality of the IMU plays a minor role in the performance of an ultra-tight receiver, and this fact justifies the choice of the tactical-grade IMU used in this work. The IMU modelling parameters were set equal to those values presented in Table 4.4.

5.2.2 Scenario

Figure 5.2 shows the satellite sky plot of the field test, and, in addition to that, Figure 5.3 depicts the Doppler frequencies of all SVs chosen for processing. There were six GPS satellites available in total, however, PRN 26 was located at a low elevation

(approximately 11 degrees); that was below the chosen elevation mask (15 degrees). This is why PRN 26 was eliminated from processing.

In this test, Dilution of Precision (DOP) values, which quantify the SV geometry, were the following: horizontal (HDOP) – 1.8 and vertical (VDOP) – 2.0.

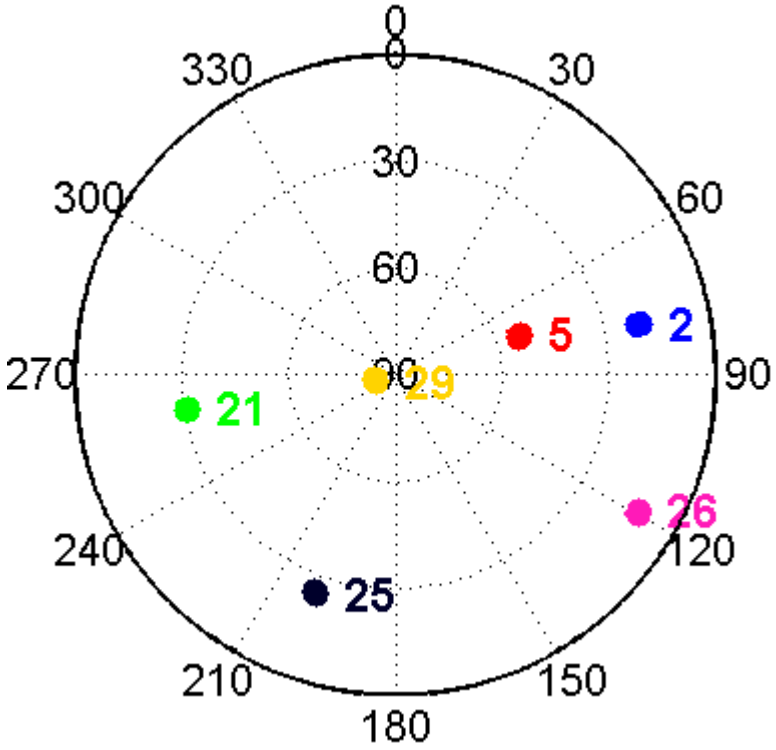

Figure 5.2: Satellite Sky Plot of the Real Data Set

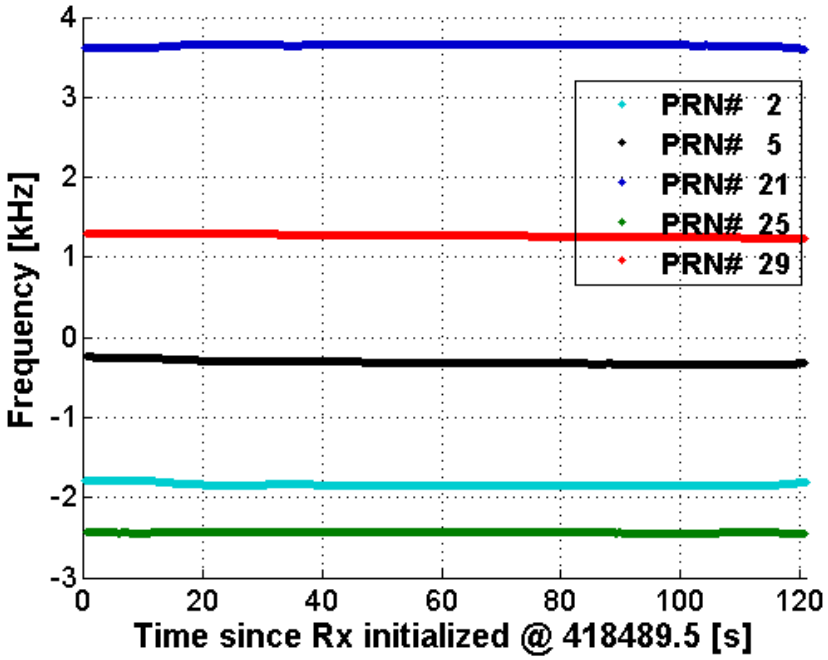

Figure 5.3: Doppler Frequencies of all 5 SVs Chosen for Processing

5.2.3 Interference Generation

Interference generation was the biggest challenge in this test. Since transmission of the RFI signals outdoor is prohibited by law, it was decided to collect “clean” data samples and add the CW jamming signal to I and Q samples in post-mission.

This approach assumes that the effect of the AGC unit of the front-end is neglected. However, the assumption that the AGC is switched off was already made in Chapter 4. Given this, the remaining task was computation of the noise variance of the sampled signal and generation of the CW signal with appropriate power. As such, Jammer-to-Noise (J/N) ratio was considered instead of the J/S ratio in this test. This is due to the fact that the latter can be easily set in the Spirent Simulator during simulated data collection, while it is impossible to know the real signal power due to the noise figure of

the setup in a real test. The J/N ratio is also a commonly used metric (for instance, it was used by Wildemeersch & Fortuny-Guasch 2008). Therefore, CW interference with certain J/N ratios was additively mixed with the "clean" samples between $t = 40 - 70$ s ($t = 0$ s is the time period when the receiver computed the first navigation solution). In other words, the clean data was processed by GSNRx™ to find the exact time when the receiver initialized (computed first navigation solution), and after this time instance was identified, 40 s were skipped prior to interference injection. The CW signal power was chosen in such way that established the J/N ratios between 10 dB and 25 dB. Particularly, the J/N ratio was changed every 5 s.

It was decided to generate f_{CW} which would target the strongest spectrum line of PRN 29 located at 176 kHz; f_D of this PRN was approximately 1280 Hz (see Figure 5.3 for detail). However, given the Doppler frequencies of other available PRNs, it was expected that some of them would also become drastically affected by generated CW interference. This will be investigated in Section 5.3.

To conclude this section, Table 5.1 summarizes the CW signal parameters.

Table 5.1: CW Interference Parameters for Real Data Test

Time, s	40 – 45	45 – 50	50 – 55	55 – 60	60 – 65	65 – 70
J/N, dB	10	15	20	20	20	25
Frequency, kHz	177.28					

5.2.4 Data Processing Parameters

Almost all parameters used for data processing, namely tracking and navigation filter parameters, ID settings, and IMU modelling parameters, were chosen as those presented in Chapter 4. Such choice of the values allowed for a fair interpretation of all results obtained in this thesis. However, several parameters were changed compared to Chapter 4, as given in Table 5.2.

Table 5.2: Modified Processing Parameters Used in Real Data Test Compared to Simulated Data Test

Processing Parameters	Unit	Value
GPS Pseudorange Standard Deviation	m	10.00
GPS Doppler Standard Deviation	Hz	1.00
C/N_0 Mask	dB-Hz	25.00
Oscillator H-Parameter h_0	$Hz/\sqrt{Hz}$	2.0E-22
Oscillator H-Parameter h_{-1}	$Hz^2/\sqrt{Hz}$	2.0E-21
Oscillator H-Parameters h_{-2}	$Hz^3/\sqrt{Hz}$	6.3E-20

First, since the GTEC RFFE front-end IIS utilizes a Temperature-Compensated Crystal Oscillator (TCXO), it was required to compute the corresponding spectral density values for the clock errors. This was done using the approach discussed by Chang et al (2004). Specifically, knowing the oscillator phase noise values (see Appendix B: for detail) it was possible to compute the oscillator spectral densities, which can be found is Table 5.2. Moreover, due to stronger interference levels than those in the simulated test, and

because the C/N_0 can drop a few dBs due to signal fading, it was decided to decrease the C/N_0 mask by 5 dB compared to the 30 dB-Hz value used Chapter 4. Finally, the standard deviations of pseudorange and Doppler observations were set in a pessimistic way (basically, standard deviation values were doubled), because real GPS measurements are noisier as opposed to simulated values due to signal degradation caused by the atmospheric irregularities, multipath effects, quality of the oscillator used in the GTEC RFFE front-end, momentary signal blockage or fading, etc.

5.3 Tracking Domain Results

To examine the tracking sensitivity of the VB, VB+ID, UT and UT+ID receivers, the effective C/N_0, FLI and PLI values are evaluated. Figure 5.4 and Figure 5.5 show the C/N_0, FLI and PLI as a function of time when using all four receivers in an outdoor kinematic scenario in which CW interference occurred between $t = 40$ s and $t = 70$ s.

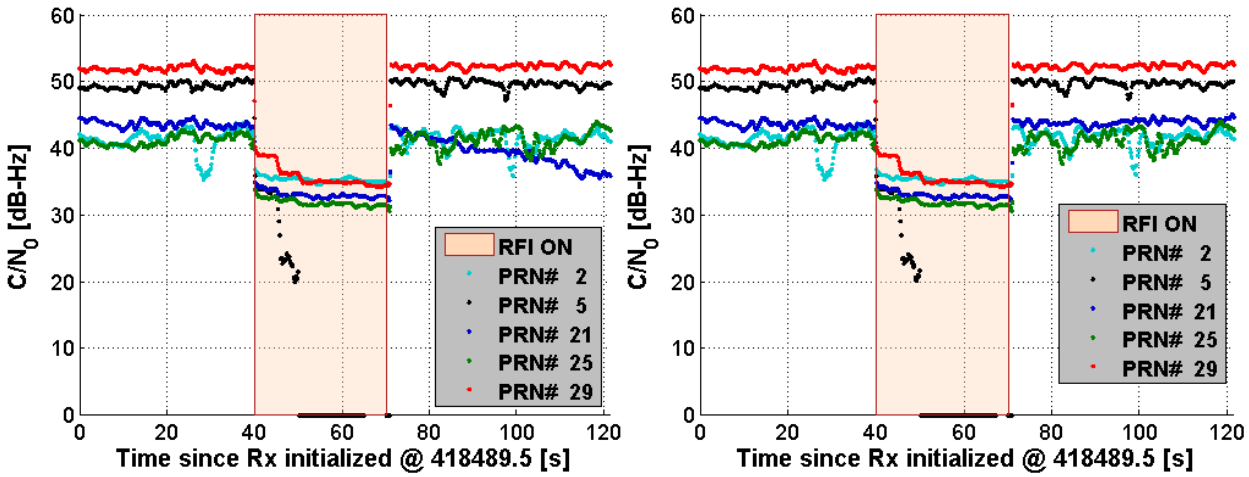

Figure 5.4: Estimated C/N_0 of all PRNs (left: VB Rx, right: VB+ID Rx)

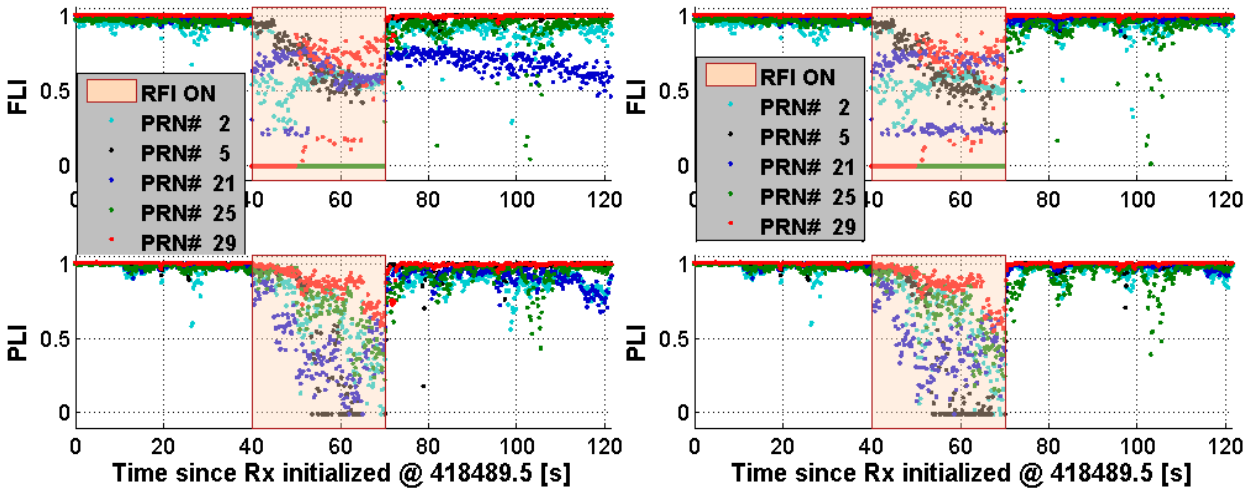

Figure 5.5: Estimated FLI and PLI of all PRNs (left: VB Rx, right: VB+ID Rx)

What is immediately apparent from Figure 5.4 is that the C/N_0 metric of PRN 29 reacted in a stair-like manner to the CW interference signal that had varying signal power, while the C/N_0 values of PRN 5 could not be estimated by both receivers from 40 to 70 s. At the same time, the C/N_0 of PRN 2, 21 and 25 reacted to the CW jamming in a step function manner. Also, Figure 5.4 shows that both VB and VB+ID receivers produced essentially the same C/N_0 values for all PRNs during interference, but in the post-interference period the C/N_0 estimates of PRN 21 of the VB mode started decreasing (the reason for this will be discussed later on). Having in mind the C/N_0 results obtained from the simulated data in Chapter 4, similar tracking performance of the VB and VB+ID receivers was expected because the same signal tracking algorithm was employed in both receivers. The reason why the carrier-to-noise values of PRN 21 in the VB receiver were dropping between $t = 70$ s and $t = 120$ s can be understood by analyzing the FLI values from Figure 5.5. One may notice that the FLI of PRN 21 was slowly decreasing

with time after interference. Simultaneous decrease of the C/N_0 and FLI means that the tracking loop of the VB receiver was not able to maintain a proper lock on this PRN. In contrast, the VB+ID receiver did not experience such decrease of the C/N_0 and FLI.

Interestingly, the C/N_0 values of PRN 29 and PRN 2 were slightly stronger than those values obtained from other PRNs. Recall that the effect of the CW signal on the SV signal depends on the difference between the Doppler and jamming frequencies (as discussed in Chapter 3). This is why the C/N_0 values for PRN 29 decreased by almost 20 dB, while PRN 2, 21 and 25 experienced only a 10 dB drop. Importantly, both receivers failed to produce C/N_0 estimates for PRN 5 during $t = 50$ s and $t = 70$ s. Analysis of the FLI and PLI values of PRN 5 in Figure 5.5 allows one to conclude that both VB and VB+ID receivers lost lock on PRN 5.

Before assessing the FLI and PLI metrics, it should be mentioned that when the FLI or PLI values were less than zero, they were plotted as zero for convenience. With regard to the FLI and PLI performance, one can observe in Figure 5.5 that the VB+ID receiver produced slightly different values for PRN 21 as opposed to the VB receiver (especially in the post-interference period). Also, during interference the VB receiver never set the FLI values of PRN 21 below 0.5, while those values from the VB+ID receiver dropped to 0.2. Recall the results obtained in Chapter 4 where the CW interference affected frequency tracking in a different way for various PRNs. This is also demonstrated in Figure 5.5 which shows that the FLI values of PRN 29, targeted by the CW signal, were

equal to zero between $t = 40$ s and $t = 50$ s, while the FLI values of PRN 25 were set to zero between $t = 50$ s and $t = 70$ s, meaning that the frequency lock was very poor (negative FLI values plotted as zeros effectively mean poor frequency lock).

Overall, the analysis of the C/N_0, FLI and PLI values allows one to say that the interference did not only affect PRN 29 (which was targeted by the CW signal), but drastically affected signals from other satellites such as PRN 5 and PRN 21. To explain these findings, Figure 5.6 shows the Doppler frequency of all PRNs plus jamming frequency (f_{CW}) modulo 1 kHz. It is apparent that when the Doppler frequency of PRN 5 (or PRN 21) and the jamming frequency is added, modulo 1 kHz of the resulting value is very close to 1 kHz. Recall the results from Chapter 3, where it was shown that if the linear combination of f_{CW} and the Doppler frequency is an integer multiple of 1 kHz, then the effect of the CW interference on the C/N_0 will be significant. This means that although PRN 29 was directly targeted by the CW signal in this particular test, PRN 5 and PRN 21 were also affected by interference due to the specific relation between the Doppler frequency of these satellites and f_{CW}.

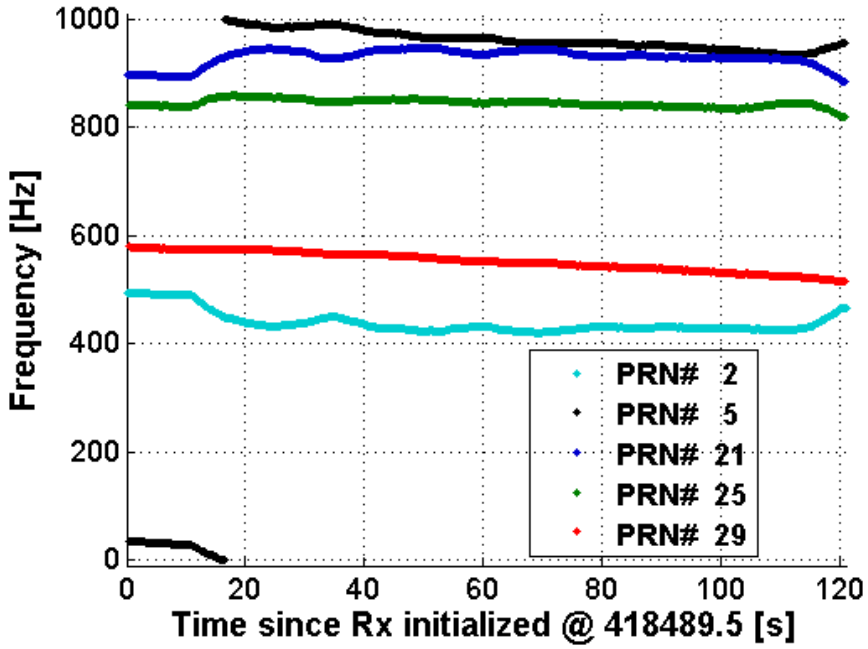

Figure 5.6: Doppler Frequency of all PRNs plus CW Frequency modulo 1 kHz vs. Time

Due to the fact that the same tracking strategy was utilized in all four receivers considered in this research, the C/N_0, FLI and PLI values generated by the UT and UT+ID receivers did not drastically differ from those values (see Figure 5.4 and Figure 5.5) obtained from the VB and VB+ID receivers, respectively. As such, these values for the UT and UT+ID receivers are omitted here and are instead provided in Appendix B:.

Having in mind the behavior of signal lock indicators discussed above, the next step is to further extend the analysis of the tracking performance of the four receivers and examine the pseudorange and Doppler tracking errors, which are shown in Figure 5.7 and Figure 5.8, respectively.

As can be seen from Figure 5.7, all four receivers experienced pseudorange error variations when the CW signal was injected. However, all receivers were almost insensitive to the J/N level of 10 dB between $t = 40$ s and $t = 45$ s). Figure 5.7 also shows that the VB receiver demonstrated the worst pseudorange estimation performance for PRN 21 among all tested receivers. Specifically, pseudorange errors of PRN 21 exceeded 6 m starting from $t = 55$ s until the end of the processing, while the VB+ID receiver managed to recover from the errors for this SV. Even though the VB+ID, UT, and UT+ID receivers also failed to produce correct pseudoranges for PRN 5 (the reason for this will be addressed later on), both UT modifications generated more accurate overall pseudorange measurements compared to the VB modifications during and after interference. Additionally, the VB receiver generated constantly growing pseudorange errors for PRN 2. Interestingly, the UT+ID receiver did not produce much pseudorange errors for PRN 2, 25 and 29 during $t = 50$ s and $t = 70$ s (recall from Table 5.1 that the J/N was varying from 20 dB to 25 dB during this time period).

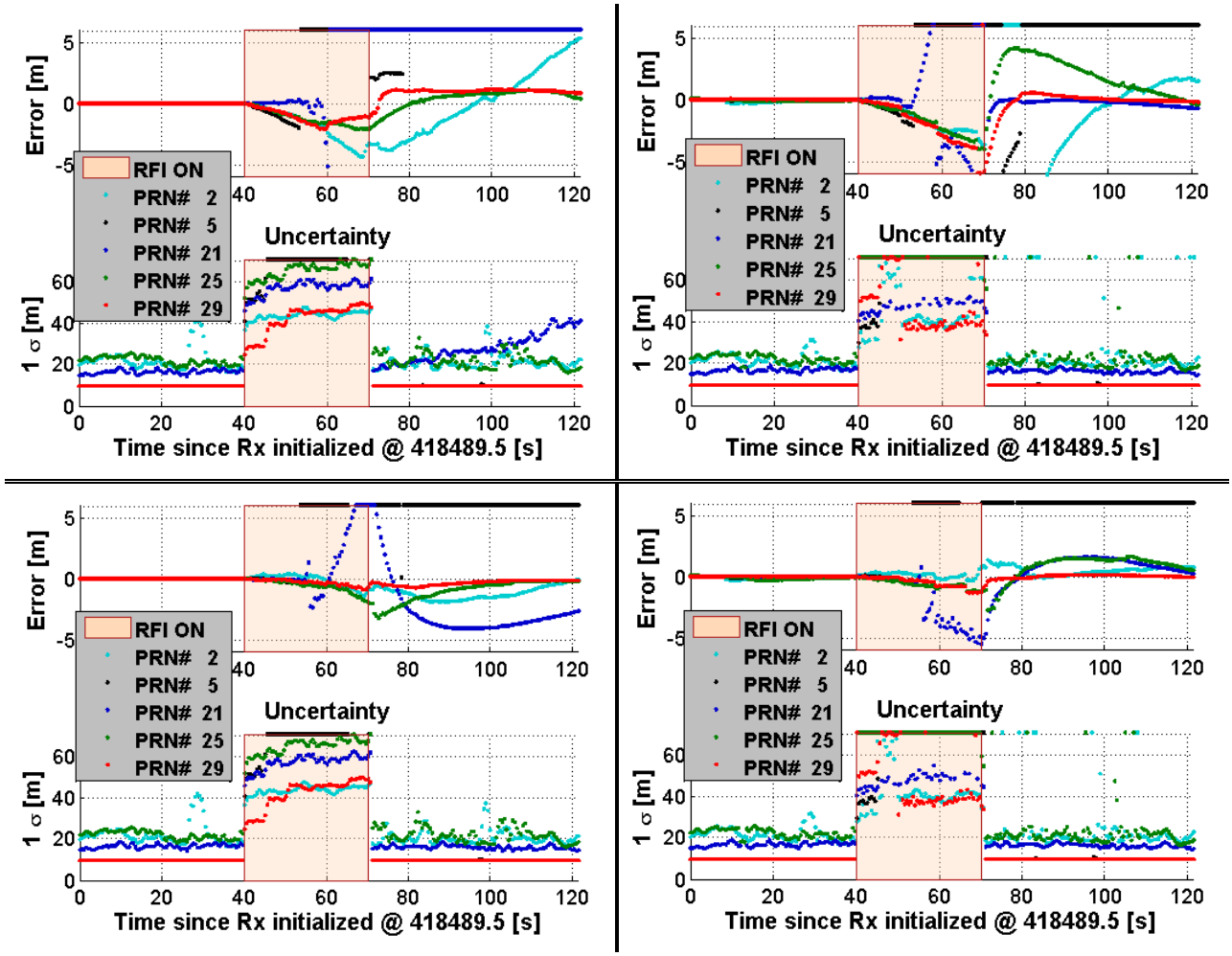

Figure 5.7: Pseudorange Errors and Pseudorange Observation Uncertainties (upper left: VB Rx, upper right: VB+ID Rx, bottom left: UT Rx, bottom right: UT+ID Rx)

Also, the UT receiver generated the erroneous pseudoranges for PRN 21 (a quick increase in the pseudorange errors is depicted in Figure 5.7), while its counterpart, the UT+ID receiver, resulted in much smaller errors for this PRN. Importantly, Figure 5.7 shows that the VB+ID, UT and UT+ID receivers produced slightly biased pseudoranges for almost all PRNs after the CW source was de-activated. This means that these

biases can potentially translate into the navigation position domain. The effect of such biases on the navigation solution will be addressed in Section 5.4.

Note that the pseudorange errors of PRN 21 in the VB receiver gradually increased and reached about -100 m at $t = 120$ s (the maximum error is constrained to 6 m in Figure 5.7 for convenience), while the error of PRN 5 reached a very large value of several hundreds of km. To explain the latter, recall that all four receivers lost lock on PRN 5 during the CW interference, and then they re-acquired the signal from this SV at $t = 70$ s. However, both bit and navigation synchronization were not yet established. The receivers attempted to perform bit and navigation synchronization for PRN 5, but as the analysis of the pseudorange innovation sequence showed, it was not successful. Particularly, the innovation sequence values for pseudoranges after $t = 80$ s were integer multiples of one millisecond, and this is an indicator of wrong bit synchronization. Subsequently, this lead to incorrect navigation synchronization; hence, the pseudorange of PRN 5 could not be correctly computed by any of the receivers.

Once again, although the PRN 29 was targeted by the jammer, PRN 5 and PRN 21 were affected even more because of the relation between their respective Doppler frequencies and the frequency of the CW signal. Also, since the C/N_0 values of PRN 5 and PRN 21 were lower than those of PRN 29 before jamming, it makes sense that the accuracy of Doppler and pseudorange measurements of PRN 5 and PRN 29 became poorer than those of PRN 29 under jamming.

With regard to the observation variances, both new observation weighing and C/N_0 methods provided increased one-sigma uncertainties during the presence of CW jamming. However, after the interference source was removed, the C/N_0 method assigned relatively small pseudorange variances to PRN 5 and PRN 21. At the same time, the new observation weighting technique that was applied in the VB+ID and UT+ID receivers set variances that complied with the pseudorange error values.

By looking at the Doppler tracking errors of PRN 21 shown in Figure 5.8, it is clear that the VB receiver performed worst amongst all receivers after CW injection. In fact, all four receivers produced Doppler errors for PRN 21 that were larger than 1 Hz between $t = 50$ s and $t = 70$ s (when the J/N ratio varied between 20 dB and 25 dB). Importantly, the VB, VB+ID, UT and UT+ID receivers generated erroneous Doppler frequency for all other PRNs during interference impact, but the errors did not exceed 1 Hz. As opposed to Figure 5.7, which shows that several pseudorange observations were biased immediately after the CW signal was switched off, Figure 5.8 shows that Doppler measurements were not biased beginning from $t = 70$ s. This, in turn, should improve velocity estimation.

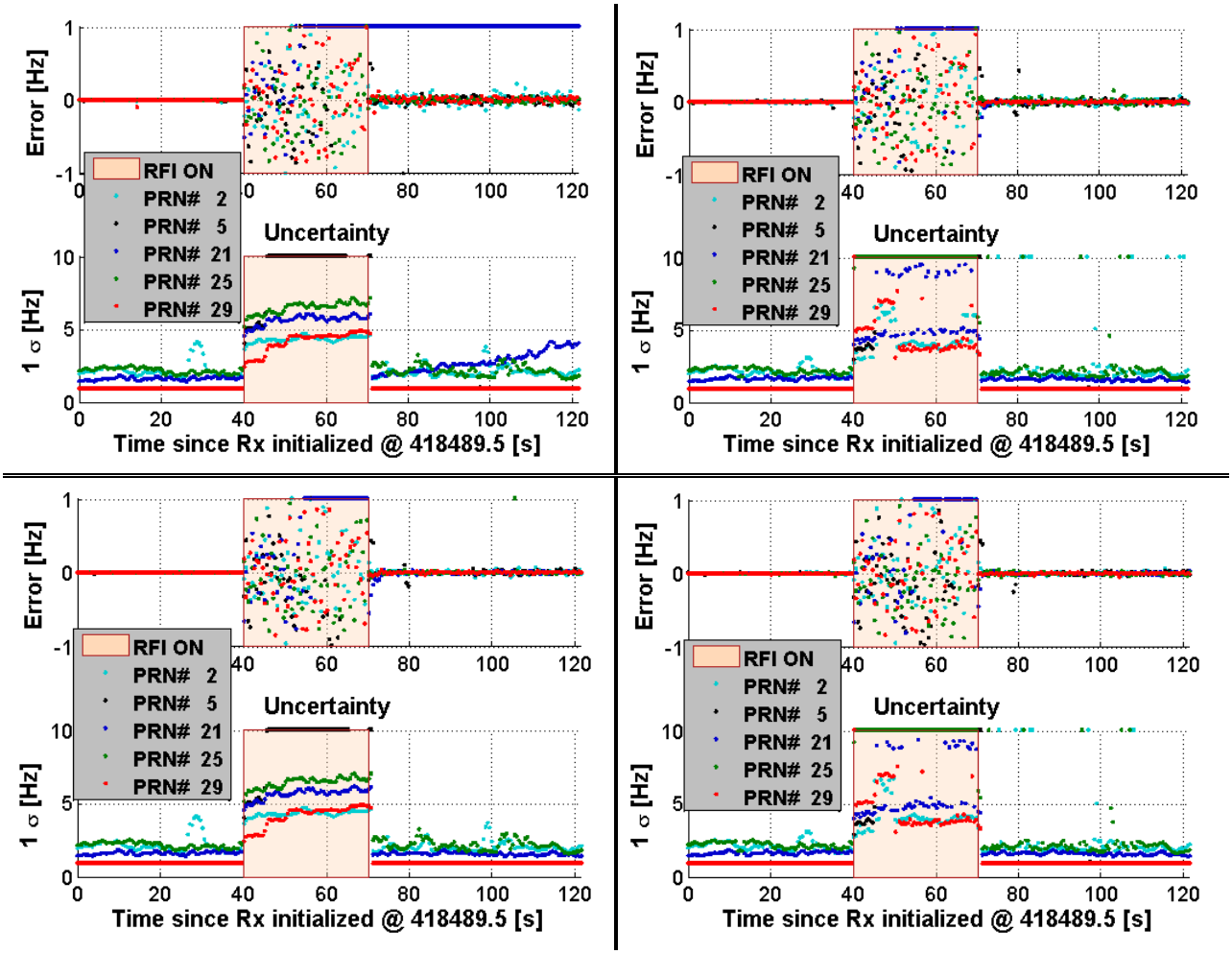

Figure 5.8: Doppler Errors and Doppler Observation Uncertainties (upper left: VB Rx, upper right: VB+ID Rx, bottom left: UT Rx, bottom right: UT+ID Rx)

Examining one-sigma uncertainties of Doppler estimates in Figure 5.8 one may observe that both C/N_0 and new observation techniques increased the observation variance for all PRNs in all four tested receivers during CW interference. Noticeably, the C/N_0 weighting method in the VB receiver set a relatively small variance for PRN 21 that suffered from large Doppler errors after the interference was removed. Recall that the same effect was observed earlier in the case of the pseudorange uncertainties of PRN

21 (see Figure 5.7). Several instances of increased Doppler uncertainty in the VB+ID and UT+ID receivers during $t = 70 - 120$ s occurred due to the FLI drops (see Figure 5.5), which are utilized in the new observation weighting approach (refer to Equation (3.4)).

From the tracking performance results presented so far, it is evident that the performance enhancement provided by the VB+ID and UT+ID receivers is indeed noticeable. This provides motivation for examining the navigation performance of all four receivers.

5.4 Navigation Solution Performance Analysis

Before assessing the position accuracies obtained from the VB, VB+ID, UT and UT+ID receivers, it is important to discuss the availability of Doppler and pseudorange observations. Figure 5.9 shows the observation availability in the VB and VB+ID receivers. It is clear that the VB modification rejected only two observations during CW injection, while its counterpart rejected many Doppler and pseudorange measurements. When J/N ratio was varying between 20 dB and 25 dB ($t = 50 - 70$ s), the VB+ID receiver rejected almost all available observations due to the ID flags.

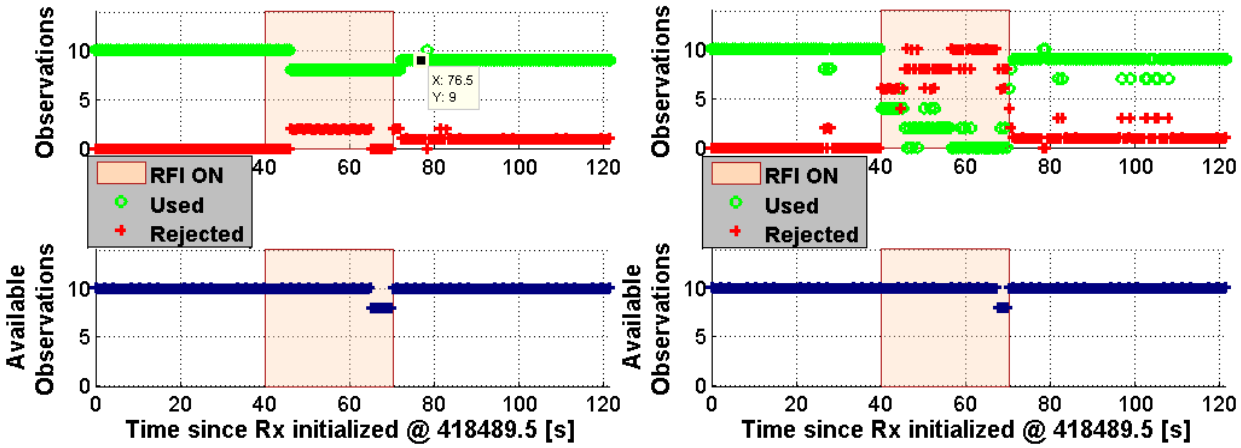

Figure 5.9: Observation Status for all 5 PRNs (left: VB Rx, right: VB+ID Rx)

Also, as it was previously discussed, all receivers failed to properly estimate the pseudoranges for PRN 5; this is why one observation was rejected in Figure 5.9 after $t = 70$ s.

To clarify the results presented in Figure 5.9, Figure 5.10 provides the full interpretation of the reason why measurements were rejected. One can easily observe that most of the Doppler and pseudorange measurements were rejected by the VB+ID due to ID flags. Furthermore, Figure 5.9 shows that one pseudorange was not used starting from $t = 70$ s. This happened because all tested receivers lost lock on PRN 5 during the CW impact, and the signal from this SV was just re-acquired at $t = 70$ s. However, the receivers did not immediately establish bit and navigation synchronization. This is why the pseudorange observations of PRN 5 were not valid for about 10 s (it is also not shown as rejected in Figure 5.10). Unfortunately, even after $t \approx 78$ s the VB and VB+ID receivers did not employ the pseudorange measurements from PRN 5 because the receivers failed to establish proper bit synchronization and the pseudoranges were

removed as blunders during the innovation sequence testing in the navigation filter until the end of the processing. In other words, although the re-acquisition of that particular PRN was proper, the bit synchronization was not correctly done. However, neither re-acquisition nor bit synchronization is within the scope of this thesis, hence, this issue is not considered here.

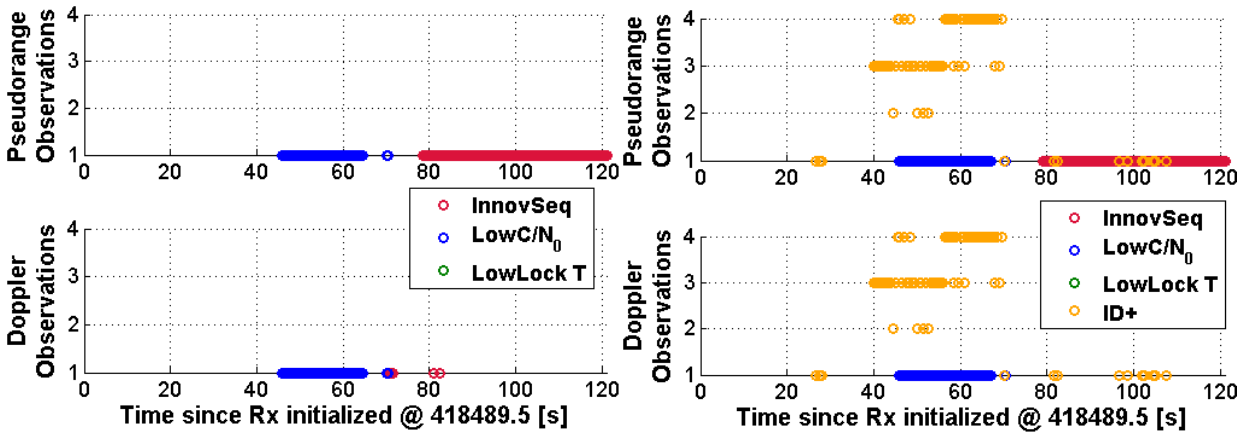

Figure 5.10: Status of Rejected Observations (left: VB Rx, right: VB+ID Rx)

The observation availability along with the interpretation of rejected measurements in the UT and UT+ID receivers was similar to that of the VB and VB+ID receivers, respectively. As such, the corresponding plots can be seen in Appendix B:. Generally, because the same observation weighting strategy was used in both UT+ID and VB+ID receivers, the amount of rejected measurements and their interpretation in the UT+ID mode is similar to that of the VB+ID receiver. The amount of rejected observations in the VB and UT receivers is also comparable.

Before analyzing the position and velocity errors itself, it is worth looking at the trajectories obtained from all four receivers considered in this work. Figure 5.11 shows the trajectories generated by the VB, VB+ID, UT and UT+ID receivers. Recall that the vehicle was moving West for about two minutes. Figure 5.11 allows one to conclude that the VB receiver showed the worst navigation performance among all tested receivers. In fact, the ending point of the VB trajectory was located at -243 m in the easting direction and -986 m in northing.

Also, Figure 5.11 shows that after interference injection, the UT and UT+ID receivers generated the trajectories that were closer to the reference as opposed to the VB+ID receiver that was quite “off” from the “true” solution, while the VB solution totally diverged.

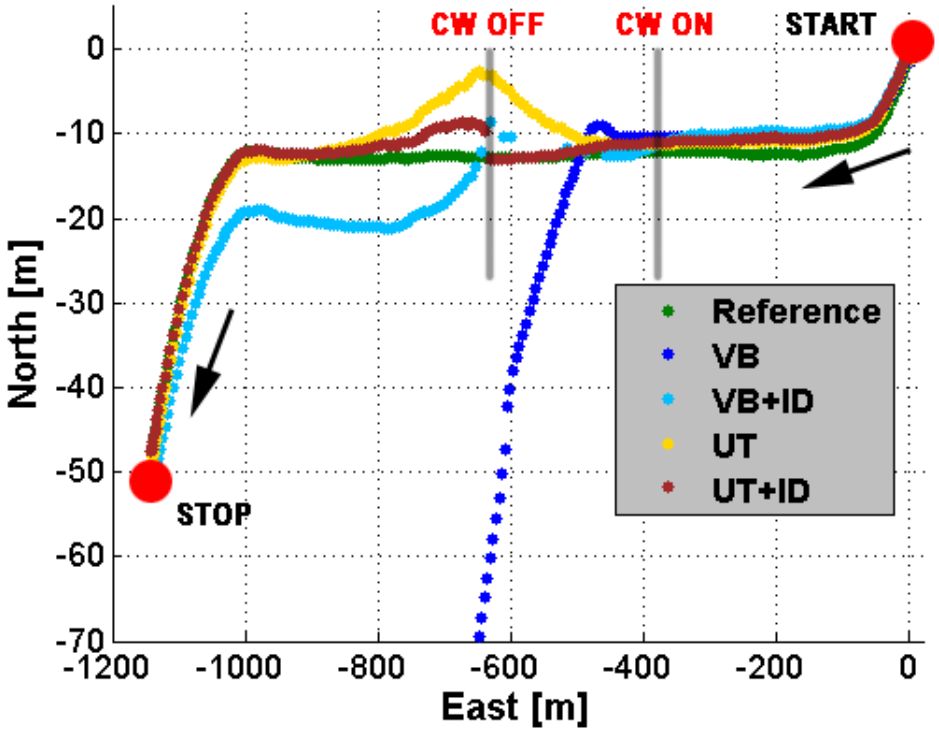

Figure 5.11: Trajectories Obtained from all Four Tested Receivers

The horizontal and vertical position and velocity performance of all four modifications of the GPS receiver are discussed below. Figure 5.12 shows the horizontal and vertical position errors, generated by the VB, VB+ID, UT and UT+ID receivers, as a function of time. In addition to this, Figure 5.13 depicts the corresponding horizontal and vertical velocity errors. In order to determine the position and velocity accuracies presented in this chapter, the navigation solutions are compared to the reference navigation solution that was obtained from the NovAtel SPAN system.

As Figure 5.12 shows, the horizontal errors generated by all four receivers did not exceed 5 m before the CW interference was injected, while the vertical errors were not greater than 10 m. Also, analysis of one-sigma position uncertainties allows one to

understand that it took about 20 s for the navigation filter of all receivers to settle. Interestingly, the VB, VB+ID, UT, and UT+ID receivers did not react to the J/N ratio which ranged from 10 dB to 20 dB during $t = 40 - 55$ s. However, all four tested receivers started suffering from position errors beginning at $t \approx 55$ s until the CW source was de-activated. Figure 5.12 shows that the VB+ID receiver significantly outperformed the VB receiver during interference. To explain the latter, recall the tracking results demonstrated earlier in Figure 5.7 and Figure 5.8. The VB modification generated large horizontal and vertical position errors, because it used erroneous pseudorange and Doppler measurements from the majority of available PRNs. At the same time, the VB+ID receiver rejected multiple observations (see Figure 5.9 and Figure 5.10) and this resulted in smaller overall position errors. In fact, the horizontal and vertical position errors produced by the VB receiver reached 242 m and -195 m, respectively (the maximum absolute errors are set to 20 m in Figure 5.12 for plotting convenience).

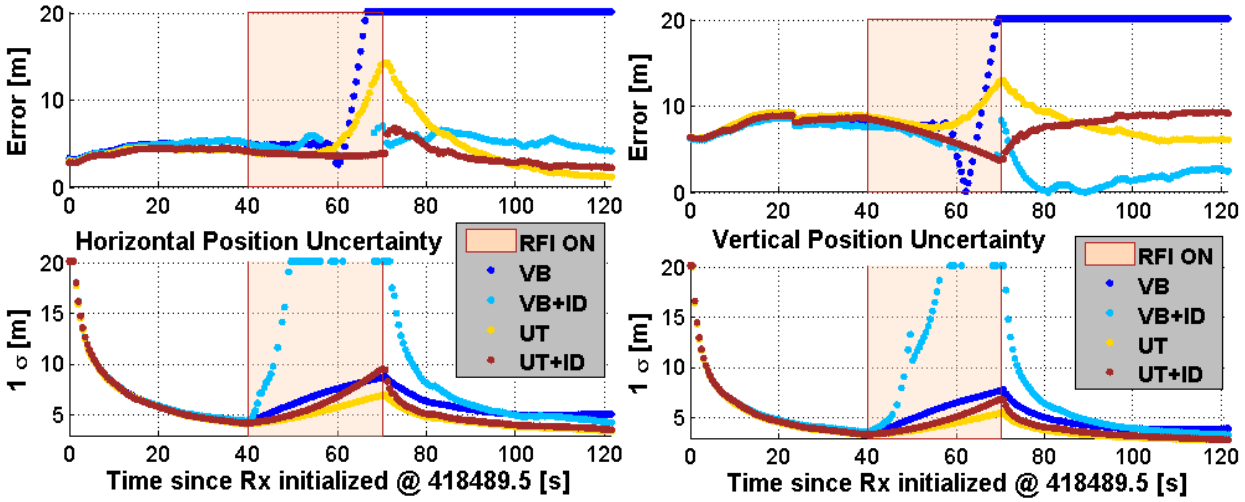

Figure 5.12: Horizontal (Left) and Absolute Vertical (Right) Position Errors and Corresponding Estimated Uncertainties for all Four Receivers

As expected from the comparison between the VB and VB+ID receivers, Figure 5.12 shows that the UT performed worse than the UT+ID receiver when the CW signal was present. This is also due to the fact that the latter receiver rejected multiple Doppler and pseudorange observations, while the former receiver did not. Interestingly, the VB+ID receiver managed to outperform the UT receiver during the first 10 s after CW interference. However, one should take into account that the VB+ID receiver rejected all available observations between $t \approx 60-70$ s (refer to Figure 5.9), and thus failed to produce a navigation solution. Specifically, all Doppler and pseudorange observations were rejected by the ID, hence the VB+ID receiver did not generate a navigation solution several times between 60 and 70 s. Therefore, although the VB+ID receiver provided smaller position and velocity errors under interference than the VB modification or even the UT receiver, the navigation solution availability was not permanent during strong jamming. Assessing the performance of all four receivers, it is

evident that the VB+ID, UT and UT+ID modifications managed to recover from large position errors after the CW source was removed. Nevertheless, this is not the case for the VB receiver, which generated notable position errors in the horizontal and vertical components (see the blue line in Figure 5.12).

To further explore the navigation performance of all four receivers under jamming, it is useful to assess the velocity errors shown in Figure 5.13. Similar to the case of the position errors presented above, all receiver configurations showed comparable velocity errors before the interference injection. From Figure 5.13 it is obvious that the VB receiver failed to provide acceptable velocity estimates after $t = 60$ s, while the VB+ID receiver produced relatively errorless velocities. However, even better velocity estimation performance was shown by the UT+ID receiver, which generated the smallest horizontal and vertical velocity errors among all tested receiver configurations. The UT receiver suffered from a horizontal velocity bias when interference was present; such a bias was also observed in horizontal position and height in the UT receiver.

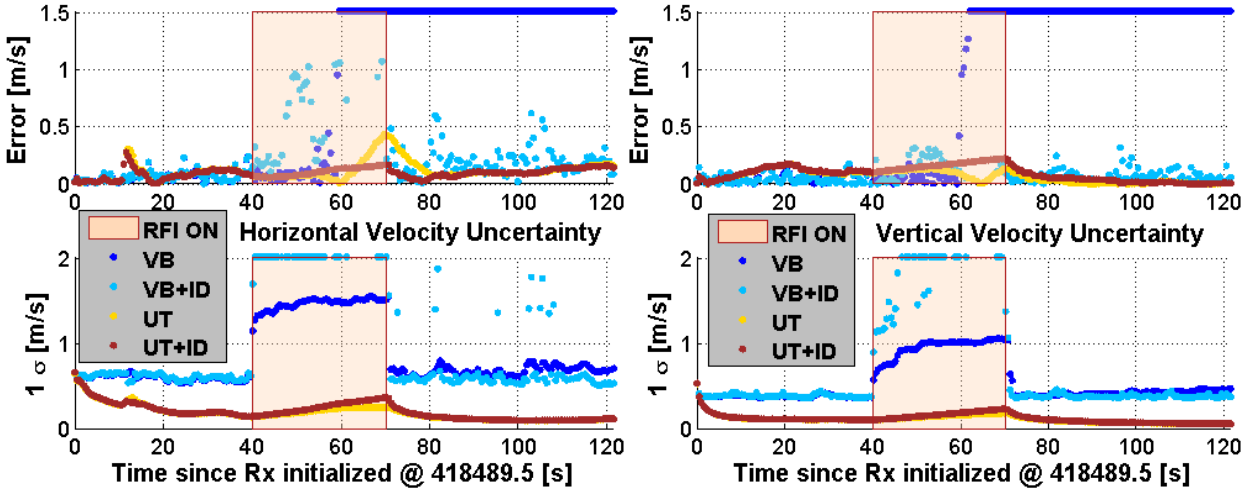

Figure 5.13: Horizontal (Left) and Absolute Vertical (Right) Velocity Errors and Corresponding Estimated Uncertainties for all Four Receivers

By looking at the estimated position and velocity uncertainties in Figure 5.12 and Figure 5.13, one can conclude that the VB receiver provides one-sigma values that are significantly smaller than the actual position and velocity errors. Hence, the navigation solution from the VB receiver cannot be fully trusted.

In contrast, both Figure 5.12 and Figure 5.13 show that, overall, the VB+ID and UT+ID receivers generated larger horizontal and vertical position (velocity) uncertainties than their counterparts. This is because the new observation weighting approach increased the variances of the Doppler and pseudorange measurements (see Equation (3.4) and Equation (3.5)). The increased uncertainty of the velocity and position estimates during interference means that the VB+ID and UT+ID solutions are more likely to be reliable compared to the solutions obtained from the VB and UT receivers, because the later receivers generated position and velocity errors which were not in agreement with their corresponding one-sigma uncertainties. For instance, the VB receiver produced

horizontal position errors greater than 20 m at $t = 60 - 70$ s, while the uncertainty was set to approximately 8 m. Conversely, during the same time period the VB+ID receiver generated horizontal position errors of approximately 6 m, while the corresponding estimated uncertainty was greater than 20 m. Similar, the VB+ID receiver produced velocity errors of about 1 m/s with the uncertainty greater than 2 m/s (i.e., errors match the uncertainty range), while the VB receiver generated velocity errors that significantly exceeded 1.5 m/s, but the uncertainty was set to approximately 1.5 m/s during $t = 60 - 70$ s.

A particularly interesting fact to mention is that the UT receiver generated velocity errors which are in agreement with their one-sigma uncertainty, while it fails to do so in terms of position estimation errors. At the same time, the UT+ID receiver managed to match the position and velocity errors with their respective estimated accuracies.

To better understand the navigation performance differences between the VB, VB+ID, UT and UT+ID receivers, Figure 5.14 summarizes the horizontal and vertical position and velocity RMSE values during CW interference. Furthermore, Figure 5.15 shows the horizontal and vertical position and velocity RMSE values after jamming was removed. When comparing all the results presented in Figure 5.14, one should bear in mind that the VB+ID receiver did not provide a navigation solution at $t = 60 - 70$ s.

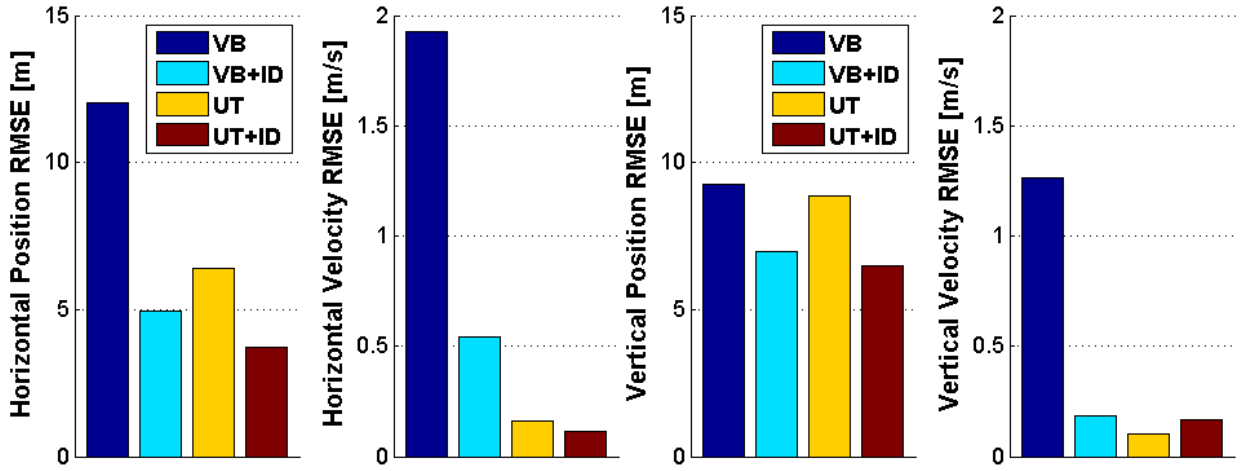

Figure 5.14: Horizontal (Left) and Vertical (Right) Position and Velocity RMS Errors in the Presence of CW

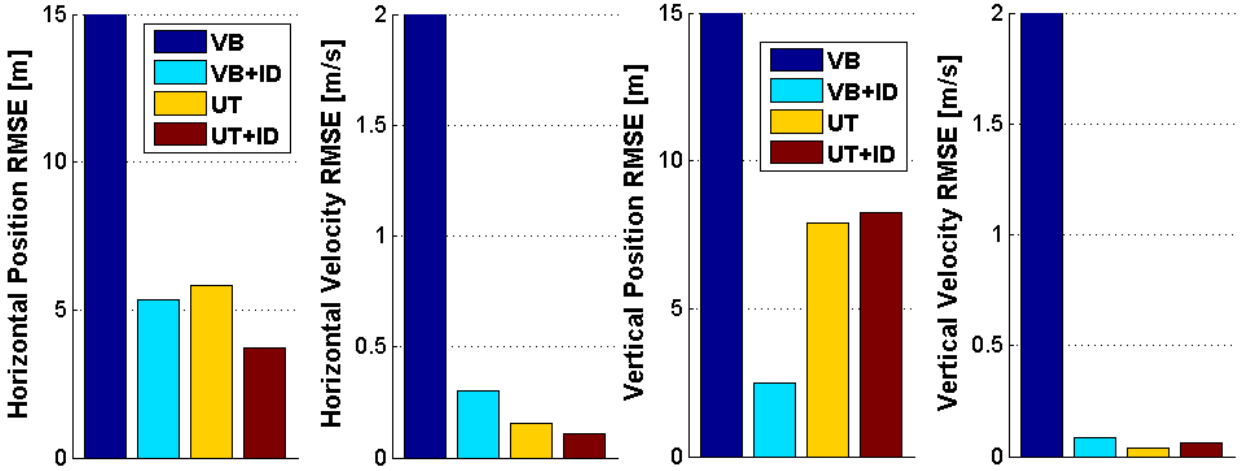

Figure 5.15: Post-Interference Horizontal (Left) and Vertical (Right) Position and Velocity RMS Errors

With regard to the statistics during the post-interference period depicted in Figure 5.15, the VB receiver showed the worst position and velocity performance compared to all other receivers (see blue bars in Figure 5.15). Interestingly, the UT and UT+ID modifications had larger vertical position RMS errors than those from the VB receiver,

while the vertical velocity RMSE was comparable for these three receivers. Note that in the case of the VB receiver in Figure 5.15, the maximum horizontal and vertical position and velocity RMSE values were constrained to 15 m and 2 m/s, respectively, and the actual errors are given in Table 5.3.

Table 5.3: Actual Position and Velocity RMS Errors Produced by the VB Receiver in Post-Interference Period

	Position RMSE, m	Velocity RMSE, m/s
Horizontal	159.5	5.5
Vertical	130.0	4.3

5.5 Summary

This chapter analyzed the tracking and navigation domain performance of the VB, VB+ID, UT and UT+ID receivers employing real data collected in an open-sky on a vehicle. The CW interference signal was injected post-mission.

A comprehensive comparison between all four tested receivers that operated in the presence of jamming was presented. Analysis of signal lock indicators as well as Doppler and pseudorange measurements allows one to conclude that CW interference affects the signals from some PRNs more than others. Therefore, in the presence of interference Doppler and pseudorange observations should be appropriately weighted or even rejected before being used by the navigation filter. Also, it was shown that all four receivers experienced loss of lock on the signal from one of the SVs when the J/N ratio varied from 20 dB to 25 dB. One of the outcomes is that the initial C/N_0 plays an

important role when interference is injected; for example, PRNs which have smaller carrier-to-noise values before jamming are likely to become more affected by the jammer than PRNs which have stronger C/N_0.

It was found that the navigation performance of the VB and UT receivers aided by the ID module and the new observation weighting technique is better than the performance of their non-aided counterparts. This was especially evident when comparing the VB versus VB+ID receivers because the former suffered from significant horizontal and vertical position and velocity biases during and after jamming. The navigation performance of the VB+ID receiver was very close to that of the UT receiver at the beginning of the interference injection (when J/N varied between 10 dB and 15 dB) and after interference; however during the period when jamming power was very strong (J/N > 20 dB) the VB+ID failed to provide a navigation solution, while the UT receiver generated a biased solution. This allows one to deduce that even IMU data aiding is not sufficient to supress the effects of CW jamming on the navigation solution if an ultra-tight receiver “blindly” uses all available Doppler and pseudorange observations rather than rejecting the most corrupted (or biased) measurements. Overall, the best position results in jamming were obtained by the UT+ID receiver.

From the results presented in this chapter, it was found that the VB+ID and UT+ID receiver modifications that utilized the novel observation weighting strategy offer more pessimistic values of the estimated position and velocity uncertainties as compared to

those of the VB and UT receivers. However, this is rather good, because the estimated position and velocity uncertainties produced by the VB+ID and UT+ID receivers were in good agreement with the actual errors. This, in turn, implies that the estimated position and velocity were reliable.

The use of real data allowed one to further test and verify the methods developed in this work. It was demonstrated that the ID and new observation weighting technique make the VB and UT receivers more tolerant to strong CW jamming.

Chapter Six: Conclusions and Recommendations

This Chapter summarizes the author's contribution and provides concluding remarks based on the results obtained herein. This is followed by suggested recommendations for future work.

6.1 Overview of Author's Contribution

This research studied the effects of aiding vector-based and ultra-tight GPS receivers with an Interference Detection module in the tracking domain. Also, an observation weighting approach that assigns appropriate weights to Doppler and pseudorange measurements in CW jamming scenarios was developed.

The methods developed were tested on simulated and real data. Specifically, medium-level vehicular dynamics was considered in this work and the data collected in an open-sky was employed for testing. Importantly, all results were obtained with poor GPS satellite availability (no more than five satellites were available) and under strong CW jamming (the J/N ratio varied between 10 dB and 25 dB in the real data test). The outcome of the conducted tests showed that even in these scenarios it is possible to obtain reasonable navigation solution accuracies using the techniques developed for interference detection and mitigation.

6.2 Conclusions

It was shown that the VB+ID and UT+ID receivers offer better overall navigation performance as compared to conventional VB and UT receivers in a CW jamming

environment. The major conclusions, which cover the objectives set in Chapter 1, are as follows:

1. The multi-correlator FFT interference detection approach is suitable for identifying strong CW signals in tracking. However, the ID initialization is challenging if no *a priori* information about interference signals is available. In some cases, this method of interference detection may substantially increase the computational load.

2. It was found that the effect of a CW signal on the effective C/N_0 may not be only destructive but constructive. Therefore, one should be extremely cautious when solely relying on the C/N_0 based interference detection technique. Rather, additional signal lock indicators should be analyzed when monitoring for CW signals.

3. Both MATLAB simulation and tracking results showed that if the linear combination of the Doppler and interference frequencies is close to an integer multiple of 1 kHz, then the signal from this particular satellite will be corrupted by interference to a large extent. It was shown that all receivers employing the KF tracking algorithm experienced either loss of lock or erroneous signal tracking when the J/N ratio exceeded 20 dB in an open-sky scenario, in which the C/N_0 values ranged between 40 dB-Hz to 50 dB-Hz (in the absence of interference). Importantly, PRNs which have smaller carrier-to-noise values before interference are likely to get more influenced by the CW interference than PRNs which have stronger C/N_0.

4. Both simulated and real data tests showed that in terms of position and velocity estimation during interference, the VB+ID and UT+ID modes outperformed the VB and UT receivers. Specifically, the VB+ID and UT+ID modifications improved horizontal position by a factor of two, while the horizontal velocity of the VB+ID receiver was improved by a factor of four compared to that of the VB receiver during interference. The VB+ID, UT, and UT+ID receivers showed comparable vertical position and velocity estimation under jamming. However, it was found that the VB receiver generated significantly biased solutions during and after CW jamming. Nevertheless, when aided by the ID module, the VB receiver showed comparable navigation performance to the UT mode. This allows one to deduce that when a vector-based receiver operates in jamming, it is rather beneficial to completely reject observations affected by interference instead of using all of them. However, if no observations are available after rejection, a vector-based receiver cannot compute the navigation solution. In case of the UT+ID receiver, a lack of observations can be compensated by IMU aiding.

5. The novel observation weighting technique, which employs not only the C/N_0 but also the FLI values, sets more appropriate observation variances in jamming than the C/N_0 weighting. Successively, this allowed one to obtain one-sigma position and velocity estimated uncertainties that matched the actual errors.

6. In the case when the VB or UT receiver does not loose lock on the signal from the satellites affected by strong interference, signal monitor should be ultimately utilized in order to avoid significant biases in the navigation solution.

7. Correct re-acquisition of the signal from satellites that were drastically affected by the interference signal is paramount. Improper re-acquisition can lead to biased Doppler and pseudorange observations, and this in turn can introduce a bias in estimated position and velocity values. Eventually, this can lead the VB (or, potentially, UT) receiver to diverge.

6.3 Recommendations

Based on the results and conclusions of this research, recommended steps for future work are as follows:

1. Test the VB+ID and UT+ID receiver performance on different types of RFI signals, such as pulsed or chirp. Specifically, it would interesting to examine the performance of the developed receivers in the presence of interference signals generated by jamming devices commercially available on the market;

2. Design an adaptive re-initialization strategy for the ID, which would be capable of choosing the appropriate settings for the ID when the operating environment of the receiver changes (for example, if the user moves from an open-sky to a dense foliage);

3. Examine the multi-correlator ID and new observation weighting scheme in combination with other RFI detection and mitigation techniques, such as notch filtering. Although the complexity of the receiver aided by the combined RFI mitigation methods will be ultimately increased, it is expected that the interference resistance capabilities of such a receiver would be enhanced;

4. Use lower-grade IMUs instead of tactical grade IMU for integration in the UT+ID receiver. This would allow to obtain an insight into how the performance of a receiver employing a low-cost IMU changes if most (or even all, in the worst case) observations are rejected by the ID due to the presence of jamming;

5. Study the re-acquisition capabilities of the VB+ID and UT+ID receivers. It was discussed that the improper re-acquisition can lead to biased Doppler and pseudorange measurements. Hence, it is crucial that the signals from SVs are properly re-acquired after the jamming source is de-activated. Moreover, attention should be paid to bit and navigation synchronization after signal re-acquisition.

References

Abdizadeh, M. (2013) *GNSS Signal Acquisition in The Presence of Narrowband Interference*. PhD Thesis, Report No. 20388, Department of Geomatics Engineering, University of Calgary.

Aminian, B. (2011) Investigations of GPS Observations for Indoor GPS/INS Integration, MSc Thesis, Report No. 20339, Department of Geomatics Engineering, The University of Calgary, Canada.

Aumayer, B.M., M.G. Petovello and G. Lachapelle (2014) “Development of a Tightly Coupled Vision/GNSS System”, Proceedings of ION GNSS+2014 (Tampa, FL, 08-12 Sep), The Institute of Navigation, 10 pages.

Balaei, A. T. & D. M. Akos (2012) "Cross Correlation Impacts and Observations in GNSS Receivers", NAVIGATION, Journal of The Institute of Navigation, Vol. 58, No. 4, Winter 2011-2012, pp. 323-333.

Balaei, A. T., A.G. Dempster and J. Barnes (2006) “A Novel Approach in Detection and Characterization of CW Interference of GPS Signal Using Receiver Estimation of C/No”, IEEE/ION PLANS 2006, pp. 1120-1126.

Bastide, F., E. Chatre, and C. Macabiau (2001) "GPS Interference Detection and Identification Using Multicorrelator Receivers," Proceedings of the 14th International

Technical Meeting of the Satellite Division of The Institute of Navigation (ION GPS 2001), Salt Lake City, UT, September 2001, pp. 872–881.

Bastide, F., E., Stna, D. Akos, C. Macabiau and B. Roturier (2003) “Automatic Gain Control (AGC) as an Interference Assessment Tool,” Proceedings of the 16th International Technical Meeting of the Satellite Division of The Institute of Navigation (ION GPS/GNSS 2003), September 9-12, Oregon Convention Center, Portland, OR, pp. 2042-2053.

Betz, J.W. (2001) "Effect of partial-band interference on receiver estimation of C/N0: Theory", Proceedings of ION 2001, Institute of Navigation, pp.872-881.

Bhaskar, S. (2014) “Exploiting quasi-periodicity in receiver dynamics to enhance GNSS carrier phase tracking”, Proceedings of ION GNSS+2014 (Tampa, FL, 08-12 Sep), The Institute of Navigation, 15 pages.

Borio, D. (2008) *A Statistical Theory for GNSS Signal Acquisition*, Doctoral Thesis, Dipartimento di Elettronica, Politecnico di Torino, Italy.

Borio, D., L. Camoriano, S. Savasta, and L. Lo Presti (2008) Time-Frequency Excision for GNSS Applications, IEEE Systems Journal, Volume 2, Issue 1, March 2008, pp. 27-37.

Broumandan, A. (2013) *GNSS Receiver Design*, ENGO 638 Course Notes, Department of Geomatics Engineering, University of Calgary, Canada.

Brown, A. (2000) “Multipath Rejection Through Spatial Processing,” in Proceedings of ION GPS 2000, 19-22 September, Salt Lake City, UT, pp. 2330 – 2337.

Cavaleri, A., B. Motella, M. Pini and M. Fantino (2010), “Detection of Spoofed GPS Signals at Code and Carrier Tracking Level,” in Satellite Navigation Technologies and European Workshop on GNSS Signals and Signal Processing (NAVITEC), pp. 1-6, December 8 - 10.

Craven, P., R. Wong, N. Fedora, and P. Crampton (2012) “Studying the Effects of Interference on GNSS Signals”, In International Technical Meeting (ITM) of The Institute of Navigation San Diego, CA, January 28-30, 2013. pp. 893–900.

Chan, B. (2013) *DGPS and UWB Aided Vector-Based GNSS Receivers for Weak Signal Environments*. MSc Thesis, Report No. 20371, Department of Geomatics Engineering, The University of Calgary.

Chang, P. C., H. M. Peng and S. Y. Lin (2004) “Allan Variance Estimated by Phase Noise Measurements”, 36th Annual Precise Time and Time Interval (PTTI) Meeting, pp. 165 – 172.

Chronos Technology (2014) *SENTINEL Project – GNSS Vulnerabilities*, Chronos Technology, Project Report 001, 04 April 2014, 59 pages.

Chiou, T., S. Alban, S. Atwater, J. Gautier, S. Pullen, P. Enge, D. Akos, D. Gebre-Egziabher, B. Pervan (2002) "Performance Analysis and Experimental Validation of a

Doppler-Aided GPS/INS Receiver for JPALS Applications" , ION GNSS 17th International Technical Meeting of the Satellite Division, 21-24 Sept. 2004, Long Beach, CA, pp.1609–1618.

Curran, J. (2010) *Weak Signal Digital GNSS Tracking Algorithms*. PhD Thesis, Department of Electrical and Electronic Engineering, National University of Ireland, Cork, October 2010.

Curran, J.T., D. Borio and C.C. Murhpy (2009) “Front-End Filtering and Quantization Effects on GNSS Signal Processing”, IEEE Wireless VITAE, Aalborg, Denmark, 17-20 May 2009.

Curran, J.T., M. Petovello and G. Lachapelle (2013) “Design Paradigms for Multi-Constellation Multi-Frequency Software GNSS Receivers”, Proceedings of China Satellite Navigation Conference, Springer, 13 pages.

Daneshmand, S. (2013) *GNSS Interference Mitigation Using Antenna Array Processing*. PhD Thesis, Report No. 20376, Department of Geomatics Engineering, University of Calgary.

Daneshmand, S., A. Jafarnia-Jahromi, A. Broumandan and G. Lachapelle (2012) A Low-Complexity GPS Anti-Spoofing Method Using a Multi-Antenna Array. Proceedings of GNSS12 (Nashville, TN, 18-21 Sep), The Institute of Navigation, 11 pages.

Dhital, A., J.B. Bancroft and G. Lachapelle (2012) “Reliability of an Adaptive Integrated System through Consistency Comparisons of Accelerometers and GNSS Measurements,” Proceedings of GNSS12 (Nashville, TN, 18-21 Sep), The Institute of Navigation, 9 pages.

Dovis, F. (2011) “Recent trends in Interference Mitigation and Spoofing Detection”, Conference presentation, ICL-GNSS 2011, Tampere, June 30, 2011.

Gelb, A. (1974) Applied Optimal Estimation. The M.I.T. Press.

Gibbons, G. (2013) “FCC Fines Operator of GPS Jammer That Affected Newark Airport GBAS”, http://www.insidegnss.com/node/3676, last accessed November 05, 2014.

Giordanengo, G. (2009) *Impact of Notch Filtering on Tracking Loops for GNSS Applications*, Master Thesis, Facoltà di Ingegneria dell'infromazione, Politecnico di Torino.

Grewal, M. S., L. R. Weill and A. P. Andrews (2009) *Global Positioning Systems, Inertial Navigation, and Integration*, Wiley-Interscience, 2nd Edition, 552 p.

Grooves, P. (2005) GPS Signal To Noise Measurement In Weak Signal And High Interference Environments. NAVIGATION, Journal of The Institute of Navigation, Vol. 52, Issue 2, pp. 83-92.

Gustafson, D. and J. Dowdle (2003) "Deeply Integrated Code Tracking: Comparative Performance Analysis," ION GPS/GNSS 2003, 9-12 September 2003, Portland, OR, pp. 9-12.

Haung, Lili (2010) *LIDAR, Camera and Inertial Sensors Based Navigation Techniques for Advanced Intelligent Transportation System Applications.* PhD Thesis, University of California, Riverside.

Jafarnia-Jahromi, A., T. Lin, A. Broumandan, J. Nielsen and G. Lachapelle (2012) Detection and Mitigation of Spoofing Attacks on a Vector Based Tracking GPS Receiver. International Technical Meeting, Institute of Navigation, 30 Jan – 1 Feb, Newport Beach, CA, 11 pages.

Jafarnia-Jahromi, A. (2013) *GNSS Signal Authenticity Verification in the Presence of Structural Interference*. PhD Thesis, Report No. 20385, Department of Geomatics Engineering, University of Calgary.

Kamel, A.M., V. Renaudin, J. Nielsen and G. Lachapelle (2013) "INS Assisted Fuzzy Tracking Loop for GPS-Guided Missiles and Vehicular Applications," International Journal of Navigation and Observation, 2013, pp.1-17, http://www.hindawi.com/journals/ijno/2013/750385/, last accessed November 08, 2014.

Kim, J.W., Dong-Hwan Hwang and S.J. Lee (2007) "Performance Evaluation of INS Velocity-Aided Tracking Loop and Deeply Coupled GPS/INS Integration System in Jamming Environment," ION 63rd Annual Meeting, April 23-25, 2007, Cambridge, Massachusetts pp.742–748.

Kumar, R. and M.G. Petovello (2014) “A Novel GNSS Positioning Technique for Improved Accuracy in Urban Canyon Scenarios using 3D City Model”, Proceedings of ION GNSS+2014 (Tampa, FL, 08-12 Sep), The Institute of Navigation, 10 pages.

Landry, R. Jr. & A. Renard (2014) “Analysis of Potential Interference Sources and Assessment of Present Solutions for GPS/GNSS Receivers”, http://lassena.etsmtl.ca/IMG/pdf/doc_25.pdf, last accessed on September 18, 2014.

Lashley, M. (2009) *Modeling and Performance Analysis of GPS Vector Tracking Algorithms*. PhD Thesis, Auburn University, USA, 391 pages.

Lin, Tao, M. Abdizadeh, A. Broumandan, D. Wang, K. O'Keefe, and G. Lachapelle (2011) Interference Suppression for High Precision Navigation Using Vector-Based GNSS software Receivers. Proceedings of GNSS11 (Portland, OR, 20-23 Sep), The Institute of Navigation, 12 pages.

Li Tan, Jean Jiang and Liangmo Wang (2011) Adaptive Harmonic IIR Notch Filters for Frequency Estimation and Tracking, Adaptive Filtering, Dr Lino Garcia (Ed.), ISBN: 978-953-307-158-9, InTech, Available from:

http://www.intechopen.com/books/adaptive-filtering/adaptive-harmonic-iir-notch-filters-for-frequency-estimation-and-tracking, last accessed November 08, 2014.

Li, T., M. Petovello, G. Lachapelle and C. Basnayake (2010) Ultra-tightly Coupled GPS/Vehicle Sensor Integration for Land Vehicle Navigation, NAVIGATION, Journal of The Institute of Navigation, Vol. 57, No. 4, 263-274.

Liu, S., M. M. Atia, T. B. Karamat and A. Noureldin (2014) A LiDAR-Aided Indoor Navigation System for UGVs, Journal of Navigation, The Royal Institute of Navigation, 21 page.

Macabiau, C., O. Julien and E. Chatre (2001) "Use of Multicorrelator Techniques for Interference Detection," ION NTM 2001, 22-24 January 2001, Long Beach, CA, pp. 353-363.

Misra, P. and P. Enge (2011) *Global Positioning System: Signals, Measurements, and Performance*, Revised 2nd ed. Ganga-Jamuna Press, 2011, 561 pages.

Moelker, D.J. (1998) *Interference in satellite navigation and mobile communication,* Dissertation, TU Delft, http://repository.tudelft.nl/view/ir/uuid%3A93c5f66e-71c8-4dc1-841c-9ab5426fbb8d/, last accessed November 07, 2014.

Mongrédien, M., G. Lachapelle and M.E. Cannon (2006) “Testing GPS L5 Acquisition and Tracking Algorithms Using a Hardware Simulator”, Proceedings of GNSS06 (Forth Worth, 26-29 Sep, Session C6), The Institute of Navigation, 13 pages.

Mongrédien, C., G. Lachapelle and M.E. Cannon (2008) “Testing GPS L5 Tracking Algorithms And Their Impact on Positioning Accuracy”, Proceedings of European Navigation Conference (Toulouse, 23-25 April), 10 pages.

Montloin, L. (2010) *Impact of Interference Mitigation Techniques on a GNSS Receiver*. Memoire de fin d'Etudes, Ecole Nationale de l'Aviation Civile, Toulouse.

Muthuraman, K., and D. Borio (2010) C/N0 Estimation for Modernized GNSS Signals: Theoretical Bounds and a Novel Iterative Estimator. NAVIGATION, Journal of The Institute of Navigation, Vol. 57, No. 4, Winter 2010, 309-323.

Navipedia (2014) *Front End*, European Space Agency, http://www.navipedia.net/index.php/Front_End, last accessed November 4, 2014.

Navstar (2013) *Interface Specification IS-GPS*-200, http://www.gps.gov/technical/icwg/IS-GPS-200H.pdf, last accessed on December 15, 2014.

Ndili, A. and P. Enge (1998) “GPS Receiver Autonomous Interference Detection,” in IEEE Position, Location and Navigation Symposium - PLANS’98, April, Palm Springs, California, pp. 123-130.

Nielsen, J., A. Broumandan and G. Lachapelle (2011) GNSS Spoofing Detection for Single Antenna Handheld Receivers. NAVIGATION, Journal of The Institute of Navigation, Vol. 58, No. 4, 335-344.

NovAtel (2010) OEMV Family of Receivers - Firmware Reference Manual, Rev 8, OM-20000094, http://www.novatel.com/assets/Documents/Manuals/om-20000094.pdf, last accessed December 01, 2010.

Noureldin, A., T.B. Karamat and J. Georgy (2013) *Fundamentals of Inertial Navigation, Satellite-based Positioning and their Integration*, Springer, 313 pages.

O'Driscoll, C., M. Petovello and G. Lachapelle (2011) Choosing the Coherent Integration Time for Kalman Filter Based Carrier Phase Tracking of GNSS Signals. GPS Solutions, 5(4), 345-356.

Ohlmeyer, E.J. (2006) "Analysis of an Ultra-Tightly Coupled GPS/INS System in Jamming," Position, Location, And Navigation Symposium, 2006 IEEE/ION, April 25-27, pp. 44–53.

Ouzeau, C., C. Macabiau, B. Roturier and M. Mabilleau (2008) "Performance of Multicorrelators GNSS Interference Detection Algorithms for Civil Aviation," ION NTM 2008, 28-30 January 2008, San Diego, CA, pp. 28–30.

Pany, T. (2010) *Navigation Signal Processing for GNSS Software Receivers,* Artech House, Chapter 6, 352 p.

Pany, T., J. Winkel, B. Riedl, M. Restle, T. Worz, R. Schweikert, H. Niedermeier, G. Ameres, B. Eissfeller, S. Lagrasta and G. Lopez-Risueno (2009) "Performance of a Partially Coherent Ultra-Tightly Coupled GNSS / INS Pedestrian Navigation System

Enabling Coherent Integration Times of Several Seconds to Track GNSS Signals Down to 1.5 dBHz", 22nd International Meeting of the Satellite Division of The Institute of Navigation, Savannah, GA, pp.919-934.

Petovello, M. (2003) *Real-time Integration of a Tactical-Grade IMU and GPS for High-Accuracy Positioning and Navigation*, PhD Thesis, published as UCGE Report No. 20173, Department of Geomatics Engineering, University of Calgary, Canada.

Petovello, M., and G. Lachapelle (2006) "Comparison of Vector-Based Software Receiver Implementations with Application to Ultra-Tight GPS/INS Integration," ION GNSS 2006, Fort Worth TX, 26-29 September 2006 pp. 26–29.

Petovello, M.G., C. O'Driscoll and G. Lachapelle (2008a) “Weak Signal Carrier Tracking Using Extended Coherent Integration with an Ultra-Tight GNSS/IMU Receiver”, Proceedings of European Navigation Conference (Toulouse, 23-25 April), 11 pages.

Petovello, M.G., C. O'Driscoll and G. Lachapelle (2008b) “Carrier Phase Tracking of Weak Signals Using Different Receiver Architectures”, Proceedings of ION NTM08 (San Diego, 28-30 Jan, Session A4). The Institute of Navigation, 11 pages.

Petovello, M.G., C. O'Driscoll, G. Lachapelle, D. Borio, H. Murtaza (2008c) “Architecture and Benefits of an Advanced GNSS Software Receiver”, International Symposium on GPS/GNSS 2008, November 11-14, Tokyo, Japan, 11 pages.

Petovello, M. (2012) *Estimation for Navigation*, ENGO 620 Lecture Notes, Department of Geomatics Engineering, University of Calgary, Canada.

Psiaki, M.L. (2001) “Smoother-Based GPS Signal Tracking in a Software Receiver”, Proceedings of ION GPS 2001, pp. 2900-2913.

Ren, T. (2014) *A Standalone Approach for High-Sensitivity GNSS Receivers*. PhD Thesis, Report No. 20412, Department of Geomatics Engineering, University of Calgary.

Rugamer, A., I. Lukcin, G. Rohmer, and J. Thielecke (2013) "GNSS Interference Detection Using a Compressed Sensing Analog to Information Converter Approach", Proceedings of the 2013 International Technical Meeting of The Institute of Navigation, San Diego, California, January 2013, pp. 843-855.

Sheridan, K., Y. Ying and T. Whitworth (2010) "Pre- and Post-Correlation GNSS Interference Detection within Software Defined Radio," 25th International Technical Meeting of the Satellite Division of the ION, Nashville, TN, September 17 - 21, pp. 3542-3548.

Soloviev, A., D. Bates and F. van Graas (2007) Tight Coupling of Laser Scanner and Inertial Measurements for a Fully Autonomous Relative Navigation Solution. NAVIGATION, Journal of The Institute of Navigation, Vol. 54, No. 3, pp. 189-205.

Teunissen, P. J. G. and M. A. Salzmann (1989) *A recursive slippage test for use in state-space filtering*, Manuscripta Geodaetica, 14, pp. 383–390.

Thompson, R. J. R., Jinghui Wu, A. Tabatabaei Balaei, and Andrew G. Dempster (2010) "Detection of RF interference to GPS using day-to-day C/No differences", 2010 International Symposium on GPS/GNSS, Taipei, Taiwan, October 26-28, 2010, 7 pages, http://www.gmat.unsw.edu.au/snap/publications/thompson_etal2010a.pdf, last accessed November 08, 2014.

Therrien, C.W. and C.H. Velasco (1993) "An Iterative Prony Method for ARMA Signal Modelling", IEEE Transactions on Signal Processing, Vol. 43, Issue 1, Jan 1995, pp. 358-361.

Tsui, J. (2005) *Fundamentals of Global Positioning System Receivers: A Software Approach*, 2nd edition, Wiley-Interscience, 352 pages.

Van Dierendonck, A. J. (1996) *GPS Receivers. B. Parkinson and J. J. Spilker, Jr., eds., Global Positioning System: Theory and Applications*, volume I, chapter 8. American Institute of Aeronautics and Astronautics, Inc., Washington D.C., USA.

Van Veen, B. and K. M. Buckley (1988) "Beamforming: A versatile approach to spatial filtering", IEEE ASSP Magazine 5 (2), pp. 4-24.

Ward, P. W. (1994) GPS Receiver RF Interference Monitoring, Mitigation, and Analysis Techniques, NAVIGATION, Journal of The Institute of Navigation, Vol. 41, No. 4, Winter 1994–1995, pp. 367–391.

Ward, P.W., J.W. Betz and C.J. Hegarty (2006) Understanding GPS: Principles and Applications, K. D. Kaplan and C. J. Hegarty, ed., Understanding GPS Principles and Applications, Chapter 6, Artech House.

Wang, L., P. Grooves and M. Ziebart (2012) Multi-Constellation GNSS Performance Evaluation for Urban Canyons Using Large Virtual Reality City Models, Journal of Navigation, The Royal Institute of Navigation, Vol., 65, Issue 03, July 2012, pp. 459-476.

Wildemeersch, M. and J. Fortuny-Guasch (2010) *Radio Frequency Interference Impact Assessment on Global Navigation Satellite Systems*, EUR 24242 EN - January 2010, European Commission, JRC, http://publications.jrc.ec.europa.eu/repository/bitstream/111111111/13508/1/reqno_jrc55767_radio_frequency_interference_impact_assessment_on_global_navigation_satellite_systems%5B1%5D.pdf), last accessed November 05, 2014.

Xie, Peng (2013) *Improving High Sensitivity GNSS Receiver Performance in Multipath Environments for Vehicular Applications*. PhD Thesis, Report No 20389, Department of Geomatics Engineering, University of Calgary.

Ziedan, N.I. and J.L. Garrison (2004) “Extended Kalman Filter-Based Tracking of Weak GPS Signals under High Dynamic Conditions”, Proceedings of ION GNSS 2004, pp. 20-31.

Appendix A: Tracking and Navigation Performance of the UT and UT+ID Receivers Using Simulated Data

A.1. Tracking Level

Figure A.1 and Figure A.2 show the effective C/N_0 estimates, FLI and PLI metrics for the UT and UT+ID receivers, respectively. As it was discussed in Chapter 4, these values do not significantly differ from those obtained from the VB and VB+ID receivers.

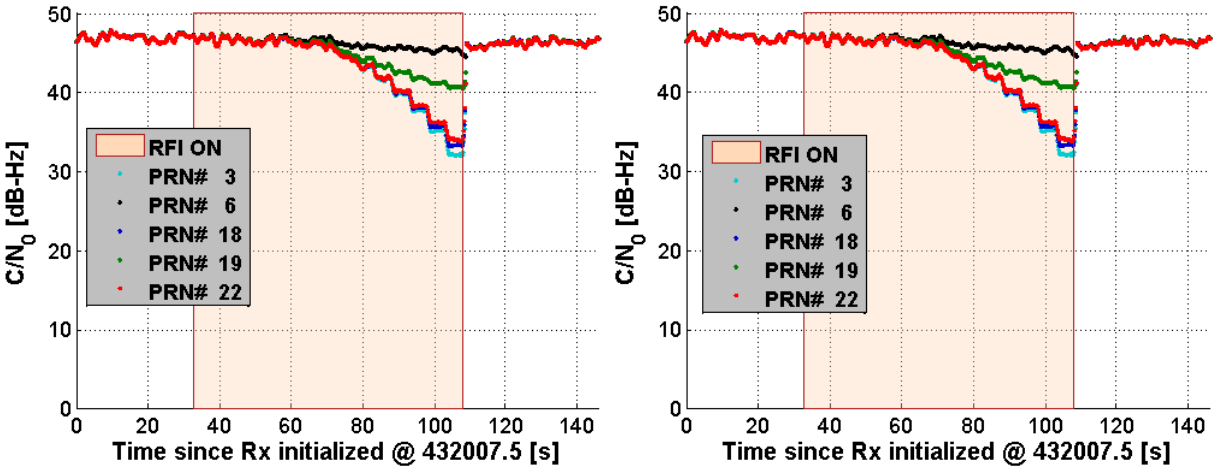

Figure A.1: Estimated C/N_0 of all PRNs (left: UT Rx, right: UT+ID Rx)

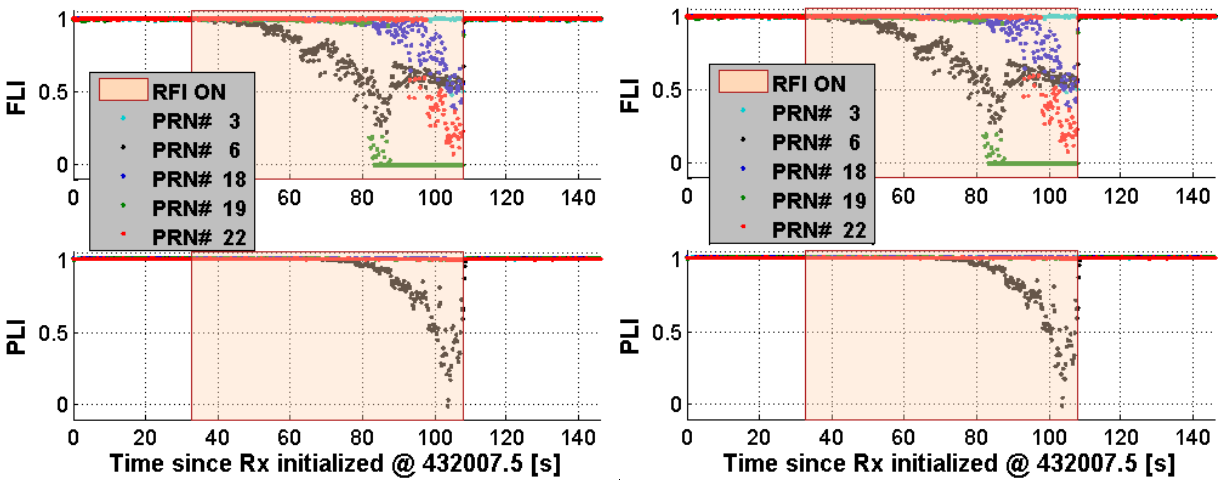

Figure A.2: Estimated FLI and PLI of all PRNs (left: UT Rx, right: UT+ID Rx)

A.2. Navigation Level

Figure A.3 shows the observation status obtained in the UT and UT+ID receivers. Once again, the UT receiver aided by the ID unit, was able to reject multiple corrupted measurements during CW interference, while the UT receiver used almost all observations to compute the navigation solution.

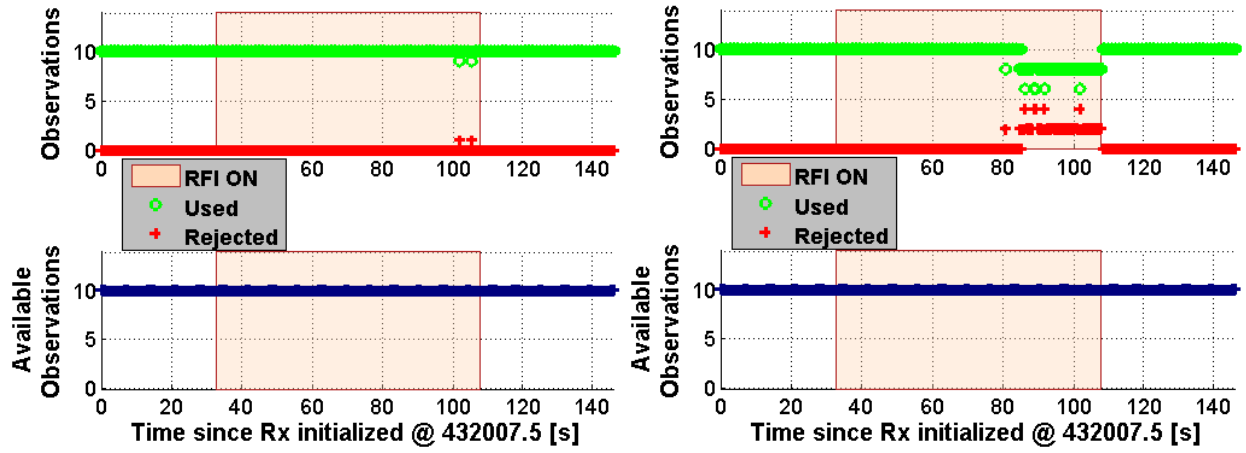

Figure A.3: Observation Status for all 5 PRNs (left: UT Rx, right: UT+ID Rx)

To demonstrate vertical navigation performance, Figure A.4 and Figure A.5 present the vertical position and velocity errors generated by all four receivers considered in this work. Analyzing Figure A.4, one sees that the VB receiver suffered from a bias after interference was removed. However, in the presence of CW interference, all four receivers demonstrated comparable performance of height estimation. Interestingly, as Figure A.5 shows, the VB receiver experienced apparent vertical velocity errors close to the end of the interference injection period and, at the same time, the estimated one-sigma uncertainty of the VB modification did not match the velocity errors. In the case of the other three receivers, the estimated velocity and position accuracies were in better agreement with actual errors.

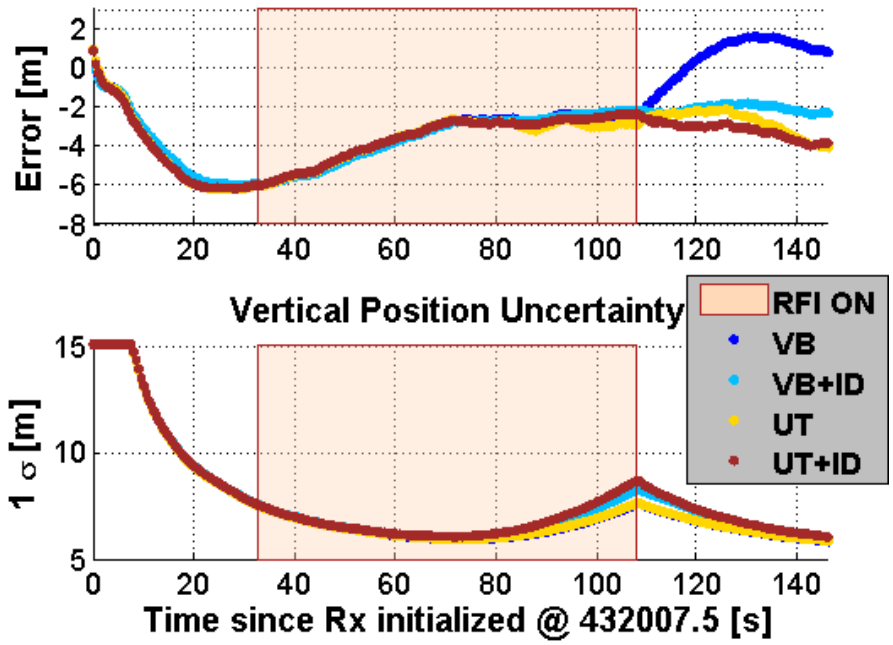

Figure A.4: Vertical Position Errors and Vertical Position Uncertainties of all Four Receivers vs. Time

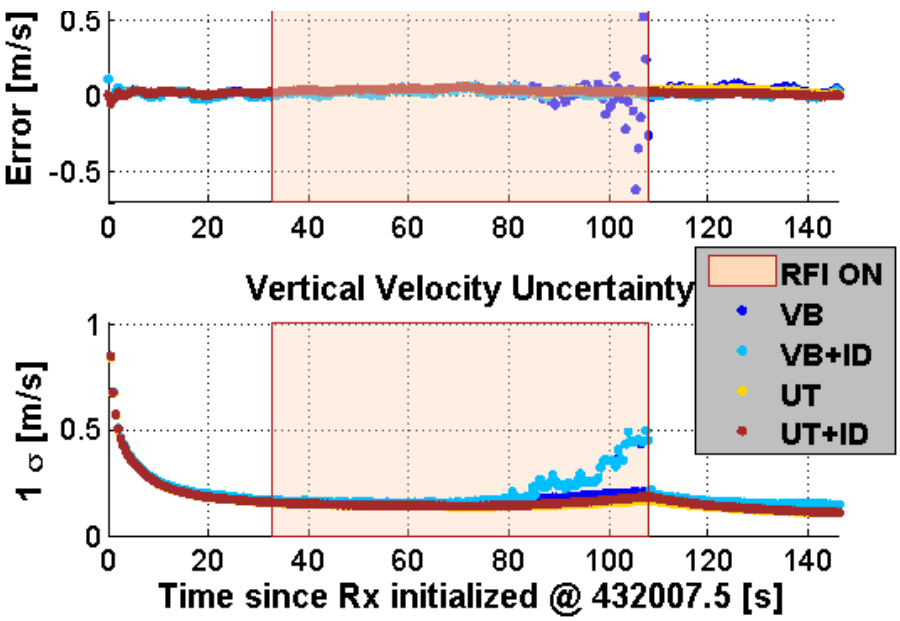

Figure A.5: Vertical Velocity Errors and Vertical Velocity Uncertainties of all Four Receivers vs. Time

Figure A.6 and Figure A.7 summarize the vertical position and velocity estimation performance of the VB, VB+ID, UT and UT+ID receivers. Once again, while the height estimation of all receivers in the presence of CW signal was comparable, the VB receiver suffered more from velocity errors. Figure A.7 shows that the height errors generated by the VB receiver were smaller than those of other receiver modifications; however, Figure A.4 shows that these smaller errors should be interpreted with caution because the VB receiver provided biased height estimation in contrast to other receivers (i.e., in the VB receiver this bias was closer to zero, thus, the error is smaller). Figure A.7 also shows that the VB+ID and UT+ID receiver outperformed their respective counterparts after the CW source was de-activated in terms of vertical velocity

estimation. Moreover, the VB+ID receiver established smaller errors than the UT receiver.

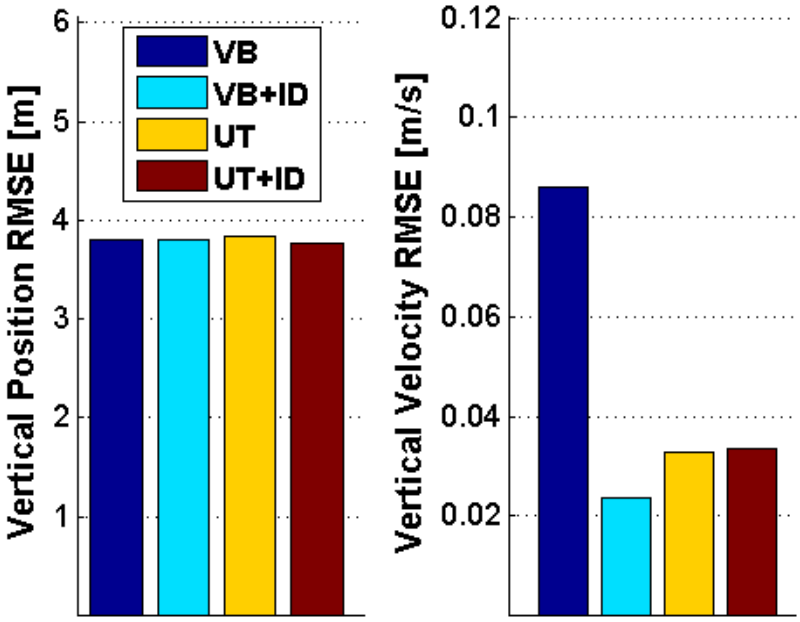

Figure A.6: Vertical Position and Velocity RMS Errors in the presence of CW

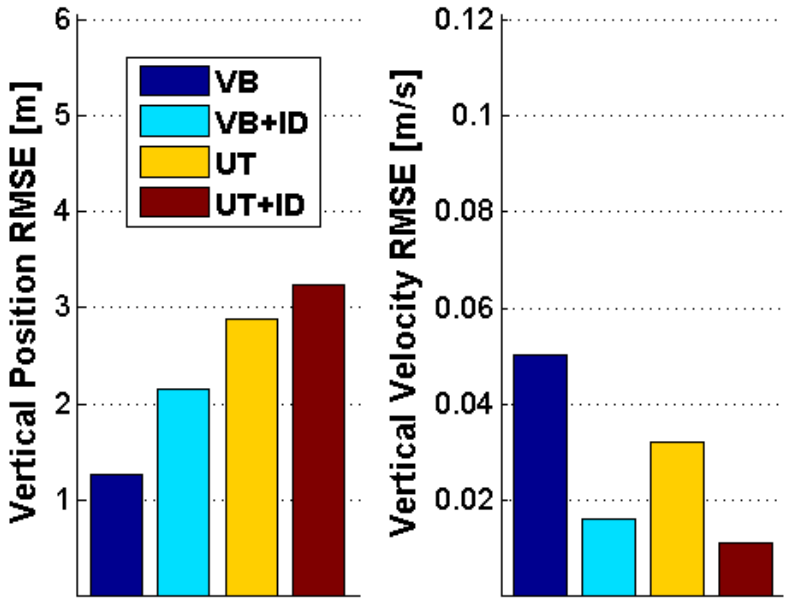

Figure A.7: Post-Interference Horizontal Position and Velocity RMS Errors

Appendix B: Tracking and Navigation Performance of the UT and UT+ID Receivers Using Real Data

B.1. Tracking Level

Figure B.8 and Figure B.9 show the effective C/N_0 estimates, FLI and PLI metrics for the UT and UT+ID receivers, respectively. As it was discussed in Chapter 5, the carrier-to-noise values as well as the FLI and PLI values do not significantly differ from those obtained from the VB and VB+ID receivers. This can be explained by the fact that all four tested receivers utilized the same signal tracking algorithm.

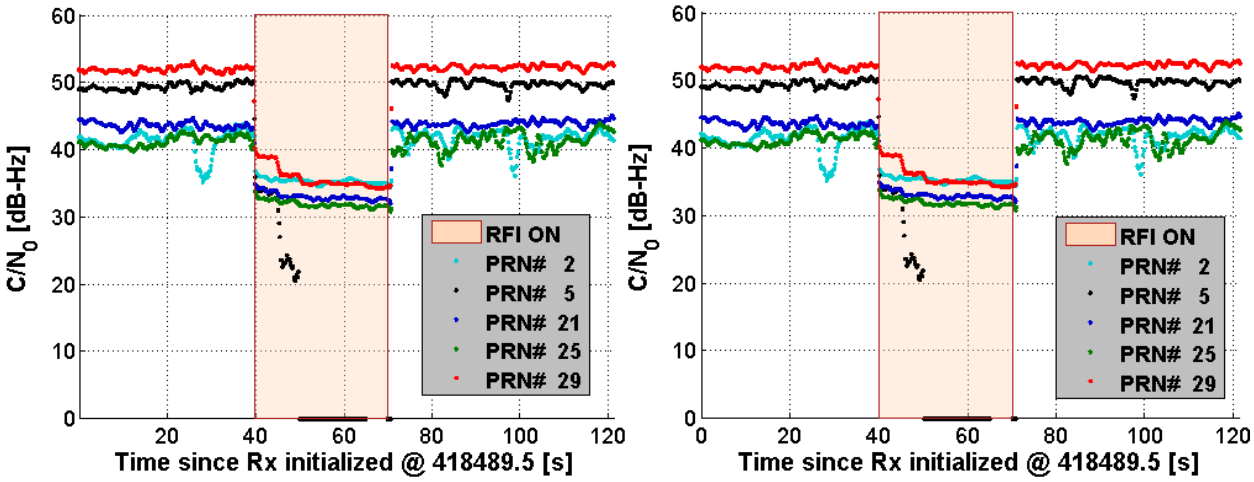

Figure B.8: Estimated C/N_0 of all PRNs (left: UT Rx, right: UT+ID Rx)

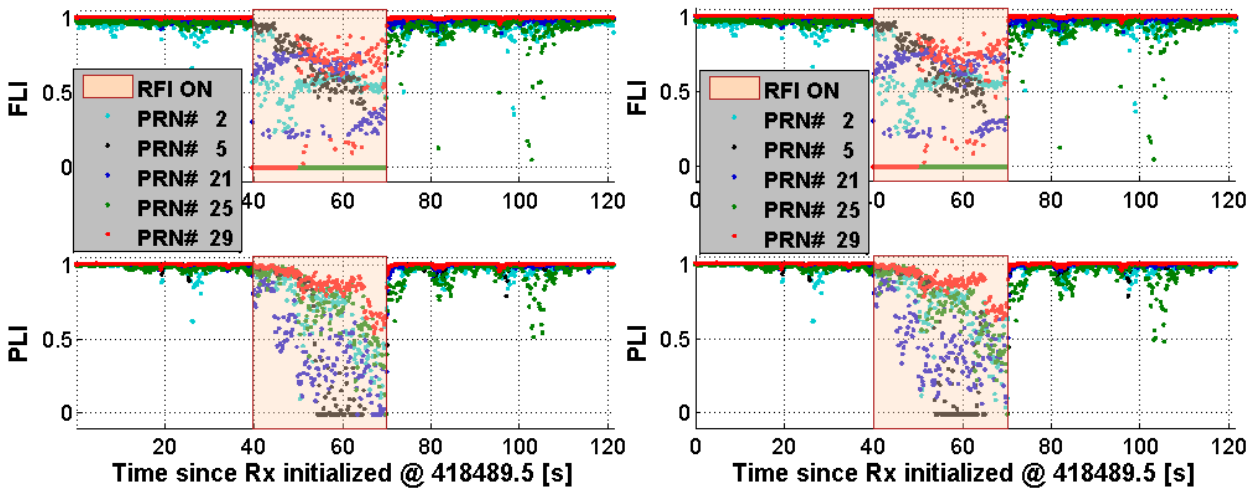

Figure B.9: Estimated FLI and PLI of all PRNs (left: UT Rx, right: UT+ID Rx)

B.2. Navigation Level

Figure B.10 shows that in case of the UT+ID receiver, multiple observations were rejected during $t = 40 - 70$ s. Note that the UT receiver rejected only two measurements during the same time period.

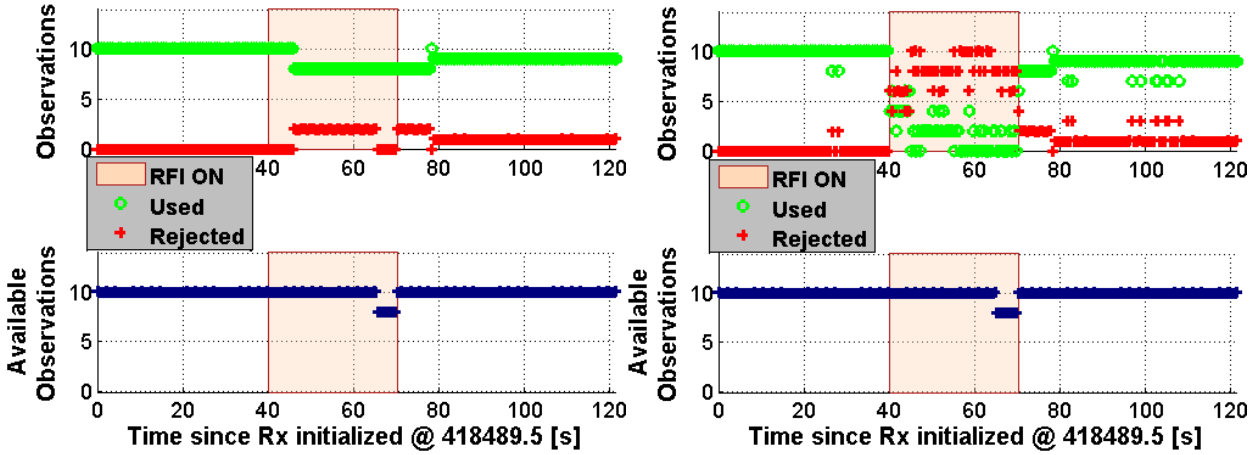

Figure B.10: Observation Status for all 5 PRNs (left: UT Rx, right: UT+ID Rx)

Figure B.11 shows the detailed interpretation of rejected observations presented earlier in Figure B.10. Also, Figure B.11 shows that one pseudorange was rejected starting from $t \approx 78$ s. This is the pseudorange obtained from the re-acquired PRN 5, for which both UT and UT+ID receivers failed to establish correct bit and navigation synchronization.

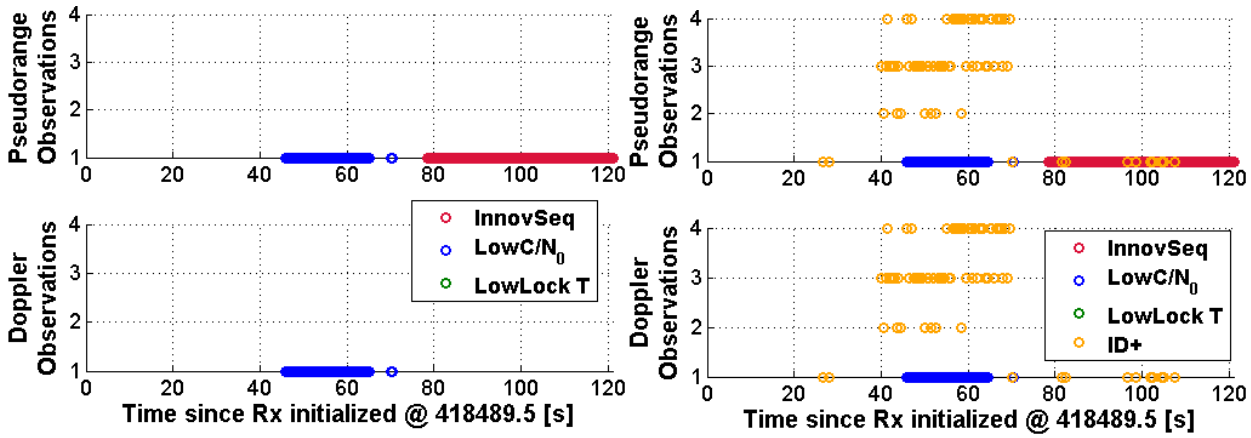

Figure B.11: Status of Rejected Observations (left: UT Rx, right: UT+ID Rx)

Figure B.12 shows the phase noise measurements of the TCXO oscillator employed in the GTEC RFFE Fraunhofer IIS Flexiband RF front-end. Phase noise values at frequency 1 Hz, 10 Hz and 100 Hz were taken to compute the h_{-2}, h_{-1} and h_0 parameters, respectively. Note that phase noise taken at 1 Hz, 10 Hz and 100 Hz correspond to Random Walk FM, Flicker FM and White FM noise processes (Chang et al 2004).

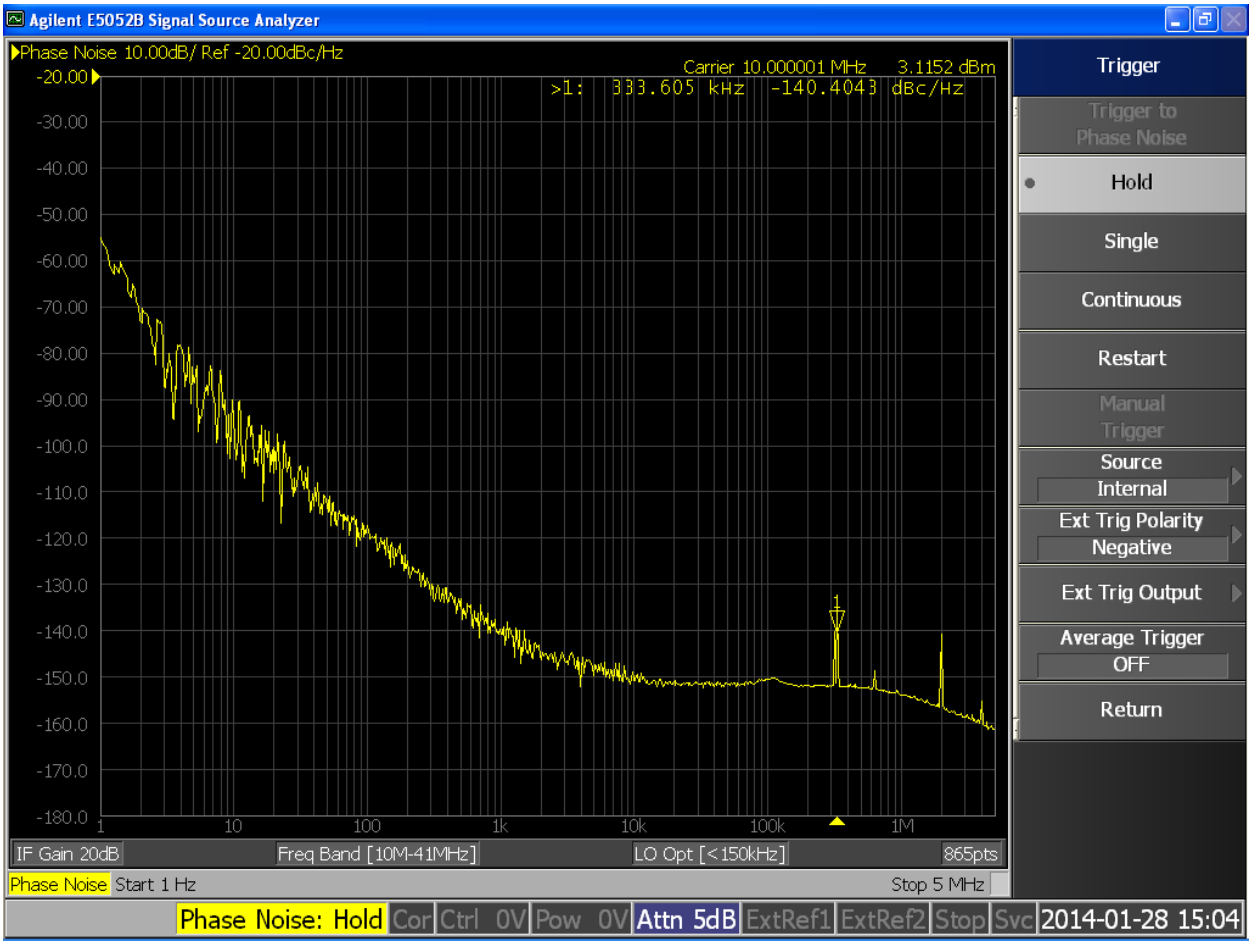

Figure B.12: GTEC RFFE Fraunhofer IIS TCXO Oscillator Phase Noise Measurements (courtesy of Fraunhofer IIS)